

Orbital dynamics in excited neon collisions

Citation for published version (APA):

Op De Beek, S. S. (1996). *Orbital dynamics in excited neon collisions*. [Phd Thesis 1 (Research TU/e / Graduation TU/e), Applied Physics and Science Education]. Technische Universiteit Eindhoven.
<https://doi.org/10.6100/IR468942>

DOI:

[10.6100/IR468942](https://doi.org/10.6100/IR468942)

Document status and date:

Published: 01/01/1996

Document Version:

Publisher's PDF, also known as Version of Record (includes final page, issue and volume numbers)

Please check the document version of this publication:

- A submitted manuscript is the version of the article upon submission and before peer-review. There can be important differences between the submitted version and the official published version of record. People interested in the research are advised to contact the author for the final version of the publication, or visit the DOI to the publisher's website.
- The final author version and the galley proof are versions of the publication after peer review.
- The final published version features the final layout of the paper including the volume, issue and page numbers.

[Link to publication](#)

General rights

Copyright and moral rights for the publications made accessible in the public portal are retained by the authors and/or other copyright owners and it is a condition of accessing publications that users recognise and abide by the legal requirements associated with these rights.

- Users may download and print one copy of any publication from the public portal for the purpose of private study or research.
- You may not further distribute the material or use it for any profit-making activity or commercial gain
- You may freely distribute the URL identifying the publication in the public portal.

If the publication is distributed under the terms of Article 25fa of the Dutch Copyright Act, indicated by the "Taverne" license above, please follow below link for the End User Agreement:

www.tue.nl/taverne

Take down policy

If you believe that this document breaches copyright please contact us at:

openaccess@tue.nl

providing details and we will investigate your claim.

Orbital Dynamics in Excited Neon Collisions



S.S. Op de Beek

Orbital Dynamics in Excited Neon Collisions

PROEFSCHRIFT

TER VERKRIJGING VAN DE GRAAD VAN DOCTOR AAN
DE TECHNISCHE UNIVERSITEIT EINDHOVEN, OP GEZAG
VAN DE RECTOR MAGNIFICUS, PROF. DR. M. REM, VOOR
EEN COMMISSIE AANGEWEEZEN DOOR HET COLLEGE VAN
DEKANEN IN HET OPENBAAR TE VERDEDIGEN OP VRIJDAG
1 NOVEMBER 1996 OM 16.00 UUR

DOOR

STEFAN SERVAS OP DE BEEK

GEBOREN TE ROERMOND

DIT PROEFSCHRIFT IS GOEDGEKEURD
DOOR DE PROMOTOREN:
PROF.DR. H.C.W. BELJERINCK
EN
PROF.DR. B.J. VERHAAR

COPROMOTOR:
DR.IR. J.P.J. DRIESSEN

CIP-GEGEVENS KONINKLIJKE BIBLIOTHEEK, DEN HAAG

Beek, Op de, Stefan Servas

Orbital dynamics in excited neon collisions /
Stefan Servas Op de Beek. - Eindhoven :
Eindhoven University of Technology
Thesis Technische Universiteit Eindhoven. - With ref. -
With summary in Dutch.
ISBN 90-386-0009-7

*aan Renske
en onze moeders*

Contents

1	Introduction	3
1	Collision physics	3
2	Collision-induced intramultiplet mixing	4
3	Ionizing collisions	6
4	Scope of this thesis	6
2	Four-Vector correlation experiments: Simulation	9
1	Introduction	10
2	Coordinate frames	11
3	Scattering analysis	16
4	Cross section expression	18
5	Concluding remarks	20
A	Numerical checks	22
B	Fundamental B coefficients	23
3	Four-Vector correlation experiment on Ne(3p) + He collisions: measurements on intramultiplet mixing	29
1	Introduction	30
2	Final-state analysis	32
3	Experimental setup	37
4	Doppler probing of Ne($3s, {}^3P_0, {}^3P_2$) elastic scattering	41
5	Ne($3p, \alpha_7$) elastic scattering	43
6	Ne($3p, \alpha_9 \rightarrow \alpha_8$) inelastic scattering	46
7	Comparison with theory	50
8	Concluding remarks	53
A	LIF-scheme for detecting small angle elastic scattering	54
B	Competing processes in the LIF signal for elastic scattering	55
4	Ionization widths for Ne($3l$)-Ar systems ($l=s,p$)	59
1	Introduction	60
2	Calculation of ionization widths	61
3	Ionization widths for Ne($3s, 3p$)-Ar	64
4	Coupled channels calculation with optical potentials	72
5	Cross sections for Ne($3p$)-Ar	77
6	Cross sections for Ne($3s$)-Ar	82
7	Concluding remarks	86
5	Calculation of Two-center Integrals	89
1	Introduction	90
2	Preliminaries	92
3	Numerical Methods	95
4	STO expansion of free electron wave function	98

5	Test of numerical code	105
6	Performance	107
7	Conclusion	113
A	Free electron wave function in Ar^+ -potential	114
B	Corrected recurrence relations	114
	Concluding remarks	116
	Summary	119
	Samenvatting	121
	Dankwoord	123



1

Introduction

1 Collision physics

The energy scale of experimental collision physics, as depicted in Fig. 1, covers at least 20 decades. On the far end of the scale high energy physics takes place, on the lower end of the scale nano Kelvin physics. Recently, several great breakthroughs have occurred at both ends of this energy scale. Examples are the discovery of the Z^0 and W^\pm vector bosons at collision energies of 80 GeV and 90 GeV, respectively, at CERN by the UA1, UA2 and LEP groups¹⁻⁴ and the experimental observation of Bose-Einstein condensation in Rb and Li gas samples at a temperature of 20 nK (corresponding with 2×10^{-12} eV) in groups at JILA, Boulder,⁵ at MIT, Cambridge⁶ and at Rice University, Houston.⁷ Many brilliant scientists seem to be interested only in either one of the extreme ends of this energy scale, which might suggest that no interesting research is being done for energies inbetween. However, in this thesis collisions are described that are located exactly in the middle of this energy scale, *viz.* in the range 0.1–1 eV. Although these kind of collisions are more related to everyday physics as can be found in ordinary fluorescence lamps or gas-discharge lasers operating at room-temperature, the aim of this study is rather fundamental, namely gaining insight into the dynamics of the collisions.⁸⁻¹⁰

As ingredients for this study we have both experiment and theory. On the one side experiments performed with crossed atomic beams where lasers select the initial and

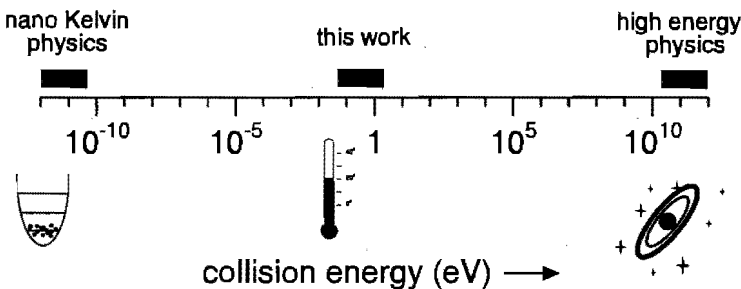


Figure 1: The energy scale of collision physics.



final states. On the other side we have two collision models, quantum and semiclassical, which use interaction potentials as input. Experiment and theory are very interesting in their own right, but real insight can only be gained by confronting the results from both sides. This ‘mixture’ of experiment and theory is reflected in the unique collaboration between the experimental Atomic Collisions and Quantum Electronics group and the theoretical Atomic Physics and Quantum Electronics group of the Physics Department of Eindhoven University of Technology.

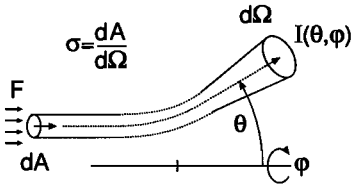


Figure 2: Definition of cross section: a flux F of particles hits the area dA and is scattered in a cone $d\Omega$ along (θ, φ) with intensity $I(\theta, \varphi)$. Conservation of particles yields $F dA = I(\theta, \varphi) d\Omega$.

Both experiment and theory result in a differential cross sections $\sigma(\theta, \varphi)$ which describes the scattering probability in terms of the area dA which has to be hit by the incoming particles in order to end up in the scattering cone with solid angle $d\Omega$, as depicted in Fig. 2. Experimentally, this differential cross section is integrated over the detection solid angle and results in a total cross section Q which has the dimension m^2 .

In this thesis two processes are studied which occur in collisions of excited Ne atoms with ground-state rare gas atoms: *i*) the intramultiplet mixing process and *ii*) ionizing collisions. These two processes will be introduced in the following sections.

2 Collision-induced intramultiplet mixing

Collisions are studied between excited Ne atoms and ground-state He atoms. Two metastable Ne(3s) states, 3P_0 and 3P_2 , are produced in a thermal discharge source. Next, a laser excites one of these metastable Ne(3s) states to a short-lived Ne(3p) state ($\tau \approx 20$ ns). In the Ne(3p) multiplet ten different fine structure levels can be distinguished. Due to the collision with a ground state He atom, the initial Ne(3p, α_i) state can make a transition to a final Ne(3p, α_f) state. This process is referred to as intramultiplet mixing or a fine-structure changing collisions.

These fine structure transitions have been studied with increasing detail. The first experiments were performed in gas-discharges. Only information in terms of rate constants could be obtained. Subsequently the process was studied in more detail in a crossed-beam setup in which a polarized laser beam is used to prepare an aligned Ne(3p) state. In this setup the total cross section Q can be determined as a function of the well-defined collision energy and the non-isotropic character of the Ne(3p) states.

An important parameter in this experiment is the polarization of the laser which determines the alignment of the initial state. The relation between laser polarization and the initial state orbitals is shown in Fig. 3. As a function of the alignment of the initial state the cross sections for different transitions Ne(3p, $\alpha_i \rightarrow \alpha_f$) have been studied by Manders *et al.*¹¹ and Boom *et al.*¹² for collision energies in the ranges 0.07–0.14 eV

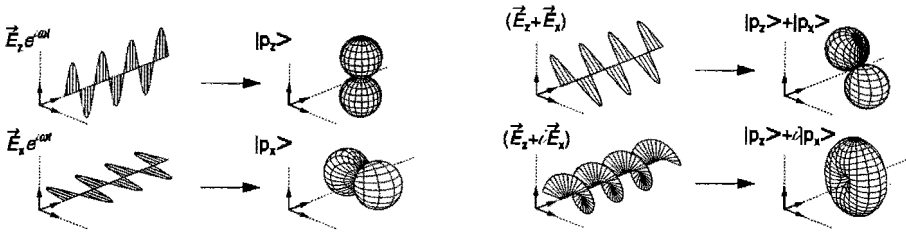


Figure 3: Orbital shapes for different pump laser polarizations. Linear laser polarizations correlate directly with p-orbitals which are aligned parallel to the polarization vector. In case of circular laser polarization a ‘rotating disk’ is excited whose rotation-sense reflects the handed-ness of the laser polarization.

and 0.5–1.5 eV, respectively. Since two vector quantities (initial velocity and alignment) can be actively controlled this is a two-vector correlation experiment.

The experiment discussed in the first part of this thesis goes one step further. Besides controlling the initial state as described above, we also probe the final state. An enormous amount of extra information regarding the collision dynamics can be obtained. However, probing the final state is not trivial, because the lifetime of scattered Ne(3p) states is typically 20 ns. Therefore, we use a laser-induced fluorescence technique¹³ where an extra ‘probe’ laser excites the final state to a higher multiplet from which the fluorescence is monitored. This is depicted in Fig. 4. Again, by varying the polarization of this probe laser, information on the alignment of the final state can be obtained. This LIF-technique can be combined with a Doppler probing scheme: the

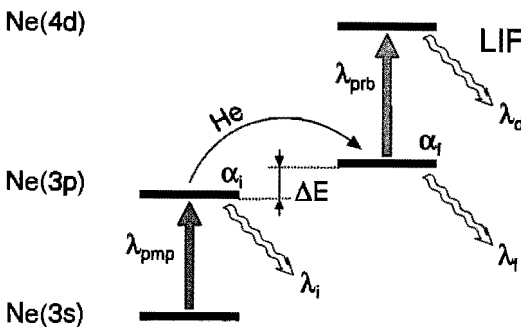


Figure 4: Pump-probe scheme for an inelastic Ne(3p, $\alpha_i \rightarrow \alpha_f$) transition caused by the collision with He. A pump (λ_{pmp}) and probe (λ_{prb}) laser are used to produce the initial state and probe the final state, respectively. The laser-induced fluorescence (LIF) is monitored (λ_d).

detuning of the probe laser selects a class of final states having a certain velocity component along the probe laser beam. This class corresponds to a cone about the probe laser direction as is shown in Fig. 5. Summarizing, we can perform differential cross section measurements as a function of four vector quantities: the initial and final velocity and the alignment of the initial and final state. In that sense we have a state-to-state analysis which we call a four-vector correlation experiment.

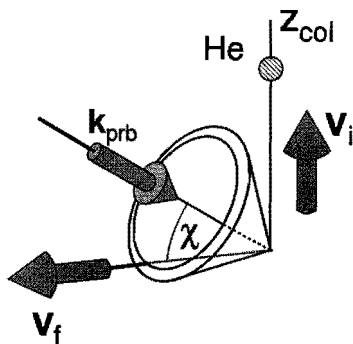


Figure 5: The Doppler cone which corresponds with the class of atoms having a well-defined velocity component along the probe laser beam. The Doppler effects determines the relation between laser detuning and the polar-angle χ .

3 Ionizing collisions

If the excitation energy of the Ne atom exceeds the ionization energy of the ground-state collision partner, the extra channel of ionization opens up. This phenomenon was first discovered by Penning who measured the ionization coefficients in discharges of mixtures of noble gases.¹⁴ Small admixtures of for example Ar in a He discharge had an enormous effect. The ionization process in the collision is described as a loss rate from the Ne(3p)-Ar system to the ionized Ne-Ar⁺ channel. Using the Heisenberg uncertainty principle $\Delta E \Delta t \geq \hbar$, we can relate the finite lifetime of the Ne(3p)-Ar system to an energy width $\Gamma(R)$. The corresponding ionization rate $\Gamma(R)/\hbar$ depends on the internuclear distance R between the colliding atoms. The trajectories of the colliding atoms are governed by the interaction potential $V(R)$. Ionization can be implemented in this classical description by defining a complex potential, usually called the optical potential, where the ionization process is incorporated through the imaginary part

$$V_{\text{opt}}(R) = V(R) - \frac{1}{2}i\Gamma(R).$$

This optical potential can also be used in a quantum mechanical description. The role of the imaginary term in the optical potential can be compared with the attenuation of a lightwave in a medium with a complex-valued refraction index (see Fig. 6). Quantum mechanically, this attenuation of the wave function describes exactly the ionization probability.

4 Scope of this thesis

Based on the two processes occurring in collisions of excited Ne atoms with ground-state rare gas atoms, this thesis can be divided in two parts.

In the first part the intramultiplet mixing process is studied. Chapters 2 and 3 are devoted to a novel four-vector correlation experiment on excited Ne atoms with ground-state He collisions. In Chapter 2 we give a novel description of the quantum mechanical framework for a four-vector correlation experiment, which is essential for an efficient numerical simulation of the experiment. In Chapter 3 the first results of

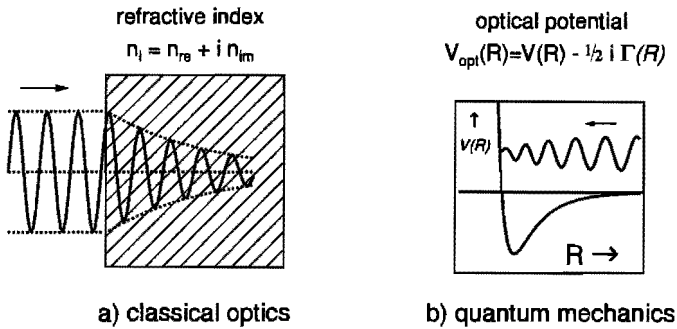


Figure 6: Optical analogue of a complex potential. a) In classical optics the attenuation of a lightwave is described by a complex-valued refractive index. b) In quantum mechanics the atomic wave function attenuates and loses flux to the ionization channel, which is described by the optical potential.

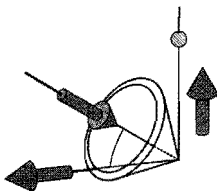
the four-vector correlation experiment are presented. Using the quantum simulations of Chapter 2 the measured results are discussed.

The second part of this thesis treats the quantum mechanical description of the ionization processes occurring in excited Ne-Ar collisions. In Chapter 4 *ab initio* calculations for ionization widths for the Ne(3s)-Ar and Ne(3p)-Ar systems are presented. As an application of these ionization widths we use them as input for a modified quantum calculation and compare the results with experimental data. The calculation of the *ab initio* ionization widths necessitates the evaluation of intricate two-center two-electron integrals. Chapter 5 deals with the calculation of these integrals.

References

- [1] G. A. *et al.*, *Phys. Lett.* **166B**, 484 (1986).
- [2] J. A. *et al.*, *Z. Phys.* **C30**, 1 (1986).
- [3] B. A. *et al.*, *Nucl. Instr. and Meth.* **A289**, 35 (1990), 13 Collaboration.
- [4] D. D. *et al.*, *Nucl. Instr. and Meth.* **A294**, 121 (1990), *aleph* Collaboration.
- [5] M. Andersen, J. Ensher, M. Matthews, C. Wieman, and E. Cornell, *Science* **269**, 198 (1995).
- [6] K. Davis, M.-O. Mewes, M. Andrews, N. van Druten, D. Durfee, D. Kurn, and W. Ketterle, *Phys. Rev. Lett.* **75**, 3969 (1995).
- [7] C. Bradley, C. Sackett, J. Tollett, and R. Hulet, *Phys. Rev. Lett.* **75**, 1678 (1995).
- [8] J. Parson, T. Schaefer, F. Tully, P. Siska, Y. Wong, and Y. Lee, *J. Chem. Phys.* **55**, 2123 (1970).
- [9] P. Siska, J. Parson, T. Schaefer, F. Tully, P. Siska, Y. Wong, and Y. Lee, *Phys. Rev. Lett.* **25**, 271 (1970).
- [10] P. Siska, *Rev. Rev. Mod. Phys.* **65**, 337 (1993), and references cited herein.
- [11] M. Manders, W. Ruyten, F. v.d. Beuken, J. Driessen, W. Veugelers, P. Kramer, E. Vredendregt, W. van Hoek, G. Sandker, H. Beijerinck, and B. Verhaar, *J. Chem. Phys.* **89**, 4777 (1988).
- [12] W. Boom, R. van Galen, B. Klaver, S. Op de Beek, J. Heier, H. Beijerinck, and B. Verhaar, *Phys. Rev. A* **51**, 3837 (1995).
- [13] C. Smith, J. Driessen, L. Eno, and S. Leone, *J. Chem. Phys.* **96**, 8212 (1992).
- [14] F. Penning, *Naturwissenschaften* **15**, 81 (1927).





2

Four-Vector correlation experiments: Simulation of Doppler probed differential cross sections

S.S. Op de Beek, J.P.J. Driessen, H.C.W. Beijerinck, and B.J. Verhaar

Theoretical expressions for scattering cross sections in the center-of-mass (c.m.) system are derived to describe elastic and intramultiplet mixing collisions of the $\text{Ne}(3p) - \text{He}$ system where both the initial and the final state are prepared and probed, respectively, by polarized lasers. The basis of these expressions is formed by transition matrix elements calculated with a coupled channels code. The polarization configuration is described by density matrices. By separating the differential cross section expression in a part comprehending the collisional quantum numbers and the transition matrix elements and a part only depending on the scattering direction (θ, ϕ) , the computational time remains manageable. For a typical calculation a reduction in computational effort with a factor 10^5 can be gained. The detuning δ_{prb} of the probe laser selects the final velocity component along the laser beam. In our theoretical description we combine the density matrices with the differential cross sections tensor and give an expression of the Doppler cross section as a function of δ_{prb} .

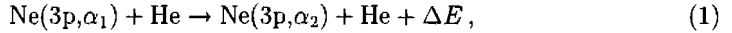


1 Introduction

Detailed information about the potential curves which govern the collision dynamics can be obtained by performing alignment (and orientation) experiments in a crossed-beam apparatus.¹⁻³ Using polarized laser beams the alignment of the initial (final) states can be controlled (determined) with respect to the initial relative velocity vector \mathbf{v}_i . These three experimentally controlled vectors can be combined with the final relative velocity vector \mathbf{v}_f to result in a so-called four-vector correlation experiment.³

Numerous theoretical studies give expressions for the cross section tensor, whose matrix representation depends on the choice of the coordinate frame. This cross section tensor describes how the initial state is transformed into a final state. When analyzing an experiment with these theoretical expressions, or when doing numerical simulations based on these expressions, it is important to translate experimental configurations correctly into density matrices.

We study collision-induced fine-structure transitions for the system



where α_1 and α_2 denote the initial and final fine-structure state of the excited Ne(3p) atom. The four vectors are defined in the following way. The experiment is performed in a crossed-beam setup [**vector 1** : initial relative velocity \mathbf{v}_i]. The initial state Ne(3p, α_1) is excited by a pump laser beam (pmp), resulting in a well-defined oriented/aligned state with respect to the laser polarization vector [**vector 2** : linear \mathbf{E}_{pmp} ; circular \mathbf{k}_{pmp}]. The final state Ne(3p, α_2) is investigated through a LIF-technique (laser-induced fluorescence) with a probe laser beam (prb). Through the Doppler effect the narrow linewidth of this probe laser selects only those scattered states which have a well-defined velocity component with respect to the laser beam direction [**vector 3** : \mathbf{v}_f]. Additionally, we obtain information about the orientation/alignment of the final state since the probe laser beam depletes a subset of magnetic sublevels with respect to the laser polarization [**vector 4** : linear \mathbf{E}_{prb} ; circular \mathbf{k}_{prb}].

The basis of the theoretical study is formed by the transition matrices calculated in a coupled channels model. As input of this calculation we use ab initio potentials calculated by Hennecart *et al.*⁴ These transition matrices have been used successfully in analyzing total cross section data and polarized-atom cross sections in the thermal and superthermal collision energy range.^{1,2}

In this paper we set up a general analysis of a four-vector correlation experiment performed on the system in Eq. (1) where all possible degrees of freedom in the experimentally controlled vector quantities are taken into account. The most important feature of this analysis is the transformation of these vector quantities in different coordinate systems. An exact definition of rotation axes and accompanying angles of these transformations is essential. These aspects are described in full detail in Section 2. In essence, the experimental configuration is contained in two density matrices for the initial and final states. In contrast, the cross section tensor describes the collision process and does not depend on the experimental arrangement. In Section 3 we describe a method for separating the differential cross section tensor $\sigma(\theta, \phi)$ in a part related

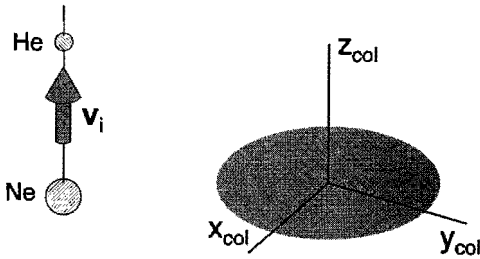


Figure 1: Collision frame $(x_{\text{col}}, y_{\text{col}}, z_{\text{col}})$: the azimuthal orientation of the x_{col} - and y_{col} -axes can be chosen arbitrarily in the collision frame.

to the coupled channels calculation and a geometrical part which depends on the scattering angles (θ, ϕ) . This separation is the key to an efficient calculation method of differential cross sections. Combining this differential cross section tensor with the two density matrices yields an expression for the experimental cross sections as is discussed in Section 4.

2 Coordinate frames

To perform a quantum mechanical analysis of the collision-induced transition of Eq. (1), we have to define four coordinate frames that will be used for describing the initial and final excited states, and for describing the initial and final nuclear motion.

2.1 Collision frame - initial nuclear motion

In quantum scattering calculations the initial nuclear motion is represented by a plane wave $e^{-i\mathbf{k}\cdot\mathbf{R}}$, with $\hbar\mathbf{k}=\mu\mathbf{v}_i$, where μ denotes the reduced mass. This plane wave is expanded into a series of spherical harmonics $Y_{N,M}(\theta, \phi)$, which are eigenstates of the nuclear angular momentum:⁵

$$e^{-i\mathbf{k}\cdot\mathbf{R}} = 4\pi \sum_{N=0}^{\infty} \sum_{M=-N}^N i^N j_N(kR) Y_{N,M}^*(\hat{\mathbf{k}}) Y_{N,M}(\hat{\mathbf{R}}), \quad (2)$$

with $j_N(kR)$ being a spherical Bessel function. If one chooses the quantization axis along $\hat{\mathbf{k}}$ with polar angles $(\theta, \phi)=(0,0)$, as depicted in Fig. 1, the plane wave expansion of Eq. (2) obtains the simpler form

$$\begin{aligned} e^{-i\mathbf{k}\cdot\mathbf{R}} &= 4\pi \sum_{N=0}^{\infty} i^N \sqrt{\frac{2N+1}{4\pi}} j_N(kR) Y_{N,0}(\hat{\mathbf{R}}) \\ &= \sum_{N=0}^{\infty} i^N (2N+1) j_N(kR) P_N(\cos\theta), \end{aligned} \quad (3)$$

where $P_N(\cos\theta)$ denotes a Legendre polynomial. The number of partial waves is greatly reduced in this so-called **collision frame** $(x_{\text{col}}, y_{\text{col}}, z_{\text{col}})$, in which \mathbf{v}_i [vector **1**] serves as the quantization axis. A visualization of this ‘collision frame’ is given in Fig. 1. Partial waves upto $N = \mathcal{O}(100)$ have to be taken into account in a typical thermal collision.

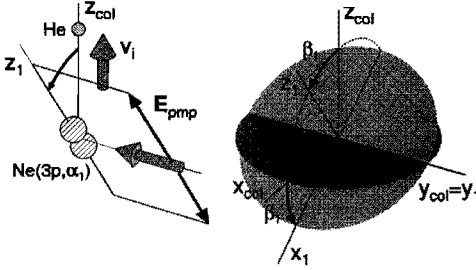


Figure 2: Preparation frame (x_1, y_1, z_1) : by choosing the direction of the laser beam axis along the 'collision frame' y_{col} -axis, only one non-zero angle β_1 is needed for the transformation between the 'collision' and 'preparation frame'.

2.2 Preparation frame - initial excited state

The optical excitation is described most easily with respect to the laser polarization vector [**vector 2**], which serves as the quantization axis in the so-called **preparation frame** (x_1, y_1, z_1) . The absorbed laser photon is now represented by a single magnetic substate, *linear* $|1, 0\rangle$; *circular* $|1, \pm 1\rangle$, which is azimuthally symmetric about the z_1 -axis. Notice that the laser-excited state $\text{Ne}(3p, \alpha_1)$ also demonstrates this azimuthal symmetry in the 'preparation frame'.

Seeing that the azimuthal orientation of the x_{col} - and y_{col} -axes is arbitrary (Fig. 1), we now fix this azimuthal orientation such that the preparation laser is directed along the y_{col} -axis, as is shown in Fig. 2. This is possible because in our experiment we always have $\mathbf{k}_{pmp} \perp \mathbf{v}_1$. Now, the relative orientation of the z_1 -axis with respect to the 'collision frame' can be characterized by the angle β_1 . Of course, since the azimuthal orientation of the 'collision frame' is no longer arbitrary, each additional vector quantity will have to be characterized by two non-arbitrary angles; one polar angle and an azimuthal orientation with respect to the 'collision frame'. This azimuthal angle characterizes the coherence of the collision process.⁶

The 'preparation frame' (x_1, y_1, z_1) can be obtained by rotating the 'collision frame' over the Euler angles $(\varphi_1, \beta_1, \gamma_1 = 0)$. First a counterclockwise rotation φ_1 about z_{col} carries the y_{col} -axis into the y_1 -axis. Subsequently, a counterclockwise rotation β_1 about this rotated y_{col} -axis carries the z_{col} -axis into the desired z_1 -axis. In principle, the azimuthal orientation of the x_1 and y_1 -axes about the z_1 -axis can be altered with a third Euler angle γ_1 , which we have chosen to be zero in our analysis. In case of a *linear* laser polarization we get only one variable Euler angle $(0, \beta_1, 0)$ depending on the specific polarization used; for *circular* laser polarizations all Euler angles are fixed $(\pi/2, \pi/2, 0)$ and applying RHC or LHC light is the only degree of freedom.

Note that a single magnetic substate $|j_1, \mu_1\rangle$ given in the 'preparation frame' can be expressed as a linear superposition of substates $|j_1, m_1\rangle$ in the 'collision frame' through a rotation over the same Euler angles. This transformation by the rotation operator $\mathcal{R}(\varphi_1, \beta_1, \gamma_1)$ with the Euler angles $(\varphi_1, \beta_1, \gamma_1)$ is written as

$$\begin{aligned} |j_1, \mu_1\rangle_{z_1} &= \sum_{m_1} [z_{col} \langle j_1, m_1 | \mathcal{R}(\varphi_1, \beta_1, \gamma_1) | j_1, \mu_1 \rangle_{z_1}] |j_1, m_1\rangle_{z_{col}} \\ &= \sum_{m_1} D_{m_1 \mu_1}^{j_1}(\varphi, \beta_1, \gamma_1) |j_1, m_1\rangle_{z_{col}}. \end{aligned} \quad (4)$$

In case of a *linear* laser polarization the Euler angles $(0, \beta_1, 0)$ give:

$$|j_1, \mu_1\rangle_{z_1} = \sum_{m_1} D_{m_1 \mu_1}^{j_1}(0, \beta_1, 0) |j_1, m_1\rangle_{z_{\text{col}}}. \quad (5)$$

If the laser is *circularly* polarized, the Euler angles are fixed $(\pi/2, \pi/2, 0)$ and we obtain

$$|j_1, \mu_1\rangle_{z_1} = \sum_{m_1} D_{m_1 \mu_1}^{j_1}\left(\frac{\pi}{2}, \frac{\pi}{2}, 0\right) |j_1, m_1\rangle_{z_{\text{col}}}. \quad (6)$$

The initial state $\text{Ne}(3p, \alpha_1)$ is excited from the lower $\text{Ne}(3s, {}^3P_0$ or ${}^3P_2)$ level. The degeneracy of the 3P_2 results in a weighted distribution (g_{μ_1}) of incoherently populated magnetic substates $|j_1, \mu_1\rangle$ in the ‘preparation frame’. This so-called ‘mixed state’ can be described with the density-matrix formalism.⁷ The density operator ρ for this initial state is represented in the ‘preparation frame’ as a weighted sum of ‘outer products’

$$\rho = \sum_{\mu_1} g_{\mu_1} |j_1, \mu_1\rangle \langle j_1, \mu_1|. \quad (7)$$

We will need the density matrix representation of the initial state in the ‘collision frame’ in the following scattering analysis. The corresponding density matrix elements ρ_{m_1, m'_1} can be found by sandwiching the density operator ρ of Eq. (7) between two magnetic sublevels $|j_1, m_1\rangle$ in the ‘collision frame’. In case of a *linear* laser polarization, we can use Eq. (5) to find

$$\begin{aligned} \rho_{m_1, m'_1} &= \langle j_1, m_1 | \rho | j_1, m'_1 \rangle = \sum_{\mu_1} g_{\mu_1} \langle j_1, m_1 | j_1, \mu_1 \rangle \langle j_1, \mu_1 | j_1, m'_1 \rangle \\ &= \sum_{\mu_1} g_{\mu_1} D_{m_1 \mu_1}^{j_1}(0, \beta_1, 0) D_{m'_1 \mu_1}^{j_1*}(0, \beta_1, 0), \end{aligned} \quad (8)$$

whereas for a *circular* laser polarization Eq. (6) gives

$$\rho_{m_1, m'_1} = \sum_{\mu_1} g_{\mu_1} D_{m_1 \mu_1}^{j_1}\left(\frac{\pi}{2}, \frac{\pi}{2}, 0\right) D_{m'_1 \mu_1}^{j_1*}\left(\frac{\pi}{2}, \frac{\pi}{2}, 0\right). \quad (9)$$

2.3 Doppler frame - final nuclear motion

Next, we introduce the so-called **Doppler frame** (x_d, y_d, z_d) where the direction $\hat{\mathbf{k}}_{\text{prb}}$ of the probe laser beam [**vector 3**] serves as the quantization axis. Due to the Doppler effect the probe laser is only resonant with final states $\text{Ne}(3p, \alpha_2)$ which are scattered into a cone around the z_d -axis with top angle χ . In this manner we are able to investigate the velocity \mathbf{v}_f of the scattered state. The relative orientation of the z_d -axis in the ‘collision frame’ is given by two polar angles (ψ, ϕ) with ψ the top angle and ϕ the azimuthal angle, as is shown in Fig. 3.

The ‘Doppler frame’ (x_d, y_d, z_d) can be obtained by rotating the ‘collision frame’ over the Euler angles $(\phi, \psi, 0)$. By choosing the third Euler angle $\xi=0$, the azimuthal orientation of the y_d -axis is fixed in the $(x_{\text{col}}, y_{\text{col}})$ -plane (Fig. 3). The choice of the ‘Doppler frame’ is thus independent of the type of laser polarization.

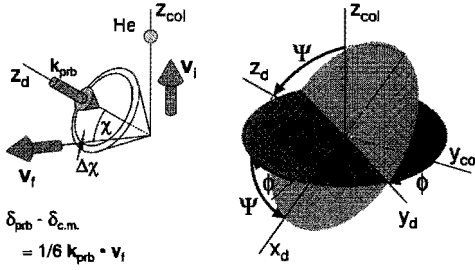


Figure 3: Doppler frame (x_d, y_d, z_d) : two Euler angles ψ and ϕ are needed to transform the ‘collision frame’ into the ‘Doppler frame’. The Doppler effect selects those final states which are scattered into a cone with top-angle χ , which depends on the laser detuning δ_{prb} , and angular spread $\Delta\chi$, which is sensitive to the laser linewidth γ_{prb} .

In Fig. 3 a ‘Doppler cone’ around the z_d -axis is displayed in order to elucidate the Doppler probing mechanism. The top angle χ of the ‘Doppler cone’ depends on the laser detuning δ_{prb} through the relation

$$\begin{aligned} \delta_{\text{prb}} &= \mathbf{k}_{\text{prb}} \cdot \mathbf{v}_{\text{Ne},f} = \mathbf{k}_{\text{prb}} \cdot \left(\mathbf{v}_{\text{c.m.}} + \frac{m_{\text{He}}}{m_{\text{Ne}} + m_{\text{He}}} \mathbf{v}_f \right) \\ &= \mathbf{k}_{\text{prb}} \cdot \left(\mathbf{v}_{\text{c.m.}} + \frac{1}{6} \mathbf{v}_f \right) = \delta_{\text{c.m.}} + \frac{1}{6} k_{\text{prb}} v_f \cos(\chi), \end{aligned} \quad (10)$$

where we have used a transformation from the center-of-mass (c.m.) frame into the laboratory frame to calculate the final velocity $\mathbf{v}_{\text{Ne},f}$ of the neon atom. The center-of-mass velocity $\mathbf{v}_{\text{c.m.}}$ results in a laser detuning offset $\delta_{\text{c.m.}}$. Thus, by varying both the probe laser direction (ψ, ϕ) and the laser detuning δ_{prb} we can explore the distribution of the final relative velocity \mathbf{v}_f in great detail.

The angular spread $\Delta\chi$ of the ‘Doppler cone’ is determined by the linewidth γ_{prb} of the probe laser, the linewidth $\Gamma = (2\pi)/\tau$ of the probing transition and the χ -dependence of the laser detuning δ_{prb} of Eq. (10). The smallest angular spread $\Delta\chi$ is determined by Γ and is obtained when a narrow laser linewidth is used ($\gamma_{\text{prb}} \ll \Gamma$). When $\gamma_{\text{prb}} \geq \Gamma$ the angular spread $\Delta\chi$ of the ‘Doppler cone’ increases, resulting in a scrambling of the velocity resolution. On the other hand, the experimental signal increases since more final states are probed. In the extreme situation that the laser linewidth is larger than the Doppler broadening of the scattering sphere, we no longer obtain information of the final relative velocity \mathbf{v}_f . In that case the experiment is reduced to a three-vector correlation study,⁸ but of course the signal strength is much larger. Which linewidth of the probe laser will be used in the experiment will depend on the attainable signal-to-noise ratio in the crossed-beam setup.

2.4 Probe frame - final excited state

Finally, we define the so-called **probe frame** (x_2, y_2, z_2) where the polarization vector of the probe laser beam [**vector 4**] serves as the quantization axis. In the ‘probe frame’ the absorbed laser photon is represented by a single magnetic substate, *linear* $|1, 0\rangle$; *circular* $|1, \pm 1\rangle$, which is azimuthally symmetric about the z_2 -axis. Therefore, the ‘probe frame’ is defined analogous to the ‘preparation frame’. Depending on the optical selection rules, a subset of magnetic sublevels is depleted incoherently. The

resulting laser-induced fluorescence (LIF) directly reflects the population distribution of this probed subset, and the orientation/alignment of the final state $\text{Ne}(3p, \alpha_2)$ is investigated. Notice that only the selection rules for Δm -transitions determine the LIF signal strength.

The orientation of the ‘probe frame’ is defined most straightforward with respect to the ‘Doppler frame’. In case of a *circular* probe laser polarization, the ‘probe frame’ coincides with the ‘Doppler frame’, and no extra angles are needed. However, when we are dealing with a *linearly* polarized laser, two angles $(\pi/2, \xi)$ are needed to denote the direction of the polarization vector \mathbf{E}_{prb} . The angle ξ characterizes the azimuthal orientation of the laser polarization about the laser beam axis, as is shown in Fig. 4.

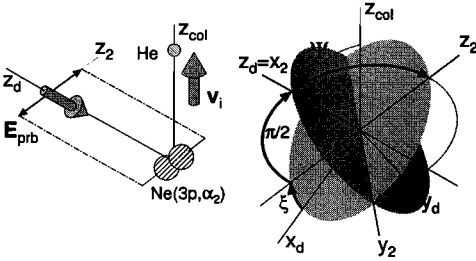


Figure 4: Probe frame (x_2, y_2, z_2) : two Euler angles ξ and $\pi/2$ are needed to transform the ‘Doppler frame’ into the ‘probe frame’. First, a rotation ξ about the z_d -axis aligns the x_d -axis along the laser polarization \mathbf{E}_{prb} . Next, a rotation $\pi/2$ about the y_2 -axis carries the z_d -axis into the z_2 -axis.

The subset of magnetic substates $|j_2, \mu_2\rangle$ can be characterized as a ‘mixed state’ with weight factors g_{μ_2} being either 0 or 1, depending on the optical selection rules. The corresponding density matrix representation of this ‘mixed state’ in the ‘collision frame’ is given by

$$\rho_{m_2, m'_2} = \langle j_2, m_2 | \rho | j_2, m'_2 \rangle = \sum_{\mu_2} g_{\mu_2} \langle j_2, m_2 | j_2, \mu_2 \rangle \langle j_2, \mu_2 | j_2, m'_2 \rangle. \quad (11)$$

To calculate these density matrix elements, we have to transform the individual magnetic substates $|j_2, \mu_2\rangle$ from the ‘probe frame’ to the ‘collision frame’. For a *linear* laser polarization this substate $|j_2, \mu_2\rangle$ is first rotated by the Euler angles $(\xi, \pi/2, 0)$ resulting in a linear superposition of substates $|j_2, \mu'_2\rangle$ defined in the ‘Doppler frame’, followed by a rotation by the Euler angles $(\phi, \psi, 0)$ connecting the ‘Doppler frame’ and the ‘collision frame’

$$\begin{aligned} |j_2, \mu_2\rangle_{z_2} &= \sum_{\mu'_2} D_{\mu'_2 \mu_2}^{j_2}(\xi, \frac{\pi}{2}, 0) |j_2, \mu'_2\rangle_{z_d} \\ &= \sum_{\mu'_2} D_{\mu'_2 \mu_2}^{j_2}(\xi, \frac{\pi}{2}, 0) \sum_{m''_2} D_{m''_2 \mu'_2}^{j_2}(\phi, \psi, 0) |j_2, m''_2\rangle_{z_{\text{col}}}. \end{aligned} \quad (12)$$

Combination of Eqs. (11) and (12) gives the desired density matrix elements

$$\begin{aligned} \rho_{m_2, m'_2} &= \sum_{\mu_2} \sum_{\mu'_2} \sum_{\mu''_2} g_{\mu_2} D_{\mu'_2 \mu_2}^{j_2}(\xi, \frac{\pi}{2}, 0) D_{\mu''_2 \mu'_2}^{j_2*}(\xi, \frac{\pi}{2}, 0) \\ &\quad \times D_{m_2 \mu''_2}^{j_2}(\phi, \psi, 0) D_{m'_2 \mu''_2}^{j_2*}(\phi, \psi, 0). \end{aligned} \quad (13)$$

For a circular polarization, the ‘Doppler frame’ and ‘probe frame’ coincide and we only need the rotation by the Euler angles $(\phi, \psi, 0)$ which connects the ‘Doppler frame’ with the ‘collision frame’

$$|j_2, \mu_2\rangle_{z_2} = \sum_{m_2} D_{m_2 \mu_2}^{j_2}(\phi, \psi, 0) |j_2, m_2\rangle_{z_{\text{col}}}. \quad (14)$$

Combination of Eqs. (11) and (14) gives the following density matrix elements

$$\rho_{m_2, m_2'} = \sum_{\mu_2} g_{\mu_2} D_{m_2 \mu_2}^{j_2}(\phi, \psi, 0) D_{m_2' \mu_2}^{j_2^*}(\phi, \psi, 0). \quad (15)$$

3 Scattering analysis

To derive (differential) cross sections for the collision-induced fine-structure changing transitions for the $\text{Ne}(3p, \alpha_1 \rightarrow \alpha_2) - \text{He}$ system, we need to calculate the so-called scattering amplitudes together with the density matrices of the initial and final state. The ‘collision frame’ will be used as the coordinate frame for our calculations: the scattering calculations are less complicated and the density matrix representations can be treated using Eqs. (8), (9), (13) and (15). In the ‘collision frame’ the initial relative velocity vector $\mathbf{v}_i = \hbar \mathbf{k}_1 / \mu$ is characterized by the polar angles $(0, 0)$, whereas the final relative velocity vector is given by $\mathbf{v}_f = \hbar \mathbf{k}_2 / \mu$ with scattering angles (θ, φ) .

In a full quantum mechanical treatment the scattering amplitude is calculated by solving the Schrödinger equation in a well chosen set of basis states $|\varphi_i^P\rangle$, characterized by a quantum number P for the total angular momentum which is a conserved quantity in the collision process. Implemented in a coupled channels computer program this results in the transition matrix T^P with matrix elements, $T_{j_2 N_2, j_1 N_1}^P$, with j_1 and j_2 the ‘collision frame’ quantum numbers describing the initial and final state, respectively, and N_1 and N_2 the corresponding quantum numbers defining the nuclear angular momentum. The scattering amplitudes can now be calculated from the transition matrix,⁹

$$\begin{aligned} f_{j_1, m_1 \rightarrow j_2, m_2}(\theta, \varphi) &= \frac{2\pi}{\sqrt{k_1 k_2}} i \sum_P \sum_{N_1} \sum_{N_2} (i)^{N_1 - N_2} (-)^{j_1 + j_2 + N_1 + N_2} \\ &\times (2P + 1) \begin{pmatrix} j_1 & N_1 & P \\ m_1 & 0 & -m_1 \end{pmatrix} \begin{pmatrix} j_2 & N_2 & P \\ m_2 & m_1 - m_2 & -m_1 \end{pmatrix} \\ &\times Y_{N_1, 0}^*(0, 0) T_{j_2 N_2, j_1 N_1}^P Y_{N_2, m_1 - m_2}(\theta, \varphi) \\ &= \sqrt{\frac{\pi}{k_1 k_2}} i \sum_{N_2} A(N_2, m_1, m_2) Y_{N_2, m_1 - m_2}(\theta, \varphi), \end{aligned} \quad (16)$$

where $(:::)$ denotes a Wigner 3- j symbol. This scattering amplitude is expanded in a series of spherical harmonics $Y_{N_2, m_1 - m_2}(\theta, \varphi)$ with coefficients $A(N_2, m_1, m_2)$ which are independent of the scattering direction (θ, φ) . Using the special case $\sqrt{4\pi} Y_{N_1, 0}^*(0, 0) = \sqrt{2N_1 + 1}$, we find

$$A(N_2, m_1, m_2) = \sum_P \sum_{N_1} (i)^{N_2 - N_1} (-)^{j_1 + j_2} (2P + 1) (2N_1 + 1)^{1/2}$$

$$\times \begin{pmatrix} j_1 & N_1 & P \\ m_1 & 0 & -m_1 \end{pmatrix} \begin{pmatrix} j_2 & N_2 & P \\ m_2 & m_1 - m_2 & -m_1 \end{pmatrix} T_{j_2 N_2, j_1 N_1}^P. \quad (17)$$

By taking products of two scattering amplitudes, we can construct the cross section tensor for differential scattering into the direction (θ, φ) , as given by⁹

$$\begin{aligned} \sigma_{j_1 m_1 m'_1 \rightarrow j_2 m_2 m'_2}(\theta, \varphi) &= \frac{k_2}{k_1} f_{j_1 m_1 \rightarrow j_2 m_2}(\theta, \varphi) f_{j_1 m'_1 \rightarrow j_2 m'_2}^*(\theta, \varphi) \\ &= \frac{k_2}{k_1} \frac{\pi}{k_1 k_2} \left[\sum_{N_2} A(N_2, m_1, m_2) Y_{N_2, m_1 - m_2}(\theta, \varphi) \right] \\ &\quad \times \left[\sum_{N'_2} A^*(N'_2, m'_1, m'_2) Y_{N'_2, m'_1 - m'_2}^*(\theta, \varphi) \right] \\ &= \frac{\pi}{k_1^2} \sum_{N_2} A(N_2, m_1, m_2) \sum_{N'_2} A^*(N'_2, m'_1, m'_2) \\ &\quad \times Y_{N_2, m_1 - m_2}(\theta, \varphi) (-)^{m'_1 - m'_2} Y_{N'_2, m'_2 - m'_1}(\theta, \varphi). \quad (18) \end{aligned}$$

If we substitute Eq. (17) into this differential cross section tensor a summation over both P and P' is obtained. Computationally this implies that the scattering matrices T^P have to be multiplied for every combination of P and P' . The scattering matrices are stored in files with a typical size of a few Mbytes. In Eq. (18) this file has to be accessed P_{\max}^2 times with P_{\max} the maximum value of the P -quantum number. The number of file accesses can be reduced to P_{\max} by introducing the A -coefficients in Eq. (17). First the A -coefficients are calculated and stored in a file. Subsequently, this file is used to calculate the differential cross section tensor of Eq. (18).

Equation (18) can be further simplified using the 'composition relation',^{5,10} replacing the product of the spherical harmonics with a summation over a single spherical harmonic:

$$\begin{aligned} Y_{l_1, \mu_1}(\theta, \varphi) Y_{l_2, \mu_2}(\theta, \varphi) &= \sum_{L=|l_1-l_2|}^{l_1+l_2} \sum_{M=-L}^{+L} \left[\frac{(2l_1+1)(2l_2+1)(2L+1)}{4\pi} \right]^{1/2} \\ &\quad \times \begin{pmatrix} l_1 & l_2 & L \\ 0 & 0 & 0 \end{pmatrix} \begin{pmatrix} l_1 & l_2 & L \\ \mu_1 & \mu_2 & M \end{pmatrix} (-)^M Y_{L, -M}(\theta, \varphi) \\ &= \sum_{L=|l_1-l_2|}^{l_1+l_2} \left[\frac{(2l_1+1)(2l_2+1)(2L+1)}{4\pi} \right]^{1/2} \\ &\quad \times \begin{pmatrix} l_1 & l_2 & L \\ 0 & 0 & 0 \end{pmatrix} \begin{pmatrix} l_1 & l_2 & L \\ \mu_1 & \mu_2 & -\mu_1 - \mu_2 \end{pmatrix} (-)^{-\mu_1 - \mu_2} Y_{L, \mu_1 + \mu_2}(\theta, \varphi), \quad (19) \end{aligned}$$

where we used the substitution $M \rightarrow -\mu_1 - \mu_2$. Using this 'composition relation' we can rewrite Eq. (18) as follows

$$\begin{aligned} \sigma_{j_1 m_1 m'_1 \rightarrow j_2 m_2 m'_2}(\theta, \varphi) &= \frac{\pi}{k_1^2} \sum_{N_3} B(N_3, m_1, m'_1, m_2, m'_2) \\ &\quad \times Y_{N_3, (m_1 - m_2) + (m'_2 - m'_1)}(\theta, \varphi) \quad (20) \end{aligned}$$

with

$$\begin{aligned}
 B(N_3, m_1, m'_1, m_2, m'_2) &= (-)^{m_1-m_2} \sum_{N_2} \sum_{N'_2} A(N_2, m_1, m_2) A^*(N'_2, m'_1, m'_2) \\
 &\times \left[\frac{(2N_2+1)(2N'_2+1)(2N_3+1)}{4\pi} \right]^{1/2} \begin{pmatrix} N_2 & N'_2 & N_3 \\ 0 & 0 & 0 \end{pmatrix} \\
 &\times \begin{pmatrix} N_2 & N'_2 & N_3 \\ m_1-m_2 & m'_2-m'_1 & -(m_1-m_2)-(m'_2-m'_1) \end{pmatrix}, \quad (21)
 \end{aligned}$$

where we have used $(-)^{(m'_1-m'_2)} (-)^{(m_1-m_2)+(m'_2-m'_1)} = (-)^{m_1-m_2}$. The differential cross section tensor is now expanded in a series of spherical harmonics $Y_{N_3, \tilde{m}}(\theta, \varphi)$, where we introduce the shorthand notation $\tilde{m} = (m_1 - m_2) + (m'_2 - m'_1)$. The expansion coefficients $B(N_3, m_1, m'_1, m_2, m'_2)$ are independent of the scattering angles and have to be calculated only once.

In conclusion, the procedure for calculating the differential cross section tensor is as follows. For every N_2 value in the range $0, \dots, N_{\max}$ we calculate a small $(2j_1 + 1) \times (2j_2 + 1)$ matrix $A(N_2, m_1, m_2)$. Then Eq. (21) is used to calculate all possible $B(N_3, m_1, m'_1, m_2, m'_2)$ values. Furthermore, it should be pointed out that the numerical stability of the Racah-recipe used for calculating the $3j$ -symbol is poor for large N_2, N'_2 and N_3 . To solve this numerical problem, we will use recursive relations to calculate the $3j$ symbols. These relations are described in Ref. [11].

4 Cross section expression

4.1 Differential cross section

In our experiment the orientation/alignment of the initial and final state is investigated with polarized laser beams. A cross section expression for differential scattering into the direction of $\hat{\mathbf{k}}_{\text{prb}}$ with polar angles (θ, φ) is obtained by multiplying the tensor of Eq. (20) with the density matrices and of the prepared initial state, Eq. (8) or (9), and of the probed final state, Eq. (13) or (15),

$$\begin{aligned}
 \sigma_{\text{expt}}(\theta, \varphi) &= \sum_{m_1, m'_1} \rho_{m_1, m'_1} \sum_{m_2, m'_2} \rho_{m_2, m'_2}^* \sigma_{j_1 m_1 m'_1 \rightarrow j_2 m_2 m'_2}(\theta, \varphi) \\
 &= \frac{\pi}{k_1^2} \sum_{N_3} \sum_{\tilde{m}} C(N_3, \tilde{m}) Y_{N_3, \tilde{m}}(\theta, \varphi). \quad (22)
 \end{aligned}$$

In this cross section expression the C -coefficients are expansion coefficients in a series of spherical harmonics $Y_{N_3, \tilde{m}}(\theta, \varphi)$. They are calculated with the B -coefficients of Eq. (21)

$$\begin{aligned}
 C(N_3, \tilde{m}) &= \sum_{m_1, m'_1} \rho_{m_1, m'_1} \sum_{m_2, m'_2} \rho_{m_2, m'_2}^* B(N_3, m_1, m'_1, m_2, m'_2) \\
 &\times \delta_{\tilde{m}, (m_1-m_2)+(m'_2-m'_1)}. \quad (23)
 \end{aligned}$$

The values of \tilde{m} lie within the interval $[-12, 12]$ for all possible transitions in the Ne(3p)-multiplet. For thermal energies the value of N_3 does not exceed 400, thus the array

$C(N_3, \tilde{m})$ can easily be stored. Note that for each arrangement of the four vectors, a different set of $C(N_3, \tilde{m})$ -coefficients needs to be calculated from the same set of B -coefficients.

4.2 Doppler cross section

In the experiment we measure the cross section as a function of the Doppler detuning δ_{prb} . According to Eq. (10) this corresponds with integrating the differential cross section over the ‘Doppler cone’ centered around the ‘Doppler frame’ z_d -axis with scattering angles $(\chi, \zeta = 0..2\pi)$ as is shown in Fig. 4. However, the spherical harmonics $Y_{N_3, \tilde{m}}(\theta, \varphi)$ of Eq. (22) are defined with respect to the ‘collision frame’. These spherical harmonics can be transformed into either frame

$$\begin{aligned} Y_{N_3, m_3}(\chi, \zeta) &= |N_3, m_3\rangle_{z_d} = \sum_{\tilde{m}} D_{\tilde{m}, m_3}^{N_3}(\phi, \psi, 0) |N_3, \tilde{m}\rangle_{z_c} \\ &= \sum_{\tilde{m}} D_{\tilde{m}, m_3}^{N_3}(\phi, \psi, 0) Y_{N_3, \tilde{m}}(\theta, \varphi) \\ Y_{N_3, \tilde{m}}(\theta, \varphi) &= \sum_{m_3} [D_{m_3, \tilde{m}}^{N_3}(\phi, \psi, 0)]^\dagger Y_{N_3, m_3}(\chi, \zeta) \\ &= \sum_{m_3} D_{m_3, \tilde{m}}^{N_3}(0, -\psi, -\phi) Y_{N_3, m_3}(\chi, \zeta). \end{aligned} \quad (24)$$

Using this transformation, Eq. (20) is rewritten as follows

$$\begin{aligned} \sigma_{j_1 m_1 m'_1 \rightarrow j_2 m_2 m'_2}(\chi, \zeta) &= \frac{\pi}{k_1^2} \sum_{N_3} B(N_3, m_1, m'_1, m_2, m'_2) \\ &\times \sum_{m_3} D_{m_3, \tilde{m}}^{N_3}(0, -\psi, -\phi) Y_{N_3, m_3}(\chi, \zeta). \end{aligned} \quad (25)$$

The differential cross section of Eq. (25) is integrated over the ‘Doppler cone’ of Fig. 3, which results in the so-called **Doppler cross section**

$$\sigma_{j_1 m_1 m'_1 \rightarrow j_2 m_2 m'_2}(\chi) d\chi = \int_0^{2\pi} d\zeta \sigma_{j_1 m_1 m'_1 \rightarrow j_2 m_2 m'_2}(\chi, \zeta) d\chi, \quad (26)$$

where the cone-angle χ depends on the laser detuning δ_{prb} according to Eq. (10). The integration over ζ only affects the spherical harmonic $Y_{N_3, m_3}(\chi, \zeta)$ giving

$$\begin{aligned} \int_0^{2\pi} \sum_{m_3} D_{m_3, \tilde{m}}^{N_3}(0, -\psi, -\phi) Y_{N_3, m_3}(\chi, \zeta) \sin \chi d\zeta \\ = 2\pi \sin \chi D_{0, \tilde{m}}^{N_3}(0, -\psi, -\phi) Y_{N_3, 0}(\chi, 0) \\ = 2\pi \sin \chi Y_{N_3, \tilde{m}}(\psi, \phi) P_{N_3}(\cos \chi), \end{aligned} \quad (27)$$

where we have used the relations

$$Y_{N_3, 0}(\theta, \varphi) = \left(\frac{2N_3 + 1}{4\pi} \right)^{1/2} P_{N_3}(\cos \theta), \quad (28)$$

$$D_{0, \tilde{m}}^{N_3}(0, -\psi, -\phi) = \left(\frac{4\pi}{2N_3 + 1} \right)^{1/2} Y_{N_3, \tilde{m}}(\theta, \phi). \quad (29)$$

Thus the final expression for the Doppler cross section tensor is obtained by substituting Eq. (25) into Eq. (26), and applying Eq. (27)

$$\begin{aligned} & \sigma_{j_1 m_1 m'_1 \rightarrow j_2 m_2 m'_2}(\chi) d\chi \\ &= \frac{2\pi^2}{k_1^2} \sin \chi \sum_{N_3} B(N_3, m_1, m'_1, m_2, m'_2) Y_{N_3, \bar{m}}(\psi, \phi) P_{N_3}(\cos \chi) d\chi. \end{aligned} \quad (30)$$

Finally, the experimental cross section expression can be obtained by multiplying Eq. (30) by the initial and final density matrix, which results in

$$\begin{aligned} \sigma_{\text{dopp}}(\chi) &= \sum_{m_1, m'_1} \rho_{m_1, m'_1} \sum_{m_2, m'_2} \rho_{m_2, m'_2}^* \sigma_{j_1 m_1 m'_1 \rightarrow j_2 m_2 m'_2}(\chi) \\ &= \frac{2\pi^2}{k_1^2} \sin \chi \sum_{N_3} E(N_3) P_{N_3}(\cos \chi), \end{aligned} \quad (31)$$

with

$$E(N_3) = \sum_{m_1, m'_1} \rho_{m_1, m'_1} \sum_{m_2, m'_2} \rho_{m_2, m'_2}^* \sum_{N_3} B(N_3, m_1, m'_1, m_2, m'_2) Y_{N_3, \bar{m}}(\psi, \phi). \quad (32)$$

Using the symmetry relations for the B -tensor as discussed in Appendix B we find $E(N_3) = E^*(N_3)$, *i.e.*, the E -coefficients are real valued. This is what we expect for the coefficients considering the experimental results for the differential cross section $\sigma_{\text{dopp}}(\chi)$.

5 Concluding remarks

The method presented in this paper for simulating experimental differential cross sections is mainly focussed on a reduction of computational time. As an example, we look closer at the calculations performed to visualize the differential cross section $\sigma(\theta, \phi)$ for a specific experimental configuration. The results of such a calculation is shown in Fig. 5. In this example we calculated $\sigma(\theta, \phi)$ for a $j_1 = 1$ initial state to a $j_2 = 0$ final state using Eq. (22) in a grid of 1500 (θ, ϕ) points. For every pair (θ, ϕ) this summation is performed, without the need of calculating a new set of C -coefficients. Obviously, the separation of the angular part reduces the calculation time in our example with a factor 1500. Another reduction is achieved by writing the product of summations over A coefficients $[(N_2)_{\text{max}}^2]$ in Eq. (18) in a single summation over the B -coefficients $[2(N_2)_{\text{max}}]$. Furthermore, a factor 2 is gained by using the symmetry relations of the B -tensor (see Table B3). This results in a total reduction factor in computational time of $15002(N_2)_{\text{max}}^2 / (2(N_2)_{\text{max}}) = 3 \times 10^5$ for $(N_2)_{\text{max}} = 200$ in this typical calculation. The calculation time for a visualization in Fig. 5 is typically 1 sec on an IBM RS/6000 Power PC. Without the reduction in computational time, such a calculation would be impractical.

In the expression for the Doppler cross section in Eq. (26) an integration over the angle ζ around the probe laser axis is performed. By introducing the E -coefficients in Eq.(31) this Doppler cross section is written analogous to the experimental cross section

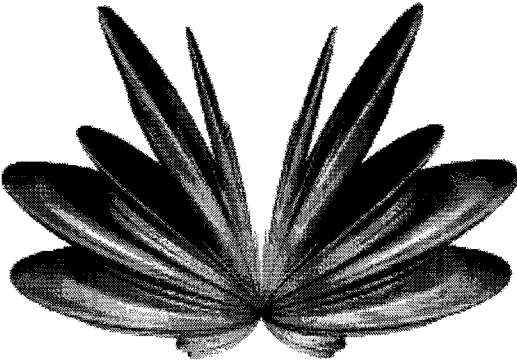


Figure 5: Visualization of the differential cross section $\sigma(\theta, \phi)$ for M_J -changing elastic collisions of $\text{Ne}(3p, \alpha_7)$ -states for a collision energy of 70 meV. A colinear linearly polarized probe-pump laser beam configuration with perpendicular polarizations is used.

expression of Eq. (22). Without the introduction of the E -coefficients the integration would have to be performed numerically, implying a calculation of the cross section tensor for every (θ, ϕ) angle pair. An accurate determination of this numerical integral would lead to an impractical number of tensor calculations.

The transition matrix elements which are calculated with the coupled channels model cannot be related directly to experimental cross sections. When only the initial state is controlled (*i.e.* a two-vector correlation experiment) the relation between the experimental cross section and the transition matrix elements is straightforward. In case of experiments where the final states is investigated as well (*i.e.* three- or four-vector correlation experiments) the experimental cross sections are complicated. The density matrix representation of the initial and final state is a compact way of describing the experimental configuration.

In the four-vector correlation experiment described in this paper, the number of controllable experimental ‘handles’ is quite large. In practice, the experiment will be preformed only as a function of a restricted number of experimental configurations. The simulation of experimental cross sections is important for investigating interesting ‘handles’ and/or configurations before the real experiment can be done.

The Doppler probing technique described in Section 2 displays an intricate integration over a ‘Doppler cone’ with top angle χ . A reverse transforming from the experimental Doppler cross section to differential cross sections in the collision frame is not straightforward. On the other hand, a simulation of the experimentally observed differential cross section as a function of the probe laser detuning δ_{prb} can directly be compared with experimental results. The general description of the experimental configuration in terms of density matrices enables us to perform simulations for a variety of experimental configurations.



Appendices

A Numerical checks

To check our computational results we will have a closer look at some of the expressions used in the calculations of the experimental Doppler cross section of Eq. (31). Our first check is to see how the A -coefficients behave if we change signs of the magnetic quantum numbers

$$\begin{aligned}
 A(N_2, -m_1, -m_2) &= \sum_P \sum_{N_1} (i)^{N_2-N_1} (-)^{j_1+j_2} (2P+1) (2N_1+1)^{1/2} \\
 &\quad \times \begin{pmatrix} j_1 & N_1 & P \\ -m_1 & 0 & m_1 \end{pmatrix} \begin{pmatrix} j_2 & N_2 & P \\ -m_2 & -m_1+m_2 & m_1 \end{pmatrix} T_{j_2 N_2, j_1 N_1}^P \\
 &= \sum_P \sum_{N_1} (i)^{N_2-N_1} (-)^{j_1+j_2} (2P+1) (2N_1+1)^{1/2} (-)^{j_1+N_1+P} (-)^{j_2+N_2+P} \\
 &\quad \times \begin{pmatrix} j_1 & N_1 & P \\ m_1 & 0 & -m_1 \end{pmatrix} \begin{pmatrix} j_2 & N_2 & P \\ m_2 & m_1-m_2 & -m_1 \end{pmatrix} T_{j_2 N_2, j_1 N_1}^P \\
 &= (-)^{j_1+j_2} A(N_2, m_1, m_2), \tag{A1}
 \end{aligned}$$

where parity conservation results in $(-)^{N_1} = (-)^{N_2}$.

Because the interaction potentials can be constructed with $3j$ -symbols, they do not depend on the sign of the magnetic quantum number. Therefore, the A -coefficients are symmetric upto a possible sign-change $(-)^{j_1+j_2}$.

We will use Eq. (A1) to examine the behavior of the B -coefficients of Eq. (21) when changing signs of the magnetic quantum numbers

$$\begin{aligned}
 B(N_3, -m_1, -m'_1, -m_2, -m'_2) &= (-)^{m_1-m_2} \sum_{N_2} \sum_{N'_2} A(N_2, -m_1, -m_2) \\
 &\quad \times A^*(N'_2, -m'_1, -m'_2) \left[\frac{(2N_2+1)(2N'_2+1)(2N_3+1)}{4\pi} \right]^{1/2} \\
 &\quad \times \begin{pmatrix} N_2 & N'_2 & N_3 \\ 0 & 0 & 0 \end{pmatrix} \begin{pmatrix} N_2 & N'_2 & N_3 \\ m_2-m_1 & m'_1-m'_2 & \tilde{m} \end{pmatrix} \\
 &= (-)^{m_1-m_2} \sum_{N_2} \sum_{N'_2} (-)^{j_1+j_2} A(N_2, m_1, m_2) \\
 &\quad \times (-)^{j_1+j_2} A^*(N'_2, m'_1, m'_2) \left[\frac{(2N_2+1)(2N'_2+1)(2N_3+1)}{4\pi} \right]^{1/2} \\
 &\quad \times \begin{pmatrix} N_2 & N'_2 & N_3 \\ 0 & 0 & 0 \end{pmatrix} \begin{pmatrix} N_2 & N'_2 & N_3 \\ m_1-m_2 & m'_2-m'_1 & -\tilde{m} \end{pmatrix} \\
 &= B(N_3, m_1, m'_1, m_2, m'_2), \tag{A2}
 \end{aligned}$$

in which the symmetry relations of the $3j$ -symbols are applied. Again we used the shorthand notation $\tilde{m} = (m_1 - m_2) + (m'_2 - m'_1)$. Another symmetry relation for the B -coefficients can be found by interchanging the primed and unprimed quantum numbers.

$$\begin{aligned}
B(N_3, m'_1, m_1, m'_2, m_2) &= (-)^{m'_1 - m'_2} \sum_{N'_2} \sum_{N_2} A(N'_2, m'_1, m'_2) A^*(N_2, m_1, m_2) \\
&\times \left[\frac{(2N'_2 + 1)(2N_2 + 1)(2N_3 + 1)}{4\pi} \right]^{1/2} \begin{pmatrix} N'_2 & N_2 & N_3 \\ 0 & 0 & 0 \end{pmatrix} \\
&\times \begin{pmatrix} N'_2 & N_2 & N_3 \\ m'_1 - m'_2 & m_2 - m_1 & \tilde{m} \end{pmatrix} \\
&= (-)^{m'_1 - m'_2} \sum_{N_2} \sum_{N'_2} A^*(N_2, m_1, m_2) A(N'_2, m'_1, m'_2) \\
&\times \left[\frac{(2N_2 + 1)(2N'_2 + 1)(2N_3 + 1)}{4\pi} \right]^{1/2} \begin{pmatrix} N_2 & N'_2 & N_3 \\ 0 & 0 & 0 \end{pmatrix} \\
&\times \begin{pmatrix} N_2 & N'_2 & N_3 \\ m_1 - m_2 & m'_2 - m'_1 & -\tilde{m} \end{pmatrix} \\
&= (-)^{\tilde{m}} B^*(N_3, m_1, m'_1, m_2, m'_2). \tag{A3}
\end{aligned}$$

With the above symmetry relations, (A2) and (A3), we can now look into the symmetry properties of the E -coefficients of Eq. (32).

$$\begin{aligned}
E(N_3) &= \sum_{m_1, m'_1} \rho_{m_1, m'_1} \sum_{m_2, m'_2} \rho_{m_2, m'_2}^* \sum_{N_3} B(N_3, m_1, m'_1, m_2, m'_2) Y_{N_3, \tilde{m}}(\psi, \phi) \\
&= \sum_{m'_1, m_1} \rho_{m'_1, m_1} \sum_{m'_2, m_2} \rho_{m'_2, m_2}^* \sum_{N_3} B(N_3, m'_1, m_1, m'_2, m_2) Y_{N_3, -\tilde{m}}(\psi, \phi) \\
&= \sum_{m'_1, m_1} \rho_{m_1, m'_1}^* \sum_{m'_2, m_2} \rho_{m_2, m'_2} \\
&\quad \times \sum_{N_3} (-)^{\tilde{m}} B^*(N_3, m_1, m'_1, m_1, m'_2) (-)^{\tilde{m}} Y_{N_3, \tilde{m}}^*(\psi, \phi) \\
&= E^*(N_3). \tag{A4}
\end{aligned}$$

This indicates that the E -coefficients must be real. Of course, this is what we expect since the experimental Doppler cross section in Eq. (31) must give a real number.

B Fundamental B coefficients

The symmetry relations Eq. (A2) and (A3) can be used to reduce computational effort when calculating the complete set of B coefficients:

$$I : B(N_3, m_1, m'_1, m_2, m'_2) = (-)^{\tilde{m}} B(N_3, m'_1, m_1, m'_2, m_2),$$



Table B1: Classification of the different regions of matrix M_1 of the scattering tensor B . The classes A, B, C, and D require a full calculation of the B -coefficients. The classes A'''' , B' , C' contain elements that can be derived from the unprimed regions by applying the symmetry relations indicated.

region $M_1^a)$	#	m_1	m'_1	symmetry
A	j_1^2	$1, \dots, j_1$	$-m_1 + 1, \dots, m_1 - 1$	
A'		$-m'_1 + 1, \dots, m'_1 - 1$	$1, \dots, j_1$	I
A''		$-j_1, \dots, -1$	$m_1 + 1, \dots, -m_1 - 1$	II
A'''		$m'_1 + 1, \dots, -m'_1 - 1$	$-j_1, \dots, -1$	III
B	j_1	$1, \dots, j_1$	m_1	
B'		$-j_1, \dots, -1$	m_1	II
C	j_1	$1, \dots, j_1$	$-m_1$	
C'		$-m_1$	$1, \dots, j_1$	I
D	1	0	0	

a) see figure B1

$$\begin{aligned} \text{II} &: B(N_3, m_1, m'_1, m_2, m'_2) = B(N_3, -m_1, -m'_1, -m_2, -m'_2), \\ \text{I} + \text{II} = \text{III} &: B(N_3, m_1, m'_1, m_2, m'_2) = (-)^{\tilde{m}} B(N_3, -m'_1, -m_1, -m'_2, -m_2). \end{aligned}$$

The tensor $B(N_3, m_1, m'_1, m_2, m'_2)$ can be regarded as a $(2j_1 + 1) \times (2j_1 + 1)$ matrix M_1 with inside each element a $(2j_2 + 1) \times (2j_2 + 1)$ matrix M_2 . Using symmetry relations I and II the matrix M_1 can be divided into several regions which are depicted in Fig. B1. The regions indicated with a prime can be obtained from the unprimed regions using the symmetry relations in Table B1.

Region A is not invariant for either symmetry operations I and II. Therefore, for each combination (m_1, m'_1) in region A we have to calculate the B -coefficients for all combinations (m_2, m'_2) of M_2 , as is shown in Fig. B2. This results in a total number of

$$\#\mathcal{A} = \#A \times \#M_2 = j_1^2 (2j_2 + 1)^2, \quad (\text{B5})$$

where we use $\#$ -symbol to indicate the number of elements in a particular set and the calligraphic characters to indicate the total number of B -coefficients. Region B is invariant for symmetry relation I. This reduces the number of fundamental B -coefficients in the M_2 matrix, as is shown in Fig. B3 where the α region is imaged onto the α' region with symmetry relation I. The remaining number of fundamental B -coefficients is equal to

$$\#\mathcal{B} = \#B \times (\#\alpha + \#\beta) = j_1 \left(\sum_{i=1}^{2j_2} i + (2j_2 + 1) \right) = j_1 (2j_2^2 + 3j_2 + 1). \quad (\text{B6})$$

Region C is invariant for symmetry relation III. This reduces the number of fundamental B -coefficients in the M_2 matrix, as can be seen in Fig. B4 where the α region is imaged

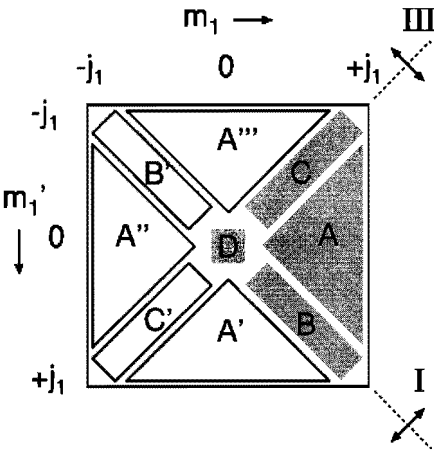


Figure B1: Matrix M_1 is divided into 4 regions using symmetry relations I and III

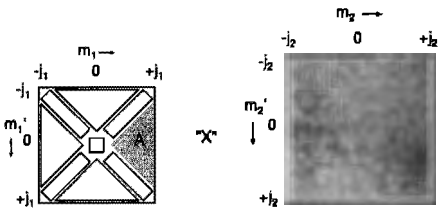


Figure B2: Schematic view of the number of elements in region A

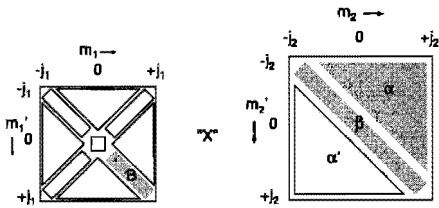


Figure B3: Schematic view of the number of elements in region B



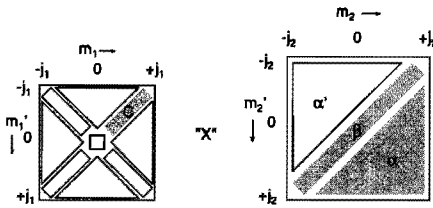


Figure B4: Schematic view of the number of elements into region C

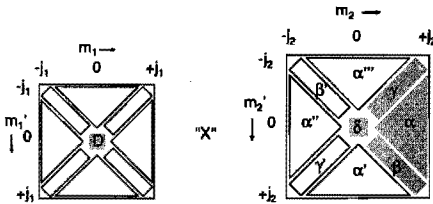


Figure B5: Schematic view of the number of elements into region D

onto the α' region with symmetry relation III. The resulting number of B -coefficients is equal to

$$\#C = \#C \times (\#\alpha + \#\beta) = \#B = j_1 (2j_2^2 + 3j_2 + 1). \tag{B7}$$

Since region D is invariant for both symmetry relations I and III, the number of fundamental B -coefficients is reduced. The total number of basic B -coefficients is equal to

$$\#D = (\#\alpha + \#\beta + \#\gamma + \#\delta) = (j_2^2 + j_2 + j_2 + 1) = (j_2 + 1)^2. \tag{B8}$$

Combining the 4 regions in matrix M_1 with the regions in matrix M_2 gives the total number of fundamental B -coefficients, *i.e.* a minimum set of coefficients which is necessary to describe the collision process completely.

From Table B2 it is clear that the total number of fundamental B -coefficients, that needs to be calculated for a certain choice of j_1 and j_2 , is given by

$$\#A + \#B + \#C + \#D = (2j_1j_2 + j_1 + j_2 + 1)^2. \tag{B9}$$

Notice the symmetric role of j_1 and j_2 in this expression: it doesn't matter which quantum number is larger. The ratio of the fundamental B -coefficients and the total number of B -coefficients is calculated in Table B3 for different combinations of j_1 and

Table B2: Number of contributions of the different regions to the total number of fundamental B -coefficients. The regions A-D are depicted in Figs. B2-B5.

region M_1	region M_2	#
A	complete	$j_1^2(2j_2 + 1)^2$
B	$\alpha + \beta$	$j_1(2j_2^2 + 3j_2 + 1)$
C	$\alpha + \beta$	$j_1(2j_2^2 + 3j_2 + 1)$
D	$\alpha + \beta + \gamma + \delta$	$(j_2 + 1)^2$
$\#A + \#B + \#C + \#D$		$(2j_1j_2 + j_1 + j_2 + 1)^2$

Table B3: Ratio of the number of fundamental B -coefficients and the total number of B -tensor elements as a function of j_1 and j_2 .

j_1	j_2	tensor size $(2j_2 + 1)^2(2j_2 + 1)^2$	gain ratio
0	0	1	1.00
0	1	9	0.45
1	1	81	0.31
1	2	225	0.28
2	2	625	0.27
2	3	1225	0.26
3	3	2401	0.26
$j_1 \gg 1$	$j_2 \gg 1$		0.25

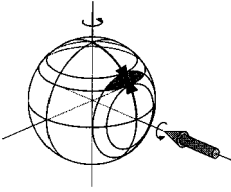
j_2 . From this table it can be seen that for the combinations $(j_1, j_2) = (0, 1)$ and $(1, 0)$, more than a factor of two in computational time can be gained. In the limit for large values of j_1, j_2 the gain is a factor four. Numerical checks indicate that the factors given in Table B3 are a good indication for the decrease in computational effort: the overhead for copying the non-fundamental B -coefficients from the fundamental ones is very small.

References

- [1] M. Manders, W. van Hoek, E. Vredenbregt, G. Sandker, H. Beijerinck, and B. Verhaar, *Phys. Rev. A* **39**, 4467 (1989).
- [2] W. Boom, R. van Galen, B. Klaver, S. Op de Beek, J. Heier, H. Beijerinck, and B. Verhaar, *Phys. Rev. A* **51**, 3837 (1995).
- [3] S. Op de Beek, J. Driessen, K. Robben, H. Beijerinck, and B. Verhaar, chapter 3 of this thesis, to be published.
- [4] D. Hennecart and F. Masnou-Seeuws, *J. Phys. B* **18**, 657 (1985).
- [5] A. Messiah, *Quantum Mechanics* (North-Holland, Amsterdam, 1961), Vol. II.
- [6] J. Driessen and S. Leone, *J. Chem. Phys.* **96**, 6136 (1992).
- [7] K. Blum, *Density matrix and applications* (Plenum, New York, 1981).
- [8] C. Smith, J. Driessen, L. Eno, and S. Leone, *J. Chem. Phys.* **96**, 8212 (1992).
- [9] M. Alexander, P. Dagdigian, and A. DePristo, *J. Chem. Phys.* **66**, 59 (1977).
- [10] R. Zare, *Angular Momentum* (John Wileys & Sons, New York, 1987).
- [11] K. Robben, Master's thesis, Eindhoven University of Technology, The Netherlands, 1996, report, unpublished.







3

Four-Vector correlation experiment on $\text{Ne}(3p) + \text{He}$ collisions: measurements on intramultiplet mixing

S.S. Op de Beek, J.P.J. Driessen, K.H.J.M. Robben,
H.C.W. Beijerinck, and B.J. Verhaar

Intramultiplet mixing collisions have been investigated using polarized $\text{Ne}(3p)$ atoms with a well-defined initial relative velocity, *i.e.*, two initial state vectors. By analyzing the final-state center-of-mass velocity with a (Doppler detuned) probe laser with a well defined polarization and detecting the laser-induced fluorescence we measure the differential cross section and the polarization of the final state, *i.e.*, two final-state vectors. Measurements have been done at a collision energy $E = 70$ meV, for both the α_7 and α_9 (Paschen numbering) initial states. For the elastic $\alpha_7 \rightarrow \alpha_7$ collisions the experimental results are strongly hindered by the undesired response on elastic scattering of the metastable $\text{Ne}(3s, {}^3P_0)$ state. Inelastic collisions have been investigated for the α_9 state, that forms a closed level system with the metastable $\text{Ne}(3s, {}^3P_2)$ state. For the $\alpha_9 \rightarrow \alpha_8$ transition experimental results are presented for both parallel and perpendicular orientations of the polarizations of the pump and probe laser, respectively, as well as for circularly polarized (σ^+ , σ^+) and (σ^+ , σ^-) configurations. The experiments are compared to a full quantum mechanical coupled channels calculation of the scattering process, using the model potentials of Hennecart and Masnou-Seeuws as input. The output of this calculation is combined with a density matrix description of the initial and final-state polarization. Both shape of the differential cross sections and their relative scaling for different laser polarization configurations agree well with experiment. This gives a strong support for the quality of the model potentials used.



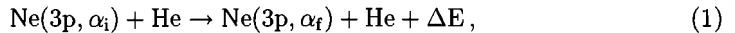
1 Introduction

The study of alignment and orientation in atomic collisions has yielded an enormous wealth of detailed information on the mechanisms and dynamics of collisional excitation and energy transfer. Complete information requires additional detection of the polarization of the final state after the collision. In principle both atomic *alignment* (i.e. symmetric population of magnetic sublevels) and *orientation* (i.e. asymmetric population of magnetic substates) can be determined.¹⁻¹⁰ In favorable cases a complete set of collision amplitudes for the coherently excited atomic states, including their relative phases, can be derived.⁵ Such a study brings experimental results much closer to a theoretical study, which may reveal important features of the potential curves.¹¹⁻¹⁸

Generally, experiments with a number n of controllable vector quantities such as relative velocity and alignment or orientation of atoms are called n -vector correlation measurements.² Polarized atom collision experiments where the initial relative velocity and initial alignment/orientation are controlled are typical examples of two-vector experiments.^{19,20} Combining these two-vector experiments with final-state analysis with respect to the alignment and/or final velocity results in three-vector⁴⁻⁶ and four-vector²¹ correlation experiments.

Many three- and four-vector correlation experiments have been performed for systems with an atom excited directly from the ground state, such as Na, Ba and Ca, colliding with rare gases.^{4,5} Because of the large experimental signals it is possible to resolve the final states with respect to final velocity or final orientation/alignment. A quantum mechanical calculation is hard to perform for these systems since accurate potential information is very scarce.

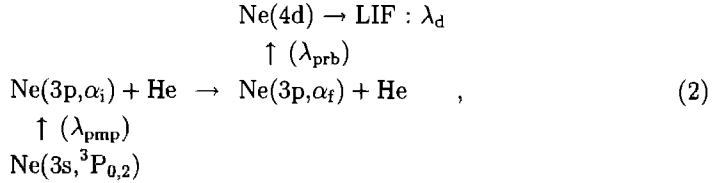
The two-vector correlation experiment of the intramultiplet mixing process



has been studied in detail in the thermal¹⁹ and superthermal²⁰ energy range. The short-lived initial $\text{Ne}(3p, \alpha_i)$ states ($\tau = 20\text{ns}$) are produced by laser excitation from one of the metastable $\text{Ne}(3s)$ states, 3P_0 or 3P_2 , which account for an excited fraction $\eta \approx 10^{-5}$ of the total atomic beam flux. Therefore, the densities of the initial $\text{Ne}(3p)$ states are much smaller compared to alkali atom densities available for excitation. By measuring the fluorescence intensity of a decay transition for both the initial and final state, polarized-atom cross sections $Q_{i \rightarrow f}^{M_i}$ can be determined.^{19,20} Here M_i is the magnetic quantum number of the electronic angular momentum J of the initial state with respect to the initial relative velocity v_i . Both a semiclassical and fully quantum mechanical analysis result in theoretical cross sections which are in good agreement with the experimental data.^{19,20} Although the experimental signals are rather small, the advantage of the system in Eq. (1) lies in the available accurate potential information,²²⁻²⁴ in contrast to the excited alkali atom-ground state noble gas systems.

In this paper we focus on a new pump-probe experiment performed on the collision

process of Eq. (1). The following pump-probe scheme is used:



where the Ne(3p) fine structure levels are denoted by the Paschen numbering ($i, f \in 1, \dots, 10$). The final state Ne(3p, α_f) is probed with a laser-induced fluorescence (LIF) technique which is combined with a Doppler probing scheme to resolve the final-state velocity. This pump-probe scheme has been chosen such that the decay fluorescence of the Ne(4d) state ($\lambda_d \approx 530$ nm) is isolated from decay lines from other multiplets ($\lambda = 580\text{--}670$ nm). Moreover, the decay lines of the Ne(4d) state have large branching ratios ($> 60\%$) which make them suitable for the LIF-technique.

In this paper we focus on two types of scattering processes: *i*) elastic collisions for $\alpha_7 \rightarrow \alpha_7$ and *ii*) inelastic collisions for $\alpha_9 \rightarrow \alpha_8$. In principle, four vector parameters can be examined in the experiment; two velocity vectors (1) \mathbf{v}_i the initial relative velocity and (2) \mathbf{v}_f the final relative velocity of the colliding particles and two alignment/orientation vectors (3) \mathbf{E}_{pmp} the polarization vector of the pump laser used to prepare the initial state and (4) \mathbf{E}_{prb} the polarization vector of probe laser used in the LIF detection scheme. In our crossed beam experiment the initial relative velocity \mathbf{v}_i is well-defined. The final velocity is detected through a Doppler detection scheme which is combined with the LIF scheme. Using polarization rotators the polarizations of both lasers can be controlled. The number of controllable parameters in this four-vector experiment can be very large. To limit the number of measurements we use fixed laser beam directions in our setup: the pump and probe laser beams are counter propagating, perpendicular to the initial relative velocity \mathbf{v}_i .

In this paper we present the first experimental data on the final-state analysis of the intramultiplet mixing process in Eq. (1). On the basis of two processes, $\alpha_7 \rightarrow \alpha_7$ and $\alpha_9 \rightarrow \alpha_8$, we investigate the feasibility of a final state analysis for short-lived Ne(3p) states. Section 2 will deal with the final-state analysis where the LIF detection scheme is combined with the Doppler probing technique. The experimental setup is described in Section 3. In the same section the implementation of the pump and probe lasers is discussed. The Doppler probing technique is calibrated by applying it to elastic scattering of metastable Ne(3s) states. The results of this calibration are presented in Section 4. In Sections 5 and 6 the four-vector experiments for elastic and inelastic scattering are discussed, respectively. In Section 7 the experimental data are compared with theoretical simulations based on a fully quantum mechanical coupled channels calculation. Finally, in Section 8 concluding remarks are given.

2 Final-state analysis

2.1 LIF technique

Information about the final-state orientation/alignment is acquired using a LIF technique, which has been described in more detail by Smith *et al.*⁵ for the Ca-He system. In our case, the second laser beam probes the final Ne(3p, α_f) state by exciting it to the Ne(4d)-level. From the decay fluorescence of the Ne(4d) state information about the magnetic sublevel distribution for the final Ne(3p, α_f) state is obtained. The pump/probe scheme is depicted in Fig. 1. In this setup the initial Ne(3p, α_i) state is

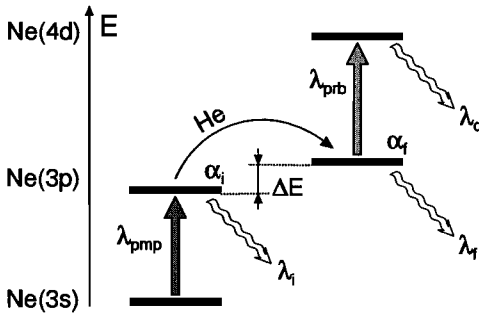


Figure 1: Scheme of a general pump-probe experiment. The pump laser excites the Ne(3s) state to the Ne(3p, α_i) state. The collision induced final state Ne(3p, α_f) is probed by exciting it to a state in the Ne(4d)-multiplet with a probe laser and measuring the fluorescence at λ_d .

selected by the pump laser (λ_{pmp}); the wavelength of the probe laser (λ_{prb}) determines which final state is analyzed. We label the Ne(3p) state with $|p\rangle$ and the state coupled by the probe laser by $|d\rangle$.

The final state has a total angular momentum quantum number J in the range $0 \leq J \leq 3$ for which different probing schemes are possible. In Fig. 2 we show the possible probing schemes for a $J = 1$ final state with a linearly or circularly polarized probe laser. By saturating the probe-transition, each of the probed magnetic sublevels of the final state is detected with equal probability. Obviously, the transition $J \rightarrow J + 1$ probes all magnetic sublevels and cannot provide alignment/orientation information of the final state. However, using the $J \rightarrow J$ and $J \rightarrow J - 1$ transitions, different subsets of magnetic sublevels are excited and combinations of these two probing schemes enable us to extract more information than either probing scheme separately. Using circularly polarized light, the asymmetry in the probed magnetic sublevel distribution gives information on the orientation of the final state.

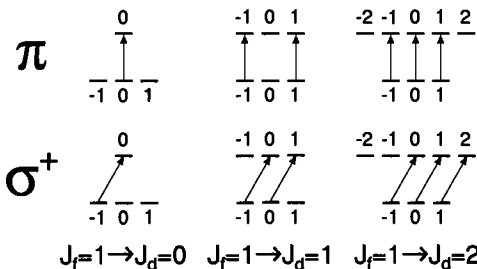


Figure 2: Probe schemes for a $J_f = 1$ final state for linearly polarized (π) and circularly polarized (σ) light, respectively. Only the schemes with $J_d \leq J_f$ give information on alignment and/or orientation.

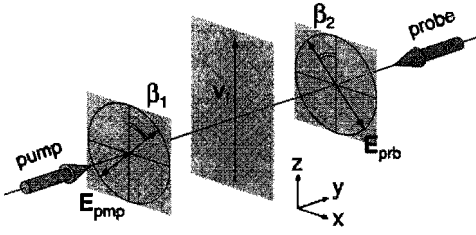


Figure 3: The configuration of the linear laser polarizations. The polarization vectors \mathbf{E}_{pmp} and \mathbf{E}_{prb} of pump and probe lasers, respectively, are rotated over angles β_1 and β_2 in a plane perpendicular to the propagation direction of the lasers.

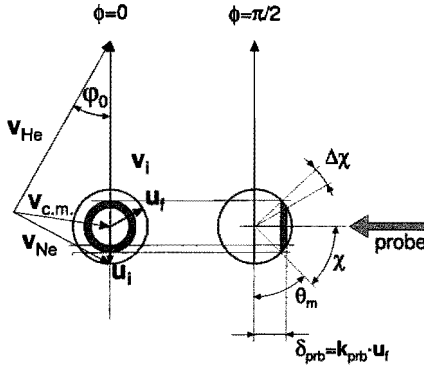


Figure 4: Newton diagram for an elastic collision. The initial Ne velocity in the center of mass coordinate system is indicated by \mathbf{u}_i . The shaded ring represents the velocity class which is resonant with a laser with detuning δ_{prb} . The left-hand side shows a view perpendicular to the collision plane ($\phi = 0$), the right-hand side parallel to the collision plane ($\phi = \pi/2$).

In the configuration described in this paper the pump and probe laser beams are counter propagating, perpendicular to the initial relative velocity \mathbf{v}_i as shown in Fig. 3. In case of linearly polarized laser beams the polarization angles β_1 and β_2 , defined with respect to the initial relative velocity \mathbf{v}_i , can be varied using $\lambda/2$ -plates. The linearly polarized configurations (β_1, β_2) that we investigate consist of a set of parallel polarizations: $(0, 0)$ and $(\pi/2, \pi/2)$ and a set of perpendicular polarizations: $(0, \pi/2)$ and $(\pi/2, 0)$. In case of circular polarization two configurations are possible: (σ^+, σ^+) , (σ^+, σ^-) . Combinations of linear and circular polarizations have not yet been investigated.

2.2 Doppler probing

The LIF probing scheme can be combined with a Doppler technique to resolve the velocity component of the final state in the probe-laser beam direction. The velocities of the Ne and He atoms are shown in a Newton diagram in Fig. 4 together with the initial relative velocity \mathbf{v}_i . The final velocity \mathbf{u}_f of the Ne($3p, \alpha_f$) state in the center-of-mass (c.m.) system has an arbitrary direction resulting in the so-called (in)elastic scattering sphere centered around the c.m. velocity $\mathbf{v}_{\text{c.m.}}$. The radius of the scattering sphere is given by

$$\mathbf{u}_f = \frac{m_{\text{He}}}{m_{\text{Ne}} + m_{\text{He}}} \mathbf{v}_f, \quad (3)$$

with \mathbf{v}_f being the final relative velocity. Depending on the sign of ΔE in Eq. (1) the radius is smaller, equal or larger than the initial relative velocity \mathbf{u}_i . In Fig. 4 the situation for an elastic collision is shown. The particles which are probed by the δ_{prb} -

Table 1: Probe parameters for the $\alpha_7 \rightarrow \alpha_7$ elastic and $\alpha_9 \rightarrow \alpha_8$ inelastic transitions in the Ne(3p) multiplet.

	$\alpha_7 \rightarrow \alpha_7$	$\alpha_9 \rightarrow \alpha_8$
ΔE (meV)	0	21
v_f (m/s)	2010	1680
u_i (m/s)	335	335
u_f (m/s)	335	280
λ_{prb} (nm)	593	583
$\Delta\omega_{\text{max}}$ (2π MHz)	564	484

detuned laser beam have a well-defined velocity component with respect to the y -axis (laser beam axis). This results in the so-called ‘Doppler cone’ with a top angle χ which depends on the laser detuning δ_{prb} through the Doppler detuning

$$\begin{aligned}\delta_{\text{prb}} &= \mathbf{k}_{\text{prb}} \cdot (\mathbf{v}_{\text{c.m.}} + \mathbf{u}_f) \\ &= \Delta\omega_{\text{c.m.}} + k_{\text{prb}} u_f \cos(\chi),\end{aligned}\quad (4)$$

with \mathbf{k}_{prb} being the wave vector of the probe laser beam. Here we have taken into account the transformation from the c.m. frame to the laboratory frame. The center-of-mass contribution $\Delta\omega_{\text{c.m.}}$ is equal to zero because the laser beam is aligned perpendicular to the two atomic beams. The detuning δ_{prb} and the angle χ are related by

$$\delta_{\text{prb}} = k_{\text{prb}} u_f \cos(\chi) = \Delta\omega_{\text{max}} \cos(\chi). \quad (5)$$

The linewidth γ_{prb} of the probe laser and the natural linewidth Γ_{prb} of the probing transition result in a finite angular range $(\chi, \chi + \Delta\chi)$ together with the corresponding resolution of the velocity component $(\mathbf{u}_f)_y$. For a typical thermal energy $E = 70\text{meV}$ elastic collision, the relative velocity is 1800 m/s. The final velocity u_f of the Ne(3p) state is 340 m/s. This translates in a detuning range $2\Delta\omega_{\text{max}} \approx 1.1(2\pi)$ GHz in case of the typical 593nm probe laser light. If a narrow-bandwidth dye laser is used, the natural linewidth $\Gamma \approx 10(2\pi)$ MHz determines the maximum obtainable resolution of approximately $0.01 \Delta\omega_{\text{max}}$ which corresponds to a velocity resolution $\Delta v_y \approx 7 \text{ms}^{-1}$. For high laser intensities power-broadening may reduce this resolution. For the transitions we study in this paper, the probe parameters are listed in Table 1.

Because the laser beam direction does not coincide with the relative velocity vector, the top angle χ does not correlate with a unique scattering angle θ , defined with respect to \mathbf{v}_i (*i.e.* the z -axis). These angles are depicted in Fig. 5. For top angles $\chi > 0$ the resonant particles correspond to scattering angles $\theta_m < \theta < \pi - \theta_m$, with $\theta_m = \pi/2 - \chi$. The differential cross section in the direction θ cannot be directly derived from the signals measured as a function of χ . Only for $\chi = 0$ (probing the ‘pole-cap’) the measured signal directly translates into $\theta = \pi/2$, albeit with a rather poor resolution. For other angles χ the following relation between scattering angle θ and χ holds:

$$\theta(\chi, \zeta) = \arccos(\sin \chi \cos \zeta), \quad (6)$$

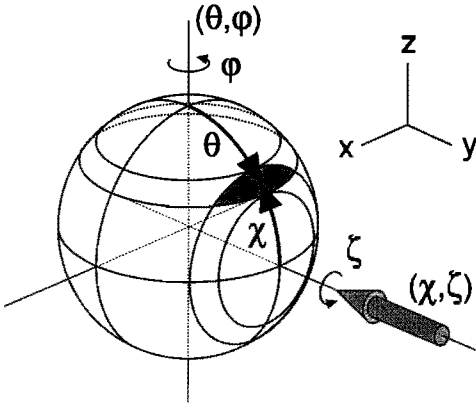


Figure 5: 3D-view of scattering sphere with the scattering cone between $(\theta, \theta + \Delta\theta)$ and the Doppler cone between $(\chi, \chi + \Delta\chi)$. The top angles (θ, ϕ) and (χ, ζ) are defined with respect to the z -axis and the y -axis, respectively.

Table 2: Performance of the ring dye-laser system compared to the diode-laser system.

system	dye laser	diode laser
λ -range	550-660 nm	$\approx 630, \approx 650, \approx 670, 750$ -850 nm
$\Delta\omega_{lw}$	< 10 MHz	20-100 MHz ^{a)}
Power	> 200 mW	< 10 mW
frequency drift	< 10 MHz/min ^{b)}	< 100 Mhz/min ^{c)}

a) No strong optical feedback

b) Locked to internal frequency reference

c) Not locked to external frequency reference

where ζ denotes the azimuthal angle about the laser probe axis (y -axis).

2.3 Pump/probe laser considerations

Pump laser

Two different laser systems are available for our experiment, *i*) a dye laser using Rhodamine/DCM dyes and *ii*) a diode laser with weak optical feedback.

The performance of these two systems is given in Table 2. The pump laser excites either the 3P_0 or 3P_2 state of the Ne(3s) configuration to one of the fine structure states of the Ne(3p)-multiplet. The pump laser is frequency stabilized by optimizing the absorption in a Ne discharge. For a dye laser, extra attention has to be paid to the alignment of the laser beam due to its narrow linewidth. This is extensively discussed in Ref. [19].

The transition wavelengths vary in the range $588 \text{ nm} < \lambda < 744 \text{ nm}$. For the initial states we will concentrate on the wavelengths listed in Table 3. These fine structure states can be excited with a dye-laser operating on Rhodamine 6G or DCM. Two diffe-



Table 3: Wavelengths in nm for the pump transitions of the metastable Ne(3s) states to a Ne(3p, α_k) state.

Ne(3s)	Ne(3p, α_4)	Ne(3p, α_7)	Ne(3p, α_8)	Ne(3p, α_9)
3P_0		653.288		
3P_2	594.483	621.728	633.443	640.225

Table 4: Wavelengths for the probe transitions of Ne(3p, α_f) to the Ne(4d) states in the notation of jl coupling. The corresponding branching ratios A_{ki}/A_k are indicated as well.

Ne(4d)	Ne(3p, α_7)		Ne(3p, α_8)		Ne(3p, α_{10})	
	λ (nm)	A_{ki}/A_k (%)	λ (nm)	A_{ki}/A_k (%)	λ (nm)	A_{ki}/A_k (%)
$4d(3/2)_2$	591.903	3.3	581.662	1.7	533.078	44.3
$4d(1/2)_1$	593.175	0.0	582.891	2.6	534.109	63.7
$4d(1/2)_0$	593.446	9.3			534.328	74.4

rent diode laser systems are available for Ne excitation: $\lambda_{\text{pmp}} = 653$ nm for ($^3P_0 \rightarrow \alpha_7$) and $\lambda_{\text{pmp}} = 633$ nm for ($^3P_2 \rightarrow \alpha_8$). For the transitions in this paper we use a diode laser for preparing α_7 states and we use a dye laser for exciting the Ne(3s, 3P_2) states to one of the α_4 , α_8 , or α_9 states.

Probe laser

To select a probe transition we must meet the following demands: *i*) the wavelength λ_{prb} must be attainable by our lasers, *ii*) we have to be able to single out the LIF wavelength λ_d (Fig. 1) with narrow-band interference filters in order to suppress competing fluorescence signals produced in the Ne-source or in the collision process, *iii*) the lifetime of the upper state |d) must be comparable to that of the |p) state to guarantee sufficient fluorescence signal when saturating the |p) \rightarrow |d) transition, and finally *iv*) the branching ratio must be large for the studied decay transition (λ_d) to produce sufficient signal.

Based on these criteria we have selected the Ne(3p) \rightarrow Ne(4d) transition for probing the final Ne(3p) states. Due to the large energy gap between the α_9 and α_{10} states the decay lines of the Ne(4d) \rightarrow α_{10} transition are located around 534 nm and can be separated out easily from the other decay lines. This makes them suitable for detection without being disturbed by laser light or decay lines from the Ne(3p)-multiplet. In this paper we limit ourselves to the probing of the final states Ne(3p, α_7) and Ne(3p, α_8). The transition lines from the α_7 and α_8 states to the Ne(4d) multiplet are listed in Table 4, together with their branching ratios A_{ki}/A_k . The large branching ratios of the subsequent transitions to the α_{10} state makes them suitable for the LIF technique. All

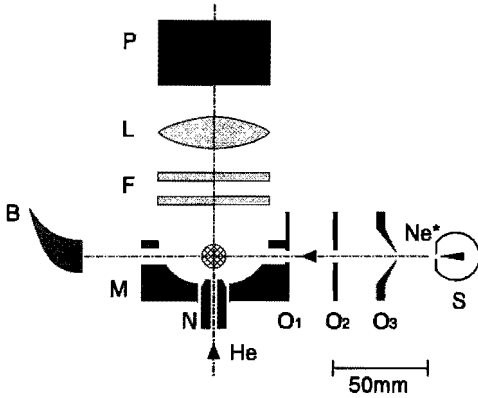


Figure 6: Schematic view of the crossed beam apparatus. (S) Ne(3s) metastable atom source; (O_1) beam-defining aperture (diameter=1 mm); (O_2) extra aperture (diameter=1 mm); (O_3) skimmer (diameter=0.5 mm); (M) parabolic mirror; (B) beam dump; (N) nozzle; (F) interference filters; (L) collimating lens; (P) photomultiplier.

the probe line wavelengths are easily attainable with a dye laser. The linewidth of the probe transition is approximately $20(2\pi)$ MHz, determined by the lifetime of both the $|p\rangle$ and $|d\rangle$ state.

3 Experimental setup

3.1 Crossed beam apparatus

To analyze the final states of intramultiplet mixing collision processes we use the experimental setup used previously for total cross section measurements. In this paper we briefly review the apparatus, for details the reader is referred to Refs. [19, 20]. In Fig. 6 a schematic view of the crossed beam apparatus is given. The scattering center is formed by the intersection of the Ne beam, the He beam and the pump-laser beam. The metastable Ne(3s) atoms are produced in a thermal discharge source.²⁵ The He beam is obtained through a skimmerless supersonic expansion. Fluorescence of the initial and final Ne(3p) states is efficiently collected by a parabolic mirror and focussed onto a photomultiplier. Wavelength selection is realized using narrow-band interference filters. Absolute values of the cross sections can be determined because the relative detection efficiencies for the initial and final state fluorescence are known. Due to the small dimensions of this atypical crossed beam apparatus with its efficient photon collection we can achieve typical countrates of $1 \text{ kcps}/\text{\AA}^2$ for the two-vector correlation experiment of the intramultiplet mixing processes of Eq. (1). Typical performance conditions of the apparatus are given in Table 5.

The velocity distribution of Ne-atoms produced by the thermal discharge source is determined through time-of-flight (TOF) measurements. In the compact crossed beam setup we use a laser chopper. With a flight path of only 100 mm the TOF experiment requires small time channels ($\tau = 20 \mu\text{s}$). The result of a typical measurement is given in Fig. 7. From the analysis of these data we find an average velocity $\langle v_{\text{Ne}} \rangle = 960 \pm 30 \text{ m/s}$ and a characteristic velocity spread $\alpha = 380 \text{ m/s}$. Combined with the He beam velocity distribution we find for the average relative velocity $\langle v_i \rangle \approx 1800 \text{ m/s}$ and the corresponding average collision energy is estimated at $\langle E \rangle = 70 \text{ meV}$.

Table 5: Typical performance conditions of the experimental setup.

name	quantity	typical value	units
atomic beams			
Ne(3s) beam intensity	$I_{\text{Ne}(3s)}$	9×10^{12}	$(\text{s}^{-1}\text{sr}^{-1})$
source - scattering center distance	L	100	(mm)
solid angle acceptance of Ne beam	Ω_{scat}	4×10^{-4}	(sr)
Ne flow velocity	v_{Ne}	960	(m/s)
speed ratio	$S = v/\alpha$	2.5	
He velocity	v_{He}	1800	(m/s)
He density	n_{He}	1×10^{20}	(m^{-3})
transmission factor	T_i	$1/e$	
initial relative velocity	v_i	2000	(m/s)
average collision energy	E	70	(meV)
detection for Ne(4d) line			
PM quantum efficiency	η_{qe}	0.15	
collection efficiency of optical system	η_{os}	0.40	
filter transmission	T_{filt}	0.6	
branching ratio	A_{ki}/A_k	0.6	

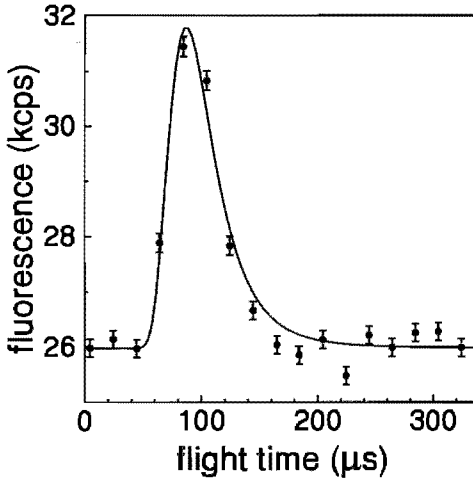


Figure 7: Typical time-of-flight measurement for Ne(3s) atoms performed with a flight path $L = 100\text{mm}$. From this we derive a flow velocity $\langle v \rangle = 956\text{ m/s}$ and a characteristic velocity spread $\alpha = 384\text{ m/s}$ for the velocity distribution.

The Ne(3s) beam, travelling in the x -direction, is attenuated by elastic scattering with He atoms. The probability for elastic scattering in travel distance $(x, x + dx)$ is given by the product $n_2(\mathbf{r}) dx Q^{\text{el}}$, with n_{He} the local He beam density and Q^{el} the effective total cross section for elastic scattering. The total transmission probability for reaching the scattering center is expressed in a factor T_i which is defined by

$$T_i = \int_{-\infty}^0 \frac{v_i(x)}{v_{\text{Ne}}} n_{\text{He}}(x) Q^{\text{el}} dx. \quad (7)$$

To obtain optimal collision-induced fluorescence²⁶ this transition probability is taken close to $T_i \approx 1/e$ by regulating the He beam density n_{He} . The interaction length of the Ne(3s) states with the He beam upstream of the pump laser beam is denoted by l_s which is typically $l_s \approx 2$ mm in our apparatus. The flux of unscattered metastable Ne(3s) atoms arriving at the scattering center is denoted by \dot{N}_s . The value of this quantity can be estimated using Table 5. The flux of Ne(3s) states is given by $\dot{N}_s = I_{\text{Ne(3s)}} \Omega_{\text{scat}} T_i$, from which we find $\dot{N}_s \approx 1.1 \times 10^9 \text{ s}^{-1}$.

The Ne(3s) states are excited to the initial Ne(3p) state with an efficiency f_{pmp} . Taking into account the natural abundance of the ²⁰Ne isotope (90%) together with the statistical distribution over the magnetic sublevels results in efficiencies and $f_{\text{pmp}} = 0.15$ and $f_{\text{pmp}} = 0.75$ for the ³P₀ or ³P₂ states, respectively. Hence, the flux of initial Ne(3p) states is given by

$$\dot{N}_p = f_{\text{pmp}} \dot{N}_s. \quad (8)$$

Because of the short lifetime $\tau = 20$ ns of the Ne(3p) states, the lifepath is only $l_p = 20$ μm which results in a much smaller collision probability than for the Ne(3s) states.

The maximum resolution $\Delta\omega/\delta\omega_{\text{max}} \approx 0.01$ in the final velocity component decreases the performance of $1 \text{ kcps}/\text{\AA}^2$ for the total cross section for intramultiplet mixing to approximately $10 \text{ cps}/\text{\AA}^2$ for the velocity resolved differential cross section. Therefore, an adequate suppression of background signal caused by scattered laser photons and photons produced in the Ne(3s) source is necessary. Because of the large separation of the selected fluorescence line ($\lambda_d \approx 530$ nm) from other decay lines we planned to use a 10 nm broad transmission filter (see Table 4). The detection efficiency for collecting light from this decay line is given by $\eta_{\text{det}} = \eta_{\text{eq}} \eta_{\text{os}} T_{\text{filt}} A_{ki}/A_k$ and can be determined using Table 5 resulting in $\eta_{\text{det}} = 2 \times 10^{-2}$.

The Ne(3s) source causes a huge background signal of 180 kcps in combination with the 10 nm transmission filter, thus far exceeding the expected differential fluorescence signal. Using a beam-defining aperture in front of the parabolic mirror (O_1 in Fig. 6) this background was reduced to 1 kcps. Apparently, light emitted from the source enters the detection system through reflections in the apparatus. This background is further reduced to 200 cps by painting parts in the detection chamber black and by installing an extra aperture with 1 mm diameter between the skimmer and the downstream aperture in front of the parabolic mirror (O_2 in Fig. 6). Because light is also being emitted in the Ne-expansion downstream of the skimmer, this extra aperture prevents these photons to reflect in the parabolic mirror. The remaining background is further reduced to 50 cps using a 1 nm bandwidth transmission filter.

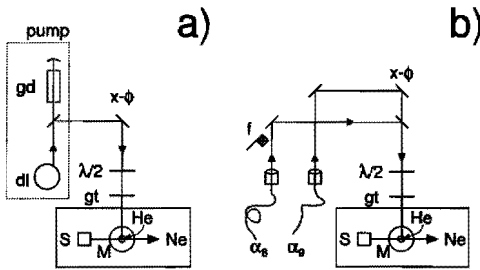


Figure 8: Schematic view of the pump laser setup. For elastic and inelastic collisions we use setup a) or setup b), respectively. (s) Ne metastable source; (dl) diode laser; (gd) gas discharge; ($x-\phi$) computer adjustable mirror; ($\lambda/2$) half-lambda plate (gt) Glan-Taylor polarizing prism; (f) laser flag; (α_8) dye laser tuned at ${}^3P_0 \rightarrow \alpha_8$ -transition; (α_9) dye laser tuned at ${}^3P_0 \rightarrow \alpha_9$ -transition.

3.2 Pump laser

A temperature- and current-stabilized diode laser is used for populating the initial α_7 state. Weak optical feedback is used to enlarge the lasing range such that the desired wavelength can be reached.²⁷ The laser is frequency stabilized by maximizing the laser beam absorption in a Ne rf-discharge using electronic feedback on the laser diode current. The linewidth of the diode laser is measured in a frequency scan where we monitor fluorescence of the Ne(3p) state. Taking into account the geometrical beam divergence and the natural linewidth $\Gamma=8(2\pi)$ MHz we find an effective linewidth of $\gamma_{\text{eff}}=50(2\pi)$ MHz, reflecting the broad linewidth of the laser diode. The experimental setup of the diode laser is shown in Fig. 8(a).

For populating one of the initial α_4 , α_8 , or α_9 states we use a cw dye laser which is stabilized on the absorption in a Ne discharge cell. The laser beam is transported through a single mode optical fiber to preserve the linear polarization. This is shown in Fig. 8(b). The polarization of the pump laser is rotated by a $\lambda/2$ plate. Non-linear components are eliminated by a Glan-Taylor prism.

When we study the inelastic transition $\alpha_9 \rightarrow \alpha_8$, an auxiliary laser beam is used for populating the final α_8 state directly by exciting the 3P_2 states. This facilitates the stabilization of the probe laser frequency to the desired transition line, which will be discussed in the Section 6. This additional laser beam is blocked during the actual collision experiment.

3.3 Probe laser

The probe laser setup is schematically shown in Fig. 9. We use a standing wave cw dye laser locked to the transmission profile of a temperature stabilized Fabry-Pérot etalon. By piezo-electric regulation of this etalon, the dye laser frequency can be tuned over a range of $3(2\pi)$ GHz. Recording the fringes on a $150(2\pi)$ MHz monitoring etalon provides a calibration of the frequency scale. The drift of the laser frequency is less than $1(2\pi)$ MHz per minute, which is small in comparison with the probe transition linewidth of $10(2\pi)$ MHz. For accurate alignment, the laser beam is transported through a single mode optical fiber from the dye laser to the apparatus.

Absorption of the probe laser beam in a Ne discharge is impractical to optimize the

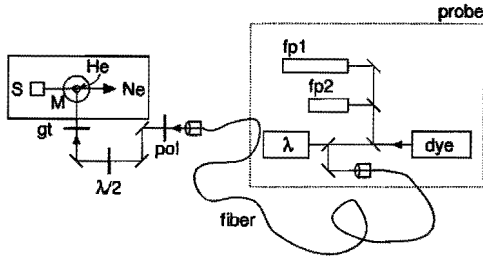


Figure 9: Schematic view of the probe laser setup. (dye) standing wave dye laser; (fp1) monitoring etalon with 150MHz FSR; (fp2) temperature stabilized locking etalon; (λ) wave length meter; ($\lambda/2$) half-lambda plate (gt) Glan-Taylor polarizing prism; (pol) polarizer.

laser frequency of the probe laser due to the small $\text{Ne}(3p)$ population in the discharge. Therefore, we use the $\text{Ne}(3p)$ states produced in the scattering center for finding the probe wavelength. In case of the inelastic collision experiment an auxiliary laser is used for populating the final $\text{Ne}(3p)$ state with subsequent optimization of the probe wavelength. We monitor the fluorescence from the $\text{Ne}(4d)$ state while making a scan of the probe laser frequency reference. Once the probe transition line is found, the laser frequency is locked to the temperature stabilized etalon with a small drift (< 5 MHz/min). Using a piezo-electric detuning of this cavity, we can fix the laser detuning to its desired value δ_{prb} . During a measurement the probe wavelength is optimized periodically (every 10 minutes) to compensate for the frequency drift of the probe laser.

The probe laser power in the collision experiment is approximately 3 mW which is sufficient to saturate the probe-transition. The waist position and size of the probe laser is chosen such that a good overlap with the pump laser is achieved. The waist size of the probe laser is typically 2 mm, whereas the waist size of the pump laser is only 1 mm. The polarization of the probe laser is rotated with a $\lambda/2$ -plate and subsequently cleaned up by a Glan-Taylor prism.

4 Doppler probing of $\text{Ne}(3s, {}^3P_0, {}^3P_2)$ elastic scattering

Applying the Doppler probing technique to the final $|p\rangle$ states is not trivial due to the small final-state populations produced in our collision experiment. A suitable system for testing the Doppler probing technique is elastic scattering of $|s\rangle$ states which are scattered over their full interaction length with the supersonic He expansion. From the transmission probability $T_i \approx 1/e$ in Eq. (7) it follows that approximately 70% of the $|s\rangle$ -particles are scattered by the He atoms before reaching the scattering center. The $|s\rangle$ states are excited to $|p\rangle$ states using a tunable pump laser. The decay fluorescence of the $|p\rangle$ states is measured as a function of the detuning δ_{pmp} of the pump laser. The relation between the detuning δ_{pmp} and the top angle χ of the ‘Doppler’ cone is analogous to Eq. (5).

We use the tunable dye laser (used as probe laser in a pump-probe experiment) to excite the ${}^3P_2 \rightarrow \alpha_4$ transition. The effective linewidth γ_{eff} is mainly determined by the natural linewidth Γ and only to a small extent by the laser linewidth γ_{pmp} and the geometrical divergence of the $\text{Ne}(3s)$ beam. We measure the decay fluorescence of the α_4 state as a function of the detuning δ_{prb} with the He beam switched on and off,



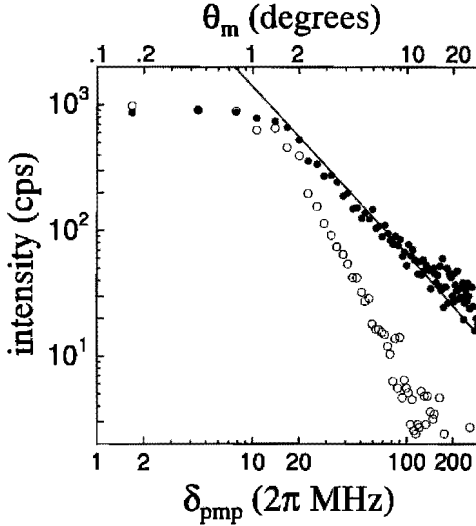


Figure 10: Direct fluorescence for the elastic scattering of $\text{Ne}(3p, {}^3P_2)$ states as a function of the detuning δ_{prb} with the He beam switched on (filled markers) and off (open markers). The fluorescence for the He beam switched off is scaled with the attenuation factor $T_i = 1/e$. The solid line represents the model function of Eq. (11) for classical small angle scattering.

respectively. The result of such a scan is plotted in Fig. 10. With the He beam on, we have an effective transmission (or beam attenuation) of $T_i \approx 30\%$. For comparison, we show the signal with the He beam switched off multiplied by the same attenuation factor T_i . For a detuning $\delta_{\text{prb}} \geq 20(2\pi)$ MHz the small angle scattering of the $\text{Ne}(3s)$ states contributes significantly to the observed signal.

The small angle scattering of $|s\rangle$ states is in good approximation determined by the long-range part of the attractive potential,^{28,29} which is given by

$$V(r) = -C_6/R^6, \quad (9)$$

with R being the internuclear distance. For scattering angles $\theta < \theta_0$, with $\theta_0 = (4\pi/k^2Q)^{1/2}$ a quantum mechanical scaling angle, diffraction phenomena dominate the differential cross section. In our case where $\theta_0 \approx 4$ mrad, this region is not relevant. For $\theta > \theta_0$ small angle scattering is fully described by classical mechanics, *i.e.*, the equivalent of refraction. For a C_6 potential the differential cross section is related to the scattering angle as²⁸

$$\sigma(\theta)/\sigma(0) = 0.285 (\theta/\theta_0)^{-7/3}, \quad (\theta > \theta_0), \quad (10)$$

where $\sigma(0)$ denotes the forward scattering cross section.

The measured signal is proportional to the integral of this differential cross section over the Doppler cone with top angle χ , as indicated in Fig. 5. Using Eqs. (5) and (10) we derive in Appendix A an expression for the detected signal

$$S(\delta_{\text{pmp}}) = C(\gamma_{\text{eff}}, n_{\text{He}}, l_p) \left[\frac{\pi}{2} - \chi(\delta_{\text{pmp}}) \right]^{-4/3}, \quad (11)$$

where the scaling constant C contains several experimental parameters. Note that this approximation is only valid for $(\pi/2 - \chi) < 0.5$ (rad) where it is accurate within 1%.

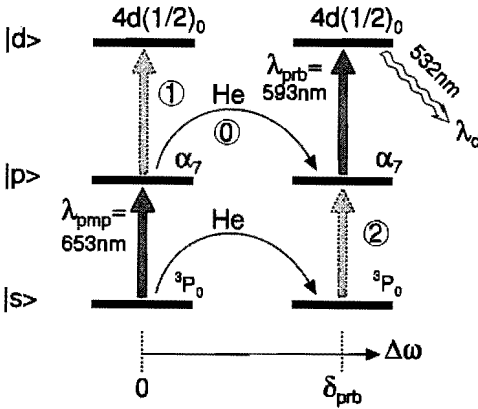


Figure 11: Pump-probe scheme for the elastic $\alpha_7 \rightarrow \alpha_7$ transition. The dashed arrows 1 and 2 indicate competing excitation processes which contribute to the signal.

The top angle χ is written as

$$\chi(\delta_{\text{pmp}}) = \arccos\left(\frac{\delta_{\text{pmp}}}{\Delta\omega_{\text{max}}}\right), \quad |\delta_{\text{pmp}}| < \Delta\omega_{\text{max}}, \quad (12)$$

where we used Eq. (5). In Fig. 10 the experimental data are plotted on a log-log scale together with the model function of Eq. (11). For a detuning corresponding with angles θ_m in the range $0.03 < \theta_m$ (rad) < 0.5 there is very good agreement with the relation of Eq. (11). A background of approximately 30 Hz is subtracted. Obviously, the Doppler technique probes the $\theta^{-7/3}$ -character of the differential cross section. We conclude that the Doppler technique works very well and can be utilized in our proposed pump-probe experiment.

5 Ne($3p, \alpha_7$) elastic scattering

5.1 Measuring scheme

The excitation and detection scheme for $\alpha_7 \rightarrow \alpha_7$ elastic scattering is shown in Fig. 11. We use a $\lambda_{\text{pmp}} = 653$ nm diode laser to excite the 3P_0 states and a dye laser at $\lambda_{\text{prb}} = 593$ nm probes the α_7 through excitation to a $J_d = 0$ state of the Ne($4d$)-multiplet. This $J_s = 0 \rightarrow J_p = 1 \rightarrow J_d = 0$ -scheme facilitates the analysis. The decay line of the Ne($4d$) state to the Ne($3p, \alpha_{10}$) state at $\lambda_d = 534$ nm is detected with an interference filter at 534 nm with a 1 nm band width.

In Fig. 11 three contributions to the detected 534 nm signals are indicated and numbered. The actual collision process that we want to investigate is denoted by the arrow 0. The dashed arrows 1 and 2 show the competing excitation processes representing the *direct* probing of unscattered α_7 states and the 3P_0 states that are scattered before they are excited by the 653 nm pump laser. The suppression of the signal due to these competing processes requires a detailed analysis of these signals. In this analysis we will not take into account the $|M_J|$ -dependency of the scattering process.



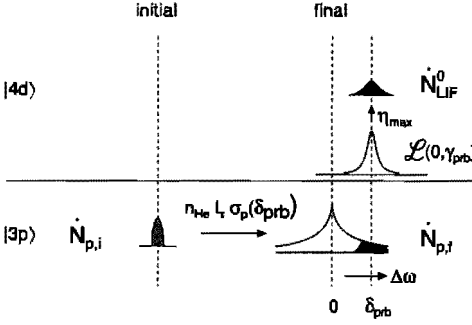


Figure 12: Schematic representation of signals in the elastic scattering probing scheme. The symbols are declared in the text.

We start out by analyzing the desired process, *i.e.*, the probing of elastic scattered $|p\rangle$ states. This process is schematically depicted in Fig. 12. In the scattering center we have flux $\dot{N}_{p,i}$ of $|p\rangle$ states given by Eq. (8). The collision rate $\dot{N}_{p,f}(\delta_{\text{prb}})$ is determined by the effective density-length product

$$\dot{N}_{p,f}(\delta_{\text{prb}}) = n l_{\tau} \sigma_p(\delta_{\text{prb}}) \dot{N}_{p,i}, \quad (13)$$

where $l_{\tau} = v_i \tau$ denotes the ‘life-path’ of the short-lived state and $\sigma_p(\delta_{\text{prb}})$ is the differential cross section for scattering into the Doppler cone about the probe laser beam with top angle $\chi(\delta_{\text{prb}})$, as defined in Eq. (5). These final states are resonant with the probe laser. Therefore, they will contribute to the desired LIF-fluorescence \dot{N}_{LIF}^0 with the maximum efficiency η_{max} , which depends on the lifetimes of the $|p\rangle$ and $|d\rangle$ states

$$\dot{N}_{\text{LIF}}^0(\delta_{\text{prb}}) = \eta_{\text{max}} \dot{N}_{p,f}(\delta_{\text{prb}}). \quad (14)$$

The total LIF-signal including the two competing processes is given by

$$\dot{N}_{\text{LIF}} = \dot{N}_{\text{LIF}}^0 + \underbrace{\dot{N}_{\text{LIF}}^1 + \dot{N}_{\text{LIF}}^2}_{\text{undesired}}. \quad (15)$$

The two competing processes depend on the laser polarization configuration because no scattering occurs during the time interval between the pump and the probe processes. When using perpendicular laser polarizations for the $J_s = 0 \rightarrow J_p = 1 \rightarrow J_d = 0$ pump-probe scheme or parallel polarizations in case of $J_s = 0 \rightarrow J_p = 1 \rightarrow J_d = 1$ excitation these processes can be suppressed considerably. This suppression is described by a factor η_{pol} which can range typically from 1 (no suppression) to 10^{-3} (maximum suppression). The undesired contributions are estimated in Appendix B in terms of experimental parameters.

Two handles are available to suppress the competing processes: *i*) the polarization configuration in combination with the $|s\rangle$ - $|p\rangle$ - $|d\rangle$ pump-probe scheme which determines η_{pol} , and *ii*) the detuning δ_{prb} of the probe laser. The ratios $\dot{N}_{\text{LIF}}^1/\dot{N}_{\text{LIF}}^0$ and $\dot{N}_{\text{LIF}}^2/\dot{N}_{\text{LIF}}^0$ determine whether it is possible to study the elastic scattering process of Eq. (1). The first ratio can be estimated as

$$\frac{\dot{N}_{\text{LIF}}^1}{\dot{N}_{\text{LIF}}^0} \simeq 10^4 \eta_{\text{pol}} \left(\frac{\gamma}{2\delta_{\text{prb}}} \right)^2, \quad (16)$$

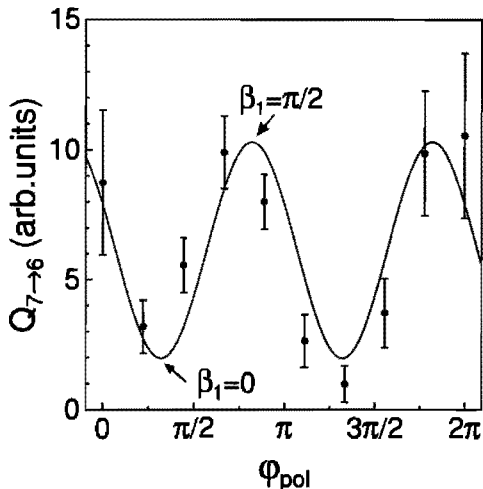


Figure 13: Typical measurement of the polarized-atom cross section $Q_{7 \rightarrow 6}$, as a function of the polarization angle φ_{pol} of the pump laser. The corresponding angle β with respect to the initial relative velocity is indicated.

where γ is the linewidth of the $|p\rangle$ - $|d\rangle$ transition, determined by the lifetimes of both states. The second ratio can be approximated by

$$\frac{\dot{N}_{\text{LIF}}^2}{\dot{N}_{\text{LIF}}^0} \simeq 100 \eta_{\text{pol}}. \quad (17)$$

Thus we conclude that it is essential to suppress the direct excitation processes maximal ($\eta_{\text{pol}} \approx 10^{-3}$) in order to study the elastic process.

5.2 Results

It is important to know the orientation of the relative velocity vector \mathbf{v}_i with respect to the lab frame indicated by angle φ_0 in Fig. 4. We calibrate the laser polarization angle φ_{pol} defined with respect to He velocity by performing a two-vector correlation experiment giving the offset angle φ_0 . The result of this measurement is shown in Fig. 13 where β_1 denotes the angle between the laser polarization \mathbf{E}_{pmp} and the relative velocity \mathbf{v}_i . Theoretically, a $\cos(2\beta_1)$ behavior is expected with a minimum for $\beta_1 = 0$ and a maximum for $\beta_1 = \pi/2$. In a least-square analysis we determine the relation between the two angles as $\beta = \varphi_{\text{pol}} - \varphi_0$ yielding an offset $\varphi_0 = 32^\circ$. The offset φ_0 also follows from the average velocities $v_{\text{Ne}} \approx 1000$ m/s and $v_{\text{He}} \approx 1800$ m/s of the crossed beams, which yields $\varphi_0 = \arctan(v_{\text{Ne}}/v_{\text{He}}) \approx 29^\circ$.

We measured the LIF-signal as a function of the detuning δ_{prb} of the probe laser for a parallel laser configuration ($\eta_{\text{pol}} = 1$). The probe parameters are given in Table 1. In Fig. 14 the results are shown for the He beam switched on and off. We adjusted He beam density n_{He} such that the transmission factor is equal to $T_i \approx 1/e$. The LIF-signal in Fig. 14 for the He beam switched off is scaled with T_i .

According to the previous section, the contribution from the competing processes \dot{N}_{LIF}^1 and \dot{N}_{LIF}^2 are not suppressed when $\eta_{\text{pol}} = 1$. Therefore, the LIF-signal will be dominated by the elastic scattering of Ne(3s), i.e., \dot{N}_{LIF}^2 , which causes the broadening



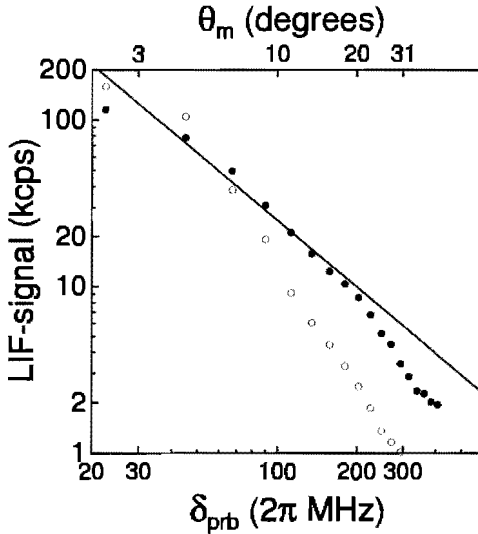


Figure 14: LIF signal ($\eta_{\text{pol}} = 1$) for the elastic scattering of $\text{Ne}(3p, \alpha_7)$ states as a function of the detuning δ_{prb} with the He beam switched on (filled markers) and off (open markers). The fluorescence for the He beam switched off is scaled with the attenuation factor $T_i = 1/e$. The solid line represents the δ_{prb} -dependence of the model function of Eq. (11) for classical small angle scattering.

that can be seen in Fig. 14. We analyze the LIF-signal measurement with the classical small angle scattering expression of Eq. (11). For a detuning $\delta_{\text{prb}} < 200(2\pi)$ MHz which corresponds to scattering angles $\theta_m < 20^\circ$ we see a fair agreement.

For the $J_s = 0 \rightarrow J_p = 1 \rightarrow J_d = 0$ pump-probe scheme the *direct* excitation ($\eta_{\text{pol}} = 1$ for parallel laser configuration) with the probe laser on resonance and the He beam switched off results in a huge LIF-signal of 300 kcps. This is efficiently reduced in the perpendicular laser configuration to only 300 cps from which follows $\eta_{\text{pol}} \approx 10^{-3}$. This countrate is superimposed on the background signal (source + pump laser + probe laser) of 260 cps. The 300 cps ‘leakage’ reduces with increasing detuning δ_{prb} . For $\delta_{\text{prb}} = 400(2\pi)$ MHz detuning the ‘leakage’ signal is smaller than the noise on the background signal. In such a far off-resonance measurement we observe no significant difference between the LIF-signal measured with the He beam switched on or off. In the case of perpendicular laser polarizations the expected LIF-signal resulting from M_J -changing collisions is estimated in the range 5 to 10 cps. The statistical noise can be reduced by increasing the measuring time. However, at the same time the drift in source operation and laser light power induces a fluctuation in the LIF-signal of the same order of magnitude as the desired signal.

We conclude that the signals for M_J -changing collisions are too small in comparison to the drift in the background signal. Quantum simulations show that the M_J -preserved collisions have cross sections about a factor 10 higher. However, the competing processes which contribute to the LIF-signal cannot be reduced in this configuration since $\eta_{\text{pol}} = 1$.

6 $\text{Ne}(3p, \alpha_9 \rightarrow \alpha_8)$ inelastic scattering

6.1 Measuring scheme

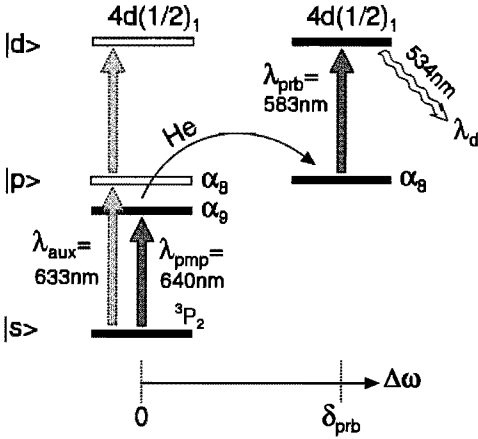


Figure 15: Pump-probe scheme for inelastic $\alpha_9 \rightarrow \alpha_8$ scattering. The dashed arrow indicates an auxiliary laser to populate the α_8 states for tuning the probe laser to the resonance frequency, *i.e.* finding the ‘zero’ point for the probe laser.

The pump-probe scheme for the inelastic collision $\alpha_9 \rightarrow \alpha_8$ is shown in Fig. 15. In this scheme the two competing contributions originating from the direct excitation of initial $|p\rangle$ states and from excitation of scattered metastable $|s\rangle$ states are eliminated. In contrast with the elastic scattering process, it is clear that now all laser configurations, *i.e.*, parallel, perpendicular and circular polarizations, can be studied.

By pumping from the 3P_2 state, a factor 5 is gained in $|p\rangle$ state population in comparison with the excitation from the 3P_0 states. Note, however, that we are not dealing with a single magnetic sublevel anymore. The two-level character of the pump transition $^3P_2 \rightarrow \alpha_9$, allows the 3P_2 states to be excited typically 25 times because the atoms reside in the laser beam about $\Delta t \approx 1 \mu s = 50\tau$. Although the cross sections for the inelastic transitions are generally much smaller than their elastic counterparts, the collision signals are enlarged by the much longer interaction length $25l_\tau \approx 0.5 \text{ mm}$ in this special configuration.

This inelastic scattering process introduces the problem of finding the probe laser transition. In contrast with the elastic probing scheme the collision induced α_8 states have to be used to find the probe transition line. Due to the small signals, the probe line cannot be detected during a course frequency scan. Therefore, an auxiliary laser is used which is tuned to the $^3P_2 \rightarrow \alpha_8$ transition. Now the α_8 states can be populated sufficiently while scanning the probe laser.

6.2 Results

In our experiment typical background signals are 50 cps from light emitted from the source, 150 cps from the pump laser and 250 cps from the probe laser, adding up to a total background signal of 450 cps. When the He beam is switched on an additional background signal of 10 cps is detected. This is caused by the altered conditions of the light production in the Ne expansion. These background signals are quite constant during a measurement and are determined every half hour. To obtain a good signal-to-noise ratio we measure 2000 seconds for each detuning of the probe laser frequency. In between two measurements the frequency drift of the probe laser is compensated for



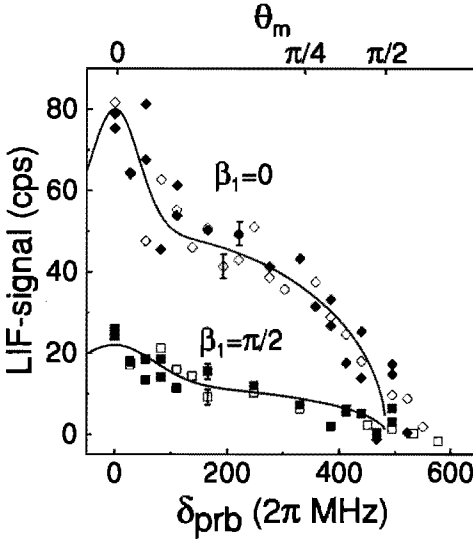


Figure 16: LIF signal measured as a function of the detuning δ_{prb} for the $\alpha_9 \rightarrow \alpha_8$ transition for different combination (β_1, β_2) of linear polarizations: diamonds ($\beta_1 = 0$); squares ($\beta_1 = \pi/2$); open markers ($\beta_2 = 0$); filled markers ($\beta_2 = \pi/2$). Two typical error bars are indicated. The solid lines represent model functions for an empirical description of the data.

by means of the auxiliary laser.

We measured the LIF-fluorescence of the $|d\rangle$ state as a function of the probe laser detuning δ_{prb} . The results for the four linear pump-probe polarization configurations, $(\beta_1, \beta_2) = (0, 0), (0, \pi/2), (\pi/2, 0), (\pi/2, \pi/2)$, are shown in Fig. 16. We see a large dependency on the pump laser polarization (β_1) . An effect of the probe laser polarization (β_2) cannot be observed. We use a model function for representing the data in a compact way. The only physical quantity which enters in this model function is the value of $\Delta\omega_{\text{max}} = 486(2\pi)$ MHz (see Table 1). We take the basis model function proportional to $[1 - (\delta_{\text{prb}}/\Delta\omega_{\text{max}})^2]^{1/2}$. An additional Gaussian function describes the forward scattered peak around $\delta_{\text{prb}} = 0$. We see perfect agreement of the cut-off at $\delta_{\text{prb}} = \Delta\omega_{\text{max}}$.

For the circular polarization we have performed measurements for the (σ^+, σ^+) and (σ^+, σ^-) configurations. The results are shown in Fig. 17. For the two polarization configurations we see a similar shape of the LIF-signal. Comparing these results to the linear polarization measurements in Fig. 16 we see that the circular measurement have a concave shape whereas the linear data display a more convex shape. We use a Lorentzian shape function to represent the data of the form $(1 + (\delta_{\text{prb}}/\delta_0)^2)^{-1}$, with $\delta_0 = 250$ MHz. A cut-off at $\delta_{\text{prb}} = \Delta\omega_{\text{max}}$ is introduced by multiplying with a Heaviside function. For the (σ^+, σ^-) configuration this feature is pronounced present in the experimental data.

Using the parameters of Section 3.1 for the flux of Ne(3s) in the scattering center $N_{s,i} \approx 1.1 \times 10^9 \text{ s}^{-1}$ and the detection efficiency $\eta_{\text{det}} = 2 \times 10^{-2}$ we can estimate the LIF-signal for Doppler probing the $\alpha_9 \rightarrow \alpha_8$ transition. In Table 6 typical quantities which determine the detected LIF-signal are given. These quantities determine the collision probability $P_{\text{col}} = n_{\text{He}} l_{\text{int}} Q_{9 \rightarrow 8}$ and the probing efficiency $\eta_{\text{LIF}} = \eta_{\text{max}} \gamma_{\text{prb}}/\Delta\omega_{\text{max}}$. The expected LIF-signal is written as the product $S = f_{\text{pmp}} N_{s,i} P_{\text{col}} \eta_{\text{det}} \eta_{\text{LIF}} \approx 35$ cps. Note, that this signal is an averaged value and that effects such as overlap of lasers, laser intensities and the effect of the polarization configuration are not taken into account.

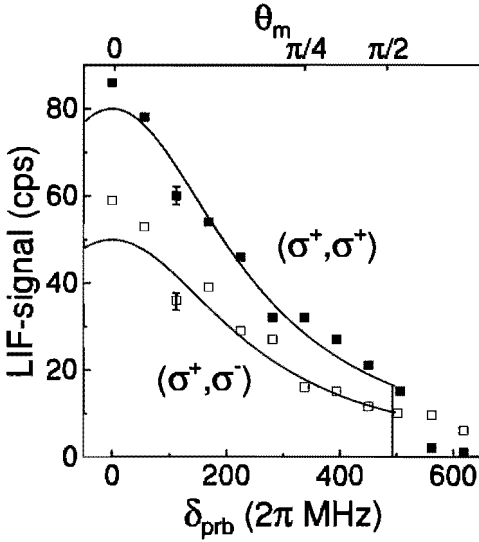


Figure 17: LIF signal measured as a function of the laser detuning δ_{prb} for the $\alpha_9 \rightarrow \alpha_8$ transition for the circular polarization combination (σ^+, σ^+) and (σ^+, σ^-) which are represented by the closed and open markers, respectively. The solid lines represent model functions for an empirical description of the data.

Table 6: Estimation of the expected signal for the $\alpha_9 \rightarrow \alpha_8$ pump-probe experiment.

	units	value	total
n_{He}	(m^{-3})	1×10^{20}	$P_{col} = n_{He} l_{int} Q = 210^{-3}$
$l_{int} \approx 25l_r$	(m)	0.5×10^{-3}	
$Q_{9 \rightarrow 8}$	(\AA^2)	3.5	
η_{max}		0.1	$\eta_{LIF} = 10^{-3}$
$\frac{\gamma_{prb}}{\Delta\omega_{max}}$		0.01	



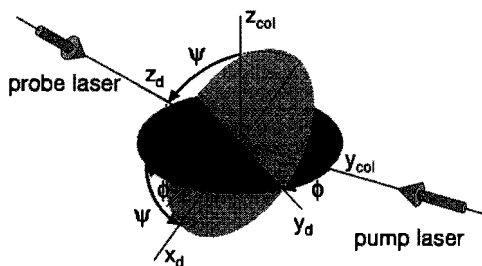


Figure 18: The collision frame $(x_{col}, y_{col}, z_{col})$ and the Doppler frame (x_d, y_d, z_d) are related by a rotation over the Euler angles (ϕ, ψ, θ) . The preparation laser beam is aligned along the y_{col} axis, the pump laser beam along the z_d axis.

Nevertheless, this estimate is in good agreement with the measured signal presented in Figs. 16 and 17.

The overlap of pump and probe laser in the scattering center is altered when changing the polarization configuration and hence the absolute value of the measured signals for the different polarization measurements cannot be compared directly. Therefore, in the further analysis only the shape of the measured cross section data will be used.

7 Comparison with theory

7.1 Coupled channels calculation

The intramultiplet mixing process of Eq. (1) is described quantum mechanically in a coupled channels calculation. Model potentials proposed by Hennecart *et al.*²²⁻²⁴ serve as an input for this calculation. Manders *et al.* extended the model potentials with a repulsive branch²⁶ and performed calculations of polarized-atom cross sections with the coupled channels code. Good agreement was found between the calculated and experimental cross sections in the thermal collision energy range $E=70-130$ meV. For super thermal collision energies in the range $E=0.5-2$ eV the calculated values are higher than the experimental cross sections, as reported by Boom *et al.*²⁰ Recently, this coupled channels program has been extended to incorporate an optical potential for describing the process of Penning ionization; it has been successfully applied to $Ne(3s/3p)+Ar$ collisions.³⁰ In that sense, the coupled channels calculations are a necessary tool for the description of these collision processes.

7.2 Numerical simulation

The basis of the simulation is formed by the scattering matrices calculated quantum mechanically in a coupled channels model. The pump-probe laser beam configuration enters the calculation in the form of two density matrices for initial state preparation and final state analysis, respectively. Next, an expression for the experimental Doppler cross section $\sigma(\chi)$ is derived. The simulation is described in detail in Ref. [31].

The simulation is set up for a general pump-probe configuration. In our case the pump laser is aligned along the y_{col} -axis, perpendicular to the initial relative velocity v_i . The collision frame $(x_{col}, y_{col}, z_{col})$ and the Doppler frame (x_d, y_d, z_d) are related by a rotation over the Euler angles (ϕ, ψ, θ) as depicted in Fig. 18. The laser configuration

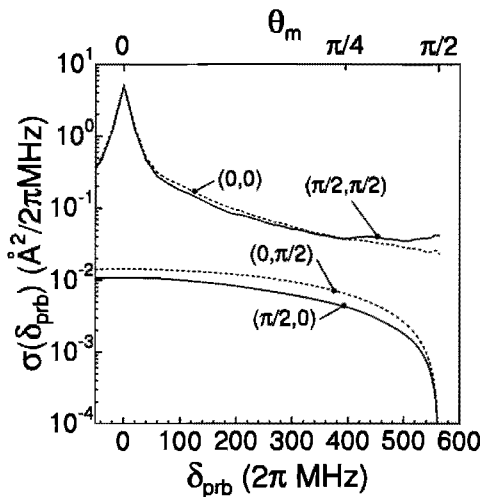


Figure 19: Quantum mechanical results for the $\alpha_7 \rightarrow \alpha_7$ transition at a collision energy $E = 70$ meV. The four basic linear polarization configurations with angles (β_1, β_2) are indicated.

used in our experiment with counter propagating laser beams is described by the Euler angles $(\phi, \psi) = (\pi/2, -\pi/2)$. The angles (β_1, β_2) introduced in Section 2.1 are now defined in terms of rotation angles around the z_{col} and z_d axis, respectively.

Simulations have been performed for the differential Doppler cross section $\sigma(\delta_{\text{prb}})$ as a function of the polarization configuration of the pump-probe laser beams and the collision energy, with δ_{prb} the probe laser detuning according to Eq. (5). Results of the simulation can be used either to investigate new pump-probe configurations or to compare to measured cross sections.

7.3 Elastic $\alpha_7 \rightarrow \alpha_7$ scattering

For the elastic process the quantum mechanical results for the four linearly polarized laser configurations are shown in Fig. 19. A clear distinction between the parallel $(0,0)$ and $(\pi/2, \pi/2)$ and the perpendicular $(0, \pi/2)$ and $(\pi/2, 0)$ laser polarization configuration can be seen. The parallel configuration probes the M_J -preserved collisions which are strongly forward peaked. The M_J -changing collision cross sections are more than a factor 10 smaller than the M_J -preserved collisions.

7.4 Inelastic $\alpha_9 \rightarrow \alpha_8$ scattering

Since the initial state α_9 with $J = 3$ is excited from the metastable 3P_2 state with $J = 2$, only the magnetic substates in the range $M_J = -2, \dots, 2$ are symmetrically populated for linearly polarized light with a population distribution g_M . This weighted distribution (g_M) of incoherently populated magnetic substates which is determined in a Monte Carlo simulation described in Ref. [32]. With this distribution we calculate the Doppler cross sections $\sigma(\delta_{\text{prb}})$ for the four linearly polarized pump-probe configurations. For the two circular polarization configurations the distribution is given by $g_M = \delta_{3,M}$.

In our experiment the initial relative velocity has a broad distribution with an



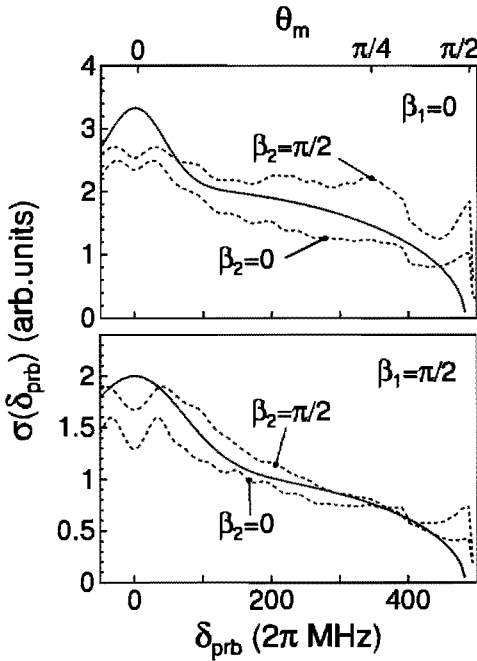


Figure 20: Quantum mechanical results for the $\alpha_9 \rightarrow \alpha_8$ transition averaged over the experimental energy distribution (dashed curves), compared with the (scaled) model functions representing the experimental results (solid curves) for linear polarization configurations with angles (β_1, β_2) as indicated.

average value $\langle v_i \rangle = 2000$ m/s and a width of 300 m/s. In a coarse approximation we calculate the differential cross sections for three collision energies 55, 70, and 85 meV and use weight factors 0.6, 1.0, and 0.6 according the energy distribution, respectively. The results of the simulation are shown in Figs. 20 and 21 for the linear and circular polarization configurations, respectively. We see a small difference in cross section values for different probe laser polarizations.

The simulated cross sections are compared with our measured data. We use different scaling factors for the $\beta_1 = 0$ and $\beta_1 = \pi/2$ measurements in the linear polarization configuration. When the polarization of the pump laser is rotated, its spatial position is slightly altered leading to a different initial Ne(3p) in the scattering center distribution and thus different scaling factors. Furthermore, due to the small nozzle-scattering center distance of 2 mm, both the collision energy and the He density vary rather strongly, over the scattering center. For instance the He density changes by 10% for a change of 0.1 mm in this position. The large waist (2 mm) of the probe laser guarantees a good overlap with the scattering center and the results are insensitive for a rotation of the probe laser polarization. In case of the circular laser polarizations the two configurations (σ^+, σ^+) and (σ^+, σ^-) are obtained by changing the probe laser polarization. A negligible effect is expected and a single scaling factor between simulated and experimental results is used.

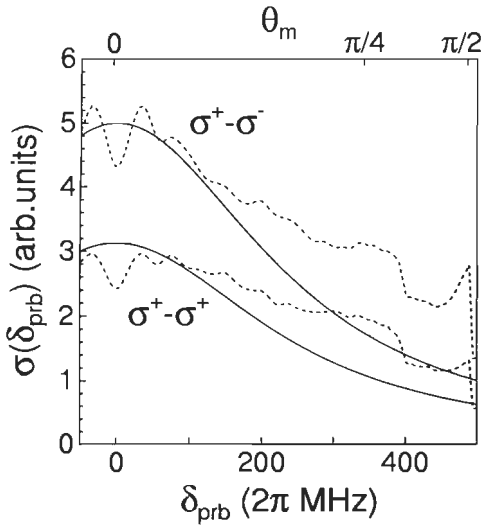


Figure 21: Quantum mechanical results for the $\alpha_9 \rightarrow \alpha_8$ transition averaged over the energy distribution (dashed curves), compared with the model functions (both scaled by the same factor) representing the experimental results (solid curves) for circular polarization configurations as indicated.

7.5 Discussion

The quantum mechanical simulations of the elastic scattering process suggest that the parallel configurations have larger cross sections than the perpendicular polarization configurations. Experimental signals for the parallel cross sections ($\eta_{\text{pol}} = 1$) are larger, but at the same time, there is a larger contribution of the undesired competing processes which scale with η_{pol} . Therefore, only the perpendicular configurations, i.e. M_J -changing processes, are good candidates for future measurements with high intensity bright metastable beams.

It should be noted that in the numerical simulation the experimental convolution effects are neglected, except for a first order energy convolution as discussed above. Two other important effects should be mentioned. First, the geometrical divergence of the Ne(3s) beam is characterized by a spread of 10 m/s in the direction of the probe laser beam which translates into an additional convolution with a block profile with a typical filter width of $30(2\pi)$ MHz. Second, the excitation process of the Ne(3p) states does not occur at a single point in space. However, Monte Carlo simulations show that the position dependence of the collision energy, the detection efficiency and the angle of the relative velocity cause an extra convolution which is not significant in comparison to the energy and perpendicular velocity spread.³²

8 Concluding remarks

Compared to the two-vector correlation experiments performed by Manders *et al.*¹⁹ and by Boom *et al.*,²⁰ we obtain an enormous amount of additional information from our LIF/Doppler probing experiment. As yet, the LIF-technique can only be applied to study the Ne($3p, \alpha_9 \rightarrow \alpha_8$) transition, with the initial laser-excited state being the upper level of a closed level system. This results in a large increase of the effective life



path this state. In the experiment of elastic collisions of $\text{Ne}(3p, \alpha_7)$ we have shown that competing processes contributing to the LIF-signal and the small signals inhibit us to study the elastic four-vector correlation process.

The good agreement between experiment and theory in shape of the differential cross sections and their relative scaling for different laser polarization configurations show the power of the model potentials.²²⁻²⁴ Even up to this level of detail they strongly support the experimentally observed features.

In the Ca-He experiments by Smith *et al.* a more detailed analysis of the experimental results in terms of coherence cross sections is possible, because the gain in signal strength is much longer both due to a ground state lower level of the Ca and the broad bandwidth of the probe laser. Comparison with theory, however, is very limited due to the scarce information on potential surfaces for these systems with two valence electrons.

The recent development of bright beams with a 10000 fold increase in beam flux and 'monochromatic' velocities³³ offers good prospects for more detailed LIF/Doppler experiments on all transitions of the Ne-He system. Elastic collisions as well as other inelastic collisions can be studied when the flux $\dot{N}_{s,i}$ of metastable atoms in the scattering center is increased drastically.

Appendices

A LIF-scheme for detecting small angle elastic scattering

In this appendix we derive an expression for small angle scattering detected with a Doppler-LIF technique. For the configuration where the pump laser is perpendicular to the initial relative velocity v_i (z -axis), the relation between the scattering angle θ and the probing direction (χ, ζ) of Eq. (6) has to be used to derive an expression for the fluorescence signal as a function of the laser detuning δ_{prb} . Basically, the signal is proportional to the $n l Q$ product and we find for the signal

$$S(\delta_{\text{prb}}) = C \langle n_{\text{He}} \rangle l_s \int_{\chi}^{\chi+\Delta\chi} \int_0^{2\pi} d\zeta \sigma[\theta(\chi, \zeta)] \sin \chi' d\chi', \quad (\text{A1})$$

where C is a scaling constant, $\langle n_{\text{He}} \rangle$ is the average He beam density, and l_s is the scattering length of the metastable atoms (≈ 2 mm). The solid angle element is represented by $d\Omega = \sin \chi' d\chi' d\zeta$. The finite χ integration denotes the resonance condition. A more accurate expression for the signal is obtained by integrating over the Lorentz profile $\mathcal{L}(\omega, \gamma_{\text{eff}})$ of the transition:

$$S(\delta_{\text{prb}}) = C \langle n_2 \rangle l_s \int_{-\infty}^{\infty} d\omega \int_0^{2\pi} d\zeta \mathcal{L}(\delta_{\text{prb}} - \omega, \gamma_{\text{eff}}) \sigma[\theta(\chi(\omega), \zeta)], \quad (\text{A2})$$

with $|\delta_{\text{prb}}| < \Delta\omega_{\text{max}}$. To evaluate the above expression we use Eqs. (5) and (6). We assume that the cross section $\sigma(\omega, \zeta)$ is constant over the width of the Lorentz profile. This approximation reduces the ω integration to unity. We find for the signal

$$S(\delta_{\text{prb}}) = C' \langle n_2 \rangle l_s \int_0^{2\pi} d\zeta \sigma[\theta(\chi(\delta_{\text{prb}}), \zeta)]. \quad (\text{A3})$$

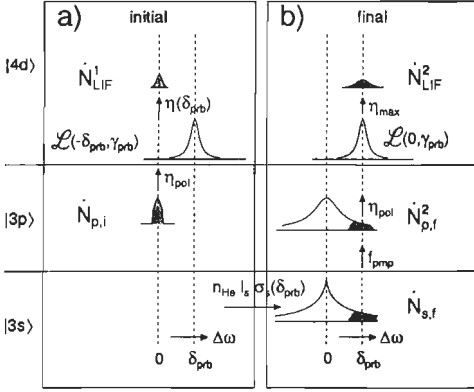


Figure B1: Schematic representation of competing processes which contributing to the LIF-signal of the elastic scattering probing scheme: a) direct probing of initial $|p\rangle$ states and b) probing of scattered $|s\rangle$ states.

The integral over the azimuthal angle ζ is integrated numerically. When the semiclassical expression for $\theta > \theta_0$ in Eq. (10) is substituted in the integrand, the integral can be approximated by

$$S(\delta_{\text{prb}}) \approx C' \langle n_2 \rangle l_s (\pi/2 + 1) [\pi/2 - \chi(\delta_{\text{prb}})]^{-4/3}. \quad (\text{A4})$$

The exact approximation of the integral with the expression above within 1% in the range $0 < \pi/2 - \chi < 0.5$ strongly suggest that a “real” mathematician should be able to derive this expression analytically.

B Competing processes in the LIF signal for elastic scattering

The two competing processes contributing to the population of the $|d\rangle$ state are graphically represented in Fig. B1 in more detail. The first competing process is the direct excitation of initial $|p\rangle$ to $|d\rangle$ which is depicted in Fig. B1(a). These unscattered $|p\rangle$ states are not resonant with the probe laser. Thus, they are converted to LIF-photons less efficiently in the off-resonance tail of the line profile as given by

$$\eta(\delta_{\text{prb}}) = \eta_{\text{max}} \frac{\mathcal{L}(\delta_{\text{prb}}, \gamma)}{\mathcal{L}(0, \gamma)} = \eta_{\text{max}} \frac{1}{1 + (2\delta_{\text{prb}}/\gamma)^2}, \quad (\text{B5})$$

where γ is the linewidth of the $|p\rangle \rightarrow |d\rangle$ transition and $\mathcal{L}(\Delta\omega, \gamma)$ denotes the Lorentz line shape function. The contribution of the direct excitation can now be written as

$$\dot{N}_{\text{LIF}}^1 = \eta_{\text{pol}} \eta(\delta_{\text{prb}}) \dot{N}_{\text{p,i}}, \quad (\text{B6})$$

with $\dot{N}_{\text{p,i}}$ given in Eq. (8).

The second competing process is more complicated and is depicted in Fig. B1(b). Even though the $|s\rangle$ states may be scattered out of resonance, they can still be pumped in the tails of the Lorentz-profile. These excited $|p\rangle$ states cannot be distinguished from the actual scattered $|p\rangle$ states that we are interested in. The collision rate $\dot{N}_{\text{s,f}}(\delta_{\text{prb}})$ for $|s\rangle$ state scattering is obtained thru the effective density length product

$$\dot{N}_{\text{s,f}}(\delta_{\text{prb}}) = n_{\text{He}} l_s \sigma_s(\delta_{\text{prb}}) \dot{N}_{\text{s,i}}, \quad (\text{B7})$$



with $\sigma_s(\delta_{\text{prb}})$ being the differential cross section for scattering. Because these scattered $|s\rangle$ states reside in the laser beam for a long time ($\Delta t \approx 1 \mu\text{s} \approx 50\tau$), eventually they will be excited by the pump laser

$$\dot{N}_{p,f}^2(\delta_{\text{prb}}) = f_{\text{pmp}} \dot{N}_{s,f}(\delta_{\text{prb}}) = n_{\text{He}} l_s \sigma_s(\delta_{\text{prb}}) \dot{N}_{p,i}, \quad (\text{B8})$$

where we substituted Eq. (8). These excited $|p\rangle$ states contribute to the LIF-signal with the same efficiency η_{max} as the scattered $|p\rangle$ states. However, because they have not collided in between the two excitation processes, this undesired contribution may be suppressed by the same factor η_{pol} as in Eq. (B6) and can be written as

$$\dot{N}_{\text{LIF}}^2(\delta_{\text{prb}}) = \eta_{\text{pol}} n_{\text{He}} l_s \sigma_s(\delta_{\text{prb}}) \dot{N}_{p,i}. \quad (\text{B9})$$

The ratios $\dot{N}_{\text{LIF}}^1/\dot{N}_{\text{LIF}}^0$ and $\dot{N}_{\text{LIF}}^2/\dot{N}_{\text{LIF}}^0$ can now be estimated. The first ratio can be written as

$$\frac{\dot{N}_{\text{LIF}}^1}{\dot{N}_{\text{LIF}}^0} = \eta_{\text{pol}} \frac{1}{1 + (2\delta_{\text{prb}}/\gamma)^2} \frac{1}{n_{\text{He}} l_\tau \sigma_p(\delta_{\text{prb}})} \simeq \eta_{\text{pol}} \left(\frac{\gamma}{2\delta_{\text{prb}}} \right)^2 \frac{1}{n_{\text{He}} l_\tau \sigma_p(\delta_{\text{prb}})}, \quad (\text{B10})$$

where we assume that $\gamma \ll \delta_{\text{prb}}$. With $n_{\text{He}} \approx 10^{20} \text{ m}^{-3}$, $l_\tau \approx 20 \mu\text{m}$ and $\sigma_p(\delta_{\text{prb}}) \approx O(5 \times 10^{-19} \text{ m}^2)$ we find

$$\frac{\dot{N}_{\text{LIF}}^1}{\dot{N}_{\text{LIF}}^0} \simeq 10^4 \eta_{\text{pol}} \left(\frac{\gamma}{2\delta_{\text{prb}}} \right)^2. \quad (\text{B11})$$

The second ratio can be approximated by

$$\frac{\dot{N}_{\text{LIF}}^2}{\dot{N}_{\text{LIF}}^0} \simeq \eta_{\text{pol}} \frac{l_s \sigma_s(\delta_{\text{prb}})}{l_\tau \sigma_p(\delta_{\text{prb}})}. \quad (\text{B12})$$

For the two interaction lengths we have, $l_s \approx 2 \text{ mm}$ for the $|s\rangle$ state, and $l_\tau \approx 20 \mu\text{m}$ for the $|p\rangle$ state. Assuming that the cross sections σ_s and σ_p are similar in magnitude, this ratio can be estimated with

$$\frac{\dot{N}_{\text{LIF}}^2}{\dot{N}_{\text{LIF}}^0} \simeq 100 \eta_{\text{pol}}. \quad (\text{B13})$$

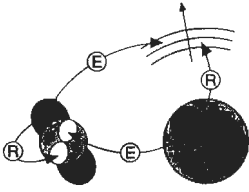
References

- [1] M. Manders, J. Driessen, H. Beijerinck, and B. Verhaar, Phys. Rev. Lett. **57**, 1577,2472 (1986).
- [2] J. Driessen and S. Leone, J. Chem. Phys **96**, 6136 (1992).
- [3] E. Spain, M. Dalberth, P. Kleiber, S. Leone, S. Op de Beek, and J. Driessen, J. Chem. Phys **102**, 9522, 9532 (1995).
- [4] A. Suits, H. Hou, H. Floyd Davis, Y. Lee, and J.-M. Mestdagh, J. Chem. Phys **95**, 8178 (1991).
- [5] C. Smith, J. Driessen, L. Eno, and S. Leone, J. Chem. Phys **96**, 8212 (1992).
- [6] C. Smith, E. Spain, M. Dalberth, S. Leone, and J. Driessen, J. Chem. Soc. Faraday Trans. **89**, 1401 (1993).
- [7] R. Düren, E. Hasselbrink, and H. Tisher, Phys. Rev. Lett. **50**, 1983 (1983).
- [8] E. Campbell, H. Hüsler, R. Witte, and I. Hertel, Z. Phys. D **16**, 21 (1990).

- [9] H. Meijer, *Z. Phys. D* **17**, 257 (1990).
- [10] N. Andersen, J. Gallagher, and I. Hertel, *Phys. Rep.* **165**, 1 (1988).
- [11] G. Nienhuis, *Phys. Rev. A* **26**, 3137 (1982).
- [12] J. Grosser, *J. Phys. B* **14**, 1449 (14).
- [13] L. Kovalenko, S. Leone, and J. Delos, *J. Chem. Phys.* **91**, 6948 (1991).
- [14] G. Schatz, L. Kovalenko, and S. Leone, *J. Chem. Phys.* **91**, 6961 (1989).
- [15] R. Dubs, P. Julienne, and F. Mies, *J. Chem. Phys.* **93**, 8784 (1990).
- [16] B. Pouilly and M. Alexander, *J. Phys.* **145**, 191 (1990).
- [17] J. Driessen and L. Eno, *J. Chem. Phys.* **97**, 5532 (1992).
- [18] R. de Vivie-Riedle, J. Driessen, and S. Leone, *J. Chem. Phys.* **98**, 2038 (1993).
- [19] M. Manders, W. Ruyten, F. v.d. Beuken, J. Driessen, W. Veugelers, P. Kramer, E. Vredenburgt, W. van Hoek, G. Sandker, H. Beijerinck, and B. Verhaar, *J. Chem. Phys.* **89**, 4777 (1988).
- [20] W. Boom, R. van Galen, B. Klaver, S. Op de Beek, J. Heier, H. Beijerinck, and B. Verhaar, *Phys. Rev. A* **51**, 3837 (1995).
- [21] T. Collins, A. McCaffery, and M. Wynn, *Faraday Discuss. Chem. Soc.* **91**, 91 (1991).
- [22] D. Hennecart and F. Masnou-Seeuws, *J. Phys. B* **18**, 657 (1985).
- [23] D. Hennecart, Ph.D. thesis, Université de Caen, Caen, France, 1982, unpublished.
- [24] H. Kucal, D. Hennecart, and F. Masnou-Seeuws, *Chem. Phys.* **145**, 163 (1990).
- [25] M. Verheijen, H. Beijerinck, L. van Moll, J. Driessen, and N. Verster, *J. Phys. E: Sci. Instrum.* **17**, 904 (1984).
- [26] M. Manders, W. van Hoek, E. Vredenburgt, G. Sandker, H. Beijerinck, and B. Verhaar, *Phys. Rev. A* **39**, 4467 (1989).
- [27] H. Megens, *Design of a continuously tunable linewidth narrowed diode laser system* (Eindhoven Univ. of Tech., The Netherlands, 1993), isbn 90-5282-235-2.
- [28] H. Beijerinck, P. van der Kam, W. Thijssen, and N. Verster, *Chem. Phys.* **45**, 225 (1980).
- [29] J. Henrichs, H. Beijerinck, and N. Verster, *Chem. Phys.* **70**, 93 (1982).
- [30] S. Op de Beek, J. Driessen, S. Kokkelmans, H. Beijerinck, and B. Verhaar, chapter 4 of this thesis, to be published.
- [31] S. Op de Beek, J. Driessen, H. Beijerinck, and B. Verhaar, chapter 2 of this thesis, to be published.
- [32] S. Op de Beek, Master's thesis, Eindhoven University of Technology, The Netherlands, 1992, report NO 92-18, unpublished.
- [33] M. Hoogerland, J. Driessen, E. Vredenburgt, H. Megens, M. Schuwer, H. Beijerinck, and K. van Leeuwen, *Appl. Phys. B* **62**, 323 (1996).







4

Ionization widths for Ne(3*l*)-Ar systems (*l*=s,p): application to ionization and intramultiplet mixing cross sections

S.S. Op de Beek, J.P.J. Driessen, S.J.J.M.F. Kokkelmans,
W. Boom, H.C.W. Beijerinck, and B.J. Verhaar

Ab initio autoionization widths for the Ne(3s)-Ar and Ne(3p)-Ar systems are calculated in a two-electron approximation. Using correctly normalized wave functions the calculations result in absolute values for the autoionization widths. We use a modified coupled channels code with ab initio potentials and ionization widths as input to calculate cross sections for ionization and intramultiplet mixing. For the very first time, the influence of ionization on the intramultiplet mixing process can be studied. Experimental results for intramultiplet mixing cross sections for the Ne(3p)-Ar system at a collision energy $\langle E \rangle = 1.7$ eV are presented. These data and ionization cross sections obtained by Bussert *et al.* are in good agreement with coupled channels calculations. For the Ne(3s)-Ar system the calculated ionization widths are in good agreement with empirical ionization widths derived in a multiproperty analysis of a wide range of scattering data. For this system we have to conclude that the ab initio results cannot explain the experimental cross section ratio $Q(^3P_0)/Q(^3P_2)=1.3$. Therefore, ab initio calculations of the real part of the potential are essential for a correct quantum mechanical coupled channel analysis.



1 Introduction

Collisions of electronically excited atoms with ground state atoms have been the subject of various theoretical studies during the last two decades. Ionization is possible if the electronic energy exceeds the ionization energy of the ground state atom. This process is referred to as Penning or associative ionization, depending on whether the final state is an atomic or molecular ion. The ionization process can be described by the imaginary part of a complex (optical) potential $V_{\text{opt}}(R)$ given by

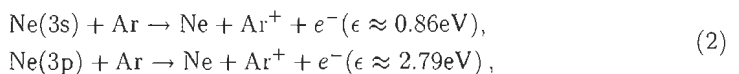
$$V_{\text{opt}}(R) = V(R) - \frac{1}{2} i \Gamma(R). \quad (1)$$

Classically, the real part $V(R)$ determines the trajectories, whereas the autoionization width $\Gamma(R)$ takes into account the loss of flux due to ionization. The ionization rate at an internuclear distance R is equal to $\Gamma(R)/\hbar$.

These optical potentials can be derived from experimental data in a multiproperty analysis, *i.e.*, by analyzing the combined results of various experiments like small angle scattering, total ionization cross sections (Penning and associative), free electron energy distributions, and elastic differential scattering cross sections.^{1,2} The real part of the potential is often described by a flexible potential with many adjustable parameters to control the attractive and repulsive parts, with the Morse-Morse-spline-van der Waals (MMSV) and Ion-Atom MMSV potentials as typical examples.^{3,4} The imaginary part is assumed to be an exponential function, based on the interatomic orbital overlap which decreases exponentially with the internuclear distance. Unfortunately, a strong correlation between the parameters describing the real and imaginary part in such an analysis cannot be excluded. This can be directly understood by considering that ionization occurs preferentially close to the classical turning point R_t of the trajectory, due to the long residence time at this point and the exponential behavior of $\Gamma(R)$. This results in a strong correlation of the absolute value of $\Gamma(R)$ and the exact shape and location of the repulsive branch of $V(R)$. As Gregor *et al.* discuss in their paper,³ the number of free parameters in the real part of the potential is so large that acceptable fits to experimental elastic differential cross sections can be achieved with totally different ionization widths. Therefore, additional constraints in the form of experimental data on the cross section for ionization or ab initio calculations are needed.

The ab initio calculation for the ionization width presented in this paper is basically the same as in the analysis of Driessen *et al.*⁵ Using a different numerical approach⁶ we are able to obtain *absolute* values of Γ . Driessen *et al.* only considered the pure triplet states $\text{Ne}(3s, {}^3P_2)$ and $\text{Ne}(3p, {}^3D_3)$. In our treatment the autoionization widths are calculated for all states of the $\text{Ne}(3s)$ and $\text{Ne}(3p)$ multiplets. To check the numerical results of our calculated widths, we compare the calculated results with experimental data through a semiclassical or quantum mechanical collision model.

Experimental data are available for the Penning ionization process of the systems



where ϵ is the energy of the emitted electron. Optical potentials have been proposed for these systems by several groups.^{2-4,7} The vast amount of experimental data available

for these systems gives a lot of information about parameters in different regions of the interaction potentials. Still, a large uncertainty in these parameters exists. The state-averaged $\text{Ne}(3s, {}^3P_{0,2})\text{-Ar}$ data give reliable values for the ionization width which can be confronted with our ab initio calculations. Verheijen *et al.*⁴ present accurate state selected data for the ionization cross sections $Q({}^3P_0, E)$ and $Q({}^3P_2, E)$ in a broad energy range of 0.05-2 eV. In a semiclassical analysis of their data they adjusted both the repulsive branch of the potentials of Gregor *et al.* and the autoionization width. Finally, using a least-squares analysis they determined a best fit optical potential for the two systems: $\text{Ne}(3s, {}^3P_0)\text{-Ar}$ and $\text{Ne}(3s, {}^3P_2)\text{-Ar}$.

Only a few groups have investigated the ionization process of the $\text{Ne}(3p)\text{-Ar}$ system.^{8,9} Accurate optical potential parameters cannot be extracted from the scarce experimental data because, as mentioned above, a large interdependence of parameters of the real and imaginary part of the potentials cannot be excluded. For the $\text{Ne}(3p)\text{-Ar}$ system intramultiplet mixing cross sections have been measured, as presented in this paper. Including the ab initio autoionization widths in a coupled channels calculation results in an additional check for the ionization potentials.

Recently, "optical" collisions are in the focus of many experimental and theoretical groups.¹⁰ The $\text{Ne}(3s)+\text{Ne}(3p)$ system is an excellent candidate to investigate ionization for low energy "optical" collisions. No experimental data is available as yet. Due to the flexibility of our numerical recipe⁶ the two-center two-electron integrals involved in the ab initio calculation can easily be calculated for this system. The actual construction of the autoionization widths from these integrals is complicated by the intricate nature of the molecular $\text{Ne}(3s)\text{-Ne}(3p)$ -states and the additional symmetries involved. However, a good estimate of the ionization processes can be achieved on the basis of a set of ab initio autoionization widths.

In this paper we present ab initio imaginary potentials for the $\text{Ne}(3l)\text{-Ar}$ systems with $l = s, p$ based on a two-electron model.⁵ In Section 2 we describe the composition of the ionization width in terms of two-center two-electron integrals, which are calculated using the numerical recipe of Ref. [6]. The actual calculation of ionization widths for the $\text{Ne}(3s/3p)\text{-Ar}$ system is reported in Section 3. If we consider the $\text{Ne}(3p)\text{-Ar}$ system, intramultiplet mixing is a competing inelastic channel. A coupled channels program is available to calculate the cross sections for intramultiplet mixing. This coupled channels code has been extended to include the ionization process. Section 4 will deal with this extension and with tests for the new code. Next, we discuss the results of the coupled channels calculation for the $\text{Ne}(3p)\text{-Ar}$ system for the ionization cross sections and the cross sections for intramultiplet mixing in Section 5. The cross sections for the $\text{Ne}(3s)\text{-Ar}$ are discussed in Section 6. Suggestions for future calculations are described and conclusions are drawn in the final Section 7.

2 Calculation of ionization widths

A quantum mechanical description of the ionization process for the $\text{Ne}(3l)\text{-Ar}$ systems is given by Driessen *et al.*⁵ for 3s and 3p valence electrons. They use the projection operator formalism, which has been adapted to collisional ionization by O'Malley¹¹ and



Bieniek.¹² In this section we will briefly review this method of calculating autoionization widths.

A rigorous description of the ionization process would involve all electron wave functions of the two colliding atoms. However, since essentially only two electrons are actively involved in the transition to the ionization channel, we restrict ourselves to a two-electron description.⁵ Depending on the role which they play in this process, we can distinguish two different mechanisms. First, the *radiative mechanism* in which the Ne(3*l*) valence electron decays into the Ne(2p)⁻¹ core hole while an Ar(3p) core electron is ejected as a free electron. Second, the *exchange mechanism* where the two electrons are exchanged during the ionization, resulting in the occupation of the Ne(2p)⁻¹ core hole with the Ar(3p) valence electron and the ejection of the Ne(3*l*) electron as a free electron.

The ionization rate $\Gamma(R)$ is constructed from the following two-center two-electron integrals⁵

$$\begin{aligned}
 V^{\text{rad}}(R; l m_{l,\text{Ar}} m_{l,c} m_{l,v} \lambda \mu) &= \iint d\mathbf{r}_1 d\mathbf{r}_2 \Psi_{3p, m_{l,\text{Ar}}}^{\text{Ar}}(\mathbf{r}_1) \Psi_{\lambda \mu}^{\text{Ar}*}(\mathbf{r}_1) \frac{e^2}{4\pi\epsilon_0 |\mathbf{r}_1 - \mathbf{r}_2|} \Psi_{3l, m_{l,v}}^{\text{Ne}}(\mathbf{r}_2) \Psi_{2p, m_{l,c}}^{\text{Ne}*}(\mathbf{r}_2) \\
 &= \frac{e^2}{4\pi\epsilon_0} \langle 1 m_{l,\text{Ar}}; \lambda \mu | r_{12}^{-1} | l m_{l,v}; 1 m_{l,c} \rangle_{\lambda}^{\text{rad}}, \quad (3)
 \end{aligned}$$

$$\begin{aligned}
 V^{\text{exch}}(R; l m_{\text{Ar}} m_{l,c} m_{l,v} \lambda \mu) &= \iint d\mathbf{r}_1 d\mathbf{r}_2 \Psi_{3l, m_{l,v}}^{\text{Ne}}(\mathbf{r}_1) \Psi_{\lambda \mu}^{\text{Ar}*}(\mathbf{r}_1) \frac{e^2}{4\pi\epsilon_0 |\mathbf{r}_1 - \mathbf{r}_2|} \Psi_{3p, m_{l,\text{Ar}}}^{\text{Ar}}(\mathbf{r}_2) \Psi_{2p, m_{l,c}}^{\text{Ne}*}(\mathbf{r}_2) \\
 &= \frac{e^2}{4\pi\epsilon_0} \langle l m_{l,v}; \lambda \mu | r_{12}^{-1} | 1 m_{l,\text{Ar}}; 1 m_{l,c} \rangle_{\lambda}^{\text{exch}}, \quad (4)
 \end{aligned}$$

where Ψ denotes the electron wave function of each of the two electrons involved. All quantum numbers in this expression are given in a single coordinate system where the internuclear axis serves as the quantization axis. The subscripts *c* and *v* relate to the core and the valence electron of the neon atom, respectively. The emitted electron is characterized by the orbital angular momentum quantum numbers (λ, μ), with μ representing the projection on the internuclear axis. The corresponding free electron wave function is a rapidly oscillating function extending to infinity. The other three electron wave functions are bound states with magnetic quantum numbers $m_{l,\text{Ar}}$, $m_{l,c}$, and $m_{l,v}$ for the Ar(3p)-, Ne(2p⁻¹)- and Ne(3*l*) states, respectively. The interaction responsible for the ionization process is the electronic Coulomb repulsion. The integration variables \mathbf{r}_1 and \mathbf{r}_2 are the position vectors of electron 1 and 2. Note that the function $\Psi_{lm}^X(\mathbf{r}_i)$ describes the wave function of electron *i* with respect to nucleus *X*. The angular part is expressed as a spherical harmonic Y_{lm} and the radial part as a function of the distance of electron *i* to nucleus *X*.

To evaluate the two-center two-electron integrals, the wave functions are expanded in so-called Slater-type orbitals (STO's). For the Ar(3p) bound state wave functions we use the representation given by Clementi.¹³ For the Ne(3s), Ne(3p) and Ne(2p) orbitals

we use the atomic wave functions calculated by Haberland¹⁴ to obtain a superposition of three or four STO's. The functions $\Psi_{\lambda\mu}(r)$ are free electron wave functions calculated by solving the Schrödinger equation in the screened Ar^+e^- Coulomb potential as given by Aymar.¹⁵ These rapidly oscillating wave functions are described by a superposition of Slater-type orbitals with complex-valued exponents $\zeta = \zeta_r + i\zeta_i$, or so-called CSTO's given by $\chi_{nlm}(r; \zeta) \sim r^{n-1} e^{\zeta_r r} \cos(\zeta_i r + \phi) = r^{n-1} \text{Re}(e^{-\zeta r} e^{i\phi})$ as introduced by Op de Beek *et al.*⁶

Using the radiative and exchange matrix elements in Eqs. (3) and (4) we construct matrix elements for the actual atomic states. The fine structure states of the $\text{Ne}(3s)$ and $\text{Ne}(3p)$ multiplets will be labeled $\text{Ne}(3l, \alpha J \Omega)$, with α a characteristic index and J the total angular momentum quantum number with $\Omega = |M_J|$. We use the Paschen numbering for both configurations: for the $(3s)$ -configuration with $\alpha_i^s = 1s_i$ ($i = 2, \dots, 5$) and $\alpha_i^p = 2p_i$ ($i = 1, \dots, 10$) for the $(3p)$ -configuration. In principle the atomic states $\text{Ne}(3l, \alpha J \Omega)$ are found by diagonalizing the total atomic Hamiltonian.¹⁶ However, in our calculation we use $|LSJ\rangle$ states, with L and S the orbital momentum and spin quantum numbers, respectively. The atomic states $\text{Ne}(3l, \alpha J \Omega)$ are well-defined superposition states of pure $|LSJ\rangle$ states with expansion coefficients $M_{\alpha \rightarrow LS}$.¹⁷ In this paper we use the LSJ -notation for the pure 3P_0 and 3P_2 states and we omit the superscripts for α_i^s and α_i^p when the l -value is apparent from its contents.

For the construction of the atomic ionization matrix elements we have to know the composition of the $\text{Ne}(3l, \alpha J \Omega)$ - and $\text{Ar}^+(J_f \Omega_f)$ states in terms of the basic Ψ_{lm} -orbitals used in the two-electron two-center integrals. This analysis has been described elsewhere⁵ and will only be summarized in this paper.

For the initial and final states of the electrons involved fully anti-symmetric wave functions are used through the second quantization formalism.¹⁸ The ionization matrix elements for a pure $|LSJ\rangle$ initial state and a $|J_f \Omega_f\rangle$ final state are given by

$$\begin{aligned}
 V(R; l, LSJ\Omega \rightarrow J_f \Omega_f, \lambda \mu m_s) &= \frac{e^2}{4\pi\epsilon_0} \\
 &\times \sum_{m_{l,v}} \sum_{m_{l,c}} \sum_{m_{s,v}} \sum_{m_{s,c}} A^{\text{Ne}(3l)}(LSJ\Omega, m_{l,v} m_{l,c} m_{s,v} m_{s,c}) \\
 &\times \sum_{m_{l,\text{Ar}}} \sum_{m_{s,\text{Ar}}} B^{\text{Ar}^+}(J_f \Omega_f, m_{l,\text{Ar}} m_{s,\text{Ar}}) \\
 &\times \left\{ \delta_{m_s m_{s,v}} \delta_{m_{s,c} m_{s,\text{Ar}}} \langle l m_{l,v}; \lambda \mu | r_{12}^{-1} | 1 m_{l,\text{Ar}}; 1 m_{l,c} \rangle^{\text{exch}} \right. \\
 &\quad \left. - \delta_{m_s m_{s,\text{Ar}}} \delta_{m_{s,c} m_{s,v}} \langle l m_{l,\text{Ar}}; \lambda \mu | r_{12}^{-1} | 1 m_{l,v}; 1 m_{l,c} \rangle^{\text{rad}} \right\}, \quad (5)
 \end{aligned}$$

where m_l and m_s are the magnetic quantum numbers of the electronic states involved. The Kronecker deltas of the spin quantum numbers arise because the Coulomb interaction does not affect the electron spin. The electron spins of the initial and final state must therefore have the same magnetic quantum number. Here, A and B are the expansion coefficients of the antisymmetric initial and final states, decomposed in terms of the electronic $|l m_l\rangle |s m_s\rangle$ basis states and are given by

$$A^{\text{Ne}(3l)}(LSJ\Omega, m_{l,v} m_{l,c} m_{s,v} m_{s,c}) = \sum_{M_L} \sum_{M_S} (L M_L S M_S | J \Omega)$$

$$\begin{aligned} & \times \sum_{m_{l,v}} \sum_{m_{l,c}} (-1)^{1-m_{l,c}} (1-m_{l,c}) |L M_L\rangle \\ & \times \sum_{m_{s,v}} \sum_{m_{s,c}} (-1)^{\frac{1}{2}-m_{s,c}} \left(\frac{1}{2} - m_{s,c} \right) \frac{1}{2} m_{s,v} |S M_S\rangle, \end{aligned} \quad (6)$$

and the final Ar⁺-ion state by

$$\begin{aligned} B^{\text{Ar}^+}(J_I \Omega_I, m_{l,\text{Ar}} m_{s,\text{Ar}}) = \\ \sum_{m_{l,\text{Ar}}} \sum_{m_{s,\text{Ar}}} (-1)^{1-m_{l,\text{Ar}}} (-1)^{\frac{1}{2}-m_{s,\text{Ar}}} (1-m_{l,\text{Ar}}) \frac{1}{2} - m_{s,\text{Ar}} |J_I \Omega_I\rangle. \end{aligned} \quad (7)$$

The factors $(-1)^{j-m_j}$ arise because the cores are represented by $(np)^{-1}$ -orbitals rather than $(np)^5$. Finally, by applying the transformation represented with the matrix $M_{\alpha \rightarrow LS}$ we get the real-valued atomic ionization matrix elements $V(R; l, \alpha J \Omega \rightarrow J_I \Omega_I, \lambda \mu m_s)$. From these matrix elements we construct the total autoionization width for the initial atomic states $|\alpha J \Omega\rangle$ as given by

$$\begin{aligned} \Gamma(R; l \alpha J \Omega) &= \sum_{\lambda} \frac{2\pi}{\hbar} \left\{ \frac{m_e}{\hbar q(R)} \sum_{J_I \Omega_I} \sum_{\mu m_s} V(R; l \alpha J \Omega \rightarrow J_I \Omega_I \lambda \mu m_s)^2 \right\} \\ &= \sum_{\lambda} \Gamma_{\lambda}(R; l \alpha J \Omega), \end{aligned} \quad (8)$$

with $q(R)$ being the local wave number of the emitted electron. The factor $2\pi/\hbar$ originates from the application of Fermi's "golden rule".¹⁹ The bound-state wave functions in Eqs. (3) and (4) are normalized to 1; the continuum state is normalized according to $\langle \phi_{q' \lambda' \mu'} | \phi_{q \lambda \mu} \rangle = \delta(q' - q) \delta_{\lambda' \lambda} \delta_{\mu' \mu}$ which results in a factor $m_e/\hbar q(R)$.

The final expression for the ionization width gives absolute values with no extra scaling involved. In the following sections we will omit the label l (denoting the valence electron angular momentum) in the parameter list of Γ if its value is clear from the context.

3 Ionization widths for Ne(3s,3p)-Ar

3.1 Energy of emitted electron

In the "local approximation" the kinetic energy of the emitted electron is given by

$$\epsilon(R) = V_i(R) - V_f(R), \quad (9)$$

where $V_i(R)$ and $V_f(R)$ are the potentials of the initial Ne($3l$)-Ar system and the final Ne-Ar⁺-system, respectively. Here we assume that the recoil transferred to the heavy particles on electron ejection can be neglected. For the Ne(3p)-Ar system we take a single value for the kinetic energy ϵ_0 given by the asymptotic energy difference $\epsilon(R \rightarrow \infty)$. In case of the Ne(3s)-Ar system, the relative variations in $\epsilon(R)$ are larger than for the Ne(3p)-Ar system and the R -dependency is not neglected in this analysis. The potential curves for the molecular Ne(3s)-Ar states are shown in Fig. 1. The relative

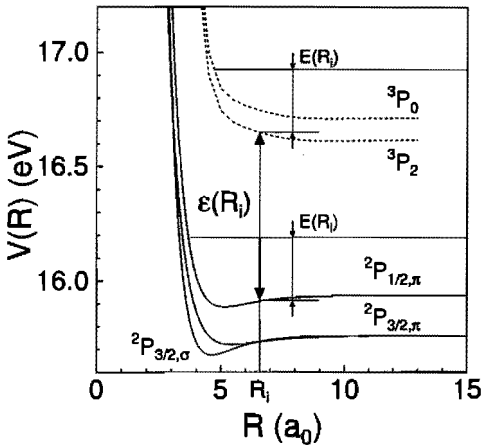


Figure 1: Potential curves of the initial Ne(3s)+Ar and the final Ne-Ar⁺-systems. The relative kinetic energy $E(R_i)$ is conserved and $\epsilon(R_i)$ represents the energy of the emitted electron.²⁰

Table 1: Calculated results for the Ne(3s)-Ar exchange integrals $\langle m_v; \mu | r_{12}^{-1} | m_{Ar}; m_c \rangle_\lambda^{\text{exch}}$ for $\lambda = 0$ at a fixed internuclear distance $R = 3.5 a_0$ as a function of the free electron energy ϵ .

ϵ (eV)	$\langle 00 r_{12}^{-1} 00 \rangle$	$\langle 00 r_{12}^{-1} 11 \rangle$
0.68	-0.5459×10^{-2}	0.1547×10^{-2}
0.83	-0.5515×10^{-2}	0.1548×10^{-2}
0.99	-0.5530×10^{-2}	0.1537×10^{-2}
1.39	-0.5449×10^{-2}	0.1475×10^{-2}
2.62	-0.4832×10^{-2}	0.1195×10^{-2}

kinetic energy $E(R_i)$ is conserved during the spontaneous ionization at position R_i . We use Ne-Ar⁺-potentials proposed by Bussert.⁸ For the Ne(3s, ³P_{0,2})-Ar potentials we use the interaction potential given by Gregor *et al.* added to the respective asymptotic energies of the two states. In contrast with Driessen *et al.*, we calculate the free electron wave function as a function of the R -dependent kinetic energy of the emitted electron.

For all electron energies used in the calculation the wave function is described by a superposition of three to four CSTO's. To study the sensitivity of the two-electron two-center integral to the energy of the emitted electron, we have calculated the exchange integral $V^{\text{exch}}(R; l m_{Ar} m_c m_v \lambda \mu)$ with $\lambda = 0$ at a fixed internuclear distance $R = 3.5 a_0$ as a function of the energy ϵ of the emitted electron. The results are given in Table 1 and suggest that the integrals are smooth functions of the energy. The integrals vary about 30% from the highest to the lowest energy used in the calculation.

3.2 Angular momentum λ of free electron

The autoionization width $\Gamma(R; l \alpha J \Omega)$ in Eq. (8) contains a summation over the angular momentum quantum number λ of the free electron. Because the angular momenta of the bound electrons refer to different origins, angular momentum conservation cannot



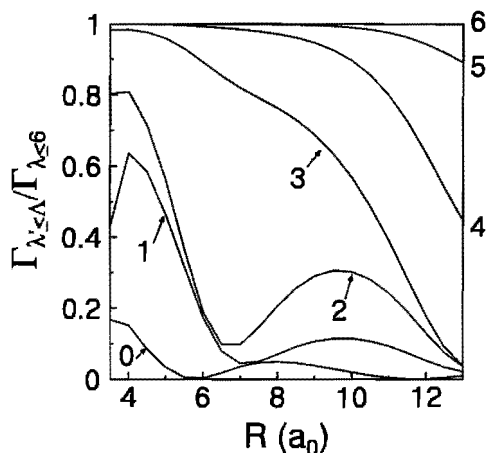


Figure 2: Accumulated contributions to the autoionization width $\Gamma_{\lambda \leq \Lambda}$ for the 3P_0 -state as a function of the maximum angular momentum quantum number Λ of the free electron. The results are scaled to the total ionization width $\Gamma_{\lambda \leq 6}$. The values of Λ are indicated in the graph.

be used to restrict λ to one specific value. Therefore, the summation over the quantum number λ ranges from 0 to infinity. However, an estimation of the upper limit Λ of this summation can be made. As an example we take the Ne(3s)-Ar system. The partial sums

$$\Gamma_{\lambda \leq \Lambda}(R) = \sum_{\lambda=0}^{\Lambda} \Gamma_{\lambda}(R), \quad (10)$$

are shown in Fig. 2 for the Ne(3P_0) state for individual λ -values. Here the contributions are normalized to the total ionization width with $\Lambda=6$. For small internuclear distances ($R < 7 a_0$), the $\lambda=6$ contribution is less than 1% of the total ionization width. This justifies the neglect of contributions for $\lambda > 6$. Driessen *et al.* neglect the contributions for $\lambda > 2$ to the total ionization width, which is obviously not correct. The contribution of larger λ -values is at least 30% of the total ionization width.

The $\lambda = 1$ contribution predominates for smaller internuclear distances ($R < 5 a_0$). The $\lambda = 2$ contribution is relatively small over the whole R -range. A large contribution for $\lambda = 3$ is found at $R = 7 a_0$. The contributions for larger λ -contributions shift to larger R -values and rapidly converge to zero.

To understand the R -dependence of the λ -contributions we have plotted in Fig. 3 the radial wave functions of the four electronic states appearing in the integrals of Eqs. (3) and (4) along the internuclear axis. In this one-dimensional simplification a schematic picture is given of the overlap of initial and final states for both electrons. In the case of the two bound state wave functions, $\Psi_{2p}^{Ne}(\mathbf{r})\Psi_{3p}^{Ar}(\mathbf{r})$, the dominant part of the product function is located between the two nuclei. On the other hand, the overlap $\Psi_{3s}^{Ne}(\mathbf{r})\Psi_{\lambda\mu}^{Ar}(\mathbf{r})$ is centered around the neon atom. The local symmetry at the neon site is mainly determined by the free electron wave function $\Psi_{\lambda\mu}^{Ar}$. In the case of even symmetry we expect a positive interference, and thus a large exchange integral. Conversely, for odd symmetry the positive and negative contributions will cancel and a small net value for the exchange integral is expected. Depending on the local phase of the free electron wave function $\Psi_{\lambda\mu}^{Ar}$ at the neon atom, these two extreme cases will occur. In Fig. 4 relative λ -contributions to the total ionization width are shown as function of

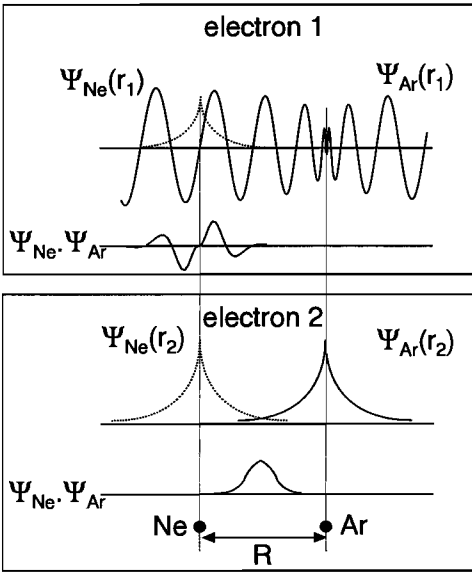


Figure 3: Schematic plot of the radial wave function products that contribute in the exchange integral. The notation $\Psi_X(r_i)$ is used, with r_i the position of electron i with respect to nucleus X . The upper panel shows the wave functions for electron one, the lower panel for electron two. The net contribution to the exchange integral results from the even part of the free electron wave function (Ψ_2).

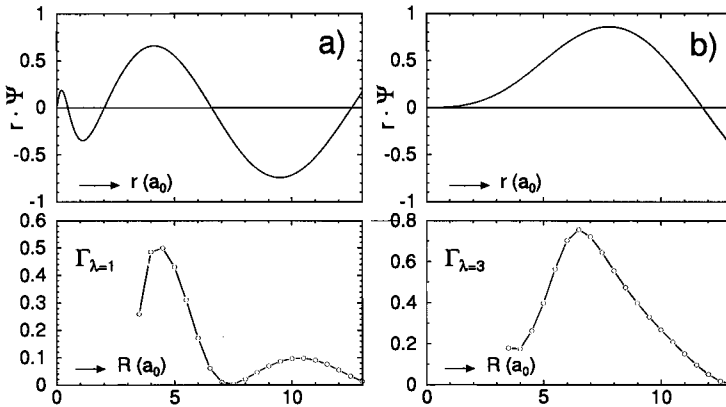


Figure 4: Relative contributions to the total autoionization width for a) $\lambda = 1$ and b) $\lambda = 3$. The upper panels show the free electron wave functions. There is a good correlation between the nodes and extrema in this function and in the λ -contribution.



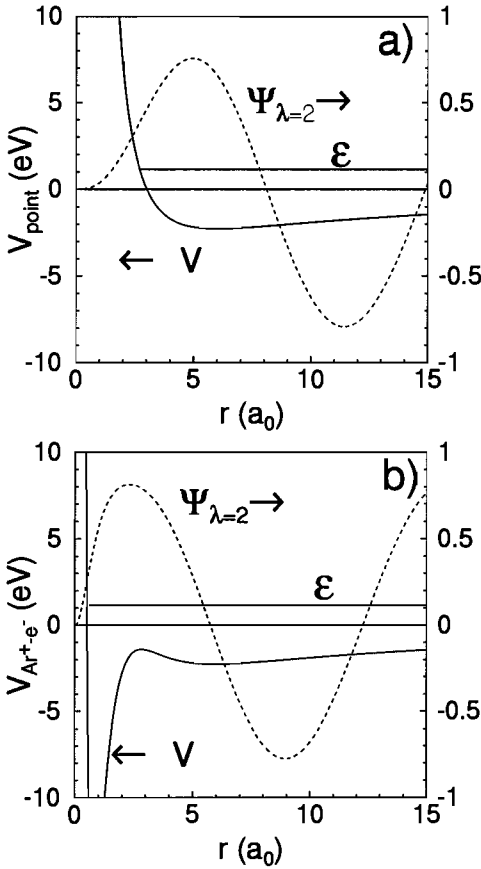


Figure 5: Free electron wave function with angular momentum quantum number $\lambda = 2$ (dotted curve) in a) a pure point charge Coulomb potential and b) in a screened $\text{Ar}^+\text{-e}^-$ -potential for a kinetic energy $\epsilon = 1.15\text{eV}$.

R together with the corresponding free electron wave function. We see that there is a strong correlation between the node structure of the free electron wave function and the calculated λ -contribution. The two maxima in the $\lambda = 1$ contribution correspond with the extrema of the wave function at $5 a_0$ and $10 a_0$, respectively. For $\lambda = 3$ a maximum at $8 a_0$ in the wave function corresponds with a maximum in the $\lambda = 3$ contribution to the total ionization width.

The phase of the free electron wave function at the position of the neon nucleus is extremely sensitive to a change in the $\text{Ar}^+\text{-e}^-$ potential. To illustrate this we show in Fig.5 the free electron wave function for $\lambda = 2$ in a pure point charge Coulomb potential and in the screened $\text{Ar}^+\text{-e}^-$ -potential. Due to the decreased screening at small internuclear distances the effective nuclear charge Z is larger than 1, resulting in a much deeper potential. Hence the classically forbidden region is smaller and the wave function starts oscillating at smaller R -values. This causes a phase shift of almost $\pi/2$. Due to its strong correlation with the free electron wave function, the R -dependence of the λ -contributions is also extremely sensitive to small changes in the screened potential. This is especially important when only a few λ -values contribute to the total ionization

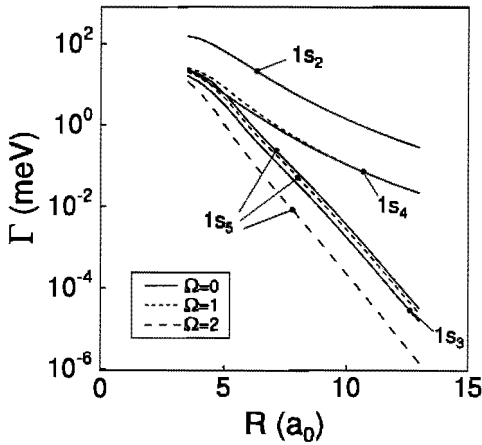


Figure 6: The autoionization width $\Gamma(R; \alpha_i^s \Omega)$ for the metastable Ne(3s)-states. Contributions for $\lambda > 6$ are neglected. The curves can be represented by the model function in Eq. 12 with parameters listed in Table 2.

width. When more λ -values contribute, their respective $\pi/2$ -phase shifts tend to average out this sensitivity for individual λ -contributions.

3.3 Results for Ne(3s)-Ar

In reality we have to deal with atomic states which are not pure LSJ -coupled states. The following mixing¹⁷ of the $J = 1$ singlet and triplet states has to be taken into account

$$\begin{aligned}
 |1s_2\rangle &= 0.265644|^3P_1\rangle + 0.964071|^1P_1\rangle, \\
 |1s_3\rangle &= |^3P_0\rangle, \\
 |1s_4\rangle &= 0.265644|^1P_1\rangle - 0.964071|^3P_1\rangle, \\
 |1s_5\rangle &= |^3P_2\rangle.
 \end{aligned}
 \tag{11}$$

In the following we will still use the LSJ -notation for the pure triplet states $1s_3$ and $1s_5$. The results for the autoionization width $\Gamma(R; \alpha J \Omega)$ for the atomic Ne(3s) states are shown in Fig. 6. Apparently, the structure in the single λ -contributions disappears in the final summation. The resulting curves are described in good approximation by the following model function

$$\Gamma_{\text{fit}}(R) = p_1 \exp\{-p_2 (R - 5 a_0)\} \exp\{p_3 \sin(p_4 R + p_5)\},
 \tag{12}$$

where parameters p_1, \dots, p_5 are determined in a least squares analysis. The sine function describes an oscillation around the exponential function. The parameters p_1, \dots, p_5 are listed in Table 2. The deviation of this model function from the actual ab initio results is less than 10%. Near $R = 3 a_0$ we find that the $\Gamma(R)$ curves start to level off due to saturation of overlap. This is comparable with the saturation introduced in the experimental curves of Verheijen *et al.* This effect is clearly not included in a satisfactory way in our model function. For the pure triplet states only the exchange mechanism contributes to the ionization width. Because the radiative mechanism is more effective, the ionization widths for the mixed states of Eq. (11) are much larger than for the pure triplet states.

Table 2: Parameters determined in a least squares analysis of the calculated autoionization width for the atomic states in the Ne(3s) multiplet. As a model function we use Eq. (12). For the pure triplet states, $1s_3=^3P_0$ and $1s_5=^3P_2$, the parameters p_3 , p_4 , and p_5 are equal to zero.

α	Ω	$\Gamma(5 a_0)$ (meV)	p_1 (meV)	p_2 (a_0^{-1})	p_3	p_4 (a_0^{-1})	p_5
1s ₂	0	62.842	49.614	0.675	0.259	0.643	-1.221
	1	63.353	50.010	0.676	0.262	0.639	-1.179
1s ₃	0	2.798	2.798	1.496			
1s ₄	0	5.885	5.948	0.724	0.509	0.423	1.045
	1	8.056	6.202	0.755	0.402	0.594	-0.539
1s ₅	0	4.865	4.865	1.468			
	1	3.927	3.927	1.478			
	2	0.977	0.977	1.687			

Bussert calculated the ionization rates for the different Ω -quantum numbers⁸ by making the assumption that these ionization rates can be expressed in a single reduced autoionization width. This resulted in a fixed ratio of the ionization rates for the different Ω -numbers independent of the internuclear distance. The following ratios for the Ω -components of the 3P_2 state have been obtained:

$$\Gamma(\Omega = 0) : \Gamma(\Omega = 1) : \Gamma(\Omega = 2) = 1 : 0.75 : 0.016.$$

In our calculation this ratio is R -dependent and at two different R -positions it is given by

$$\begin{aligned} \Gamma(\Omega = 0) : \Gamma(\Omega = 1) : \Gamma(\Omega = 2) &= 1 : 0.79 : 0.17 \quad \text{at } R = 5 a_0, \\ \Gamma(\Omega = 0) : \Gamma(\Omega = 1) : \Gamma(\Omega = 2) &= 1 : 0.77 : 0.07 \quad \text{at } R = 10 a_0. \end{aligned}$$

The ratio $\Gamma(\Omega = 0) : \Gamma(\Omega = 1)$ is in perfect agreement. For the $\Omega = 2$ state our calculation give relative much larger values.

In Fig. 7 the state-averaged autoionization width for a mixed beam ($^3P_0: ^3P_2=1:5$) is compared with fine structure averaged results of Gregor *et al.*,³ Verheijen *et al.*,⁴ and Baudon *et al.*² There is excellent agreement with the absolute values of Baudon *et al.* for small internuclear distances ($R < 6 a_0$), where ionization predominantly takes place. This results supports the excellent quality of the multiproperty analysis performed by Baudon *et al.* on differential elastic cross sections, ionization cross sections by Verheijen *et al.*⁴ and the ratio of Penning to associative ionization.

The results of Gregor *et al.* differ significantly, whereas the results of Verheijen *et al.* show a reasonable agreement. The correlation between the ionization widths determined in a multiproperty analysis and the simultaneously determined real part of the potential is very strong, as mentioned before. As a consequence, the ionization widths determined in such treatments have to be regarded with the accompanying real part of the potential. Generally, from a least squares analysis of the experimental data,

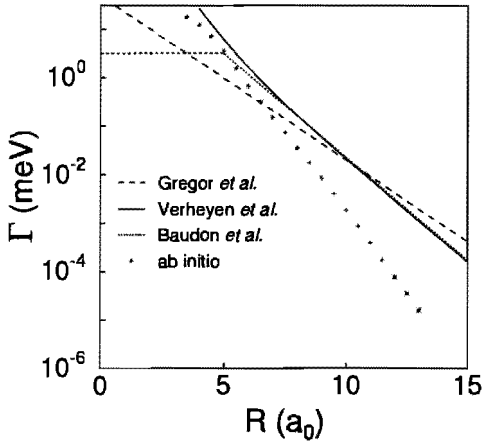


Figure 7: State averaged autoionization width for Ne(3s), compared with results of Verheyen *et al.*,⁴ Baudon *et al.*,² and Gregor *et al.*³

the exponential behavior of the ionization width cannot be determined very accurately. The absolute value of the ionization width can be determined only in the region where $\Gamma(R)$ is large and the particle velocity is small, *i.e.*, close to the classical turning point.

3.4 Results for Ne(3p)-Ar

The ionization widths for the Ne(3p)-multiplet have been calculated using Eq. (8). The relative λ -contributions to the total ionization width for the α_9 state are shown in Fig. 8, analogous to Fig. 2. Since the free electron has a larger energy (2.86 eV) compared to

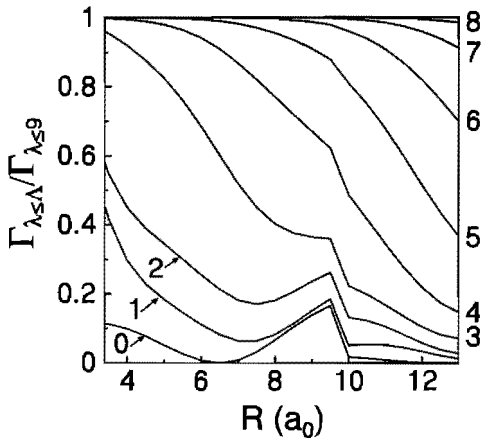


Figure 8: Accumulated contributions to the autoionization width $\Gamma_{\lambda \leq \Lambda}$ for the $|\alpha_9, \Omega = 0\rangle$ -state as a function of the maximum angular momentum quantum number Λ of the free electron. The results are scaled to the total ionization width $\Gamma_{\lambda \leq 9}$. The values of Λ are indicated in the graph.

the Ne(3s)-Ar ionization process (0.86 eV), more λ -quantum numbers contribute to the total ionization width. We find that contributions for $\lambda > 9$ rapidly converge to zero and can be neglected. For the pure Ne(3p, α_9) state ionization widths have been calculated by Driessen *et al.*. Contributions for $\lambda > 2$ were erroneously considered to be negligible, resulting in a large underestimation in the final results.

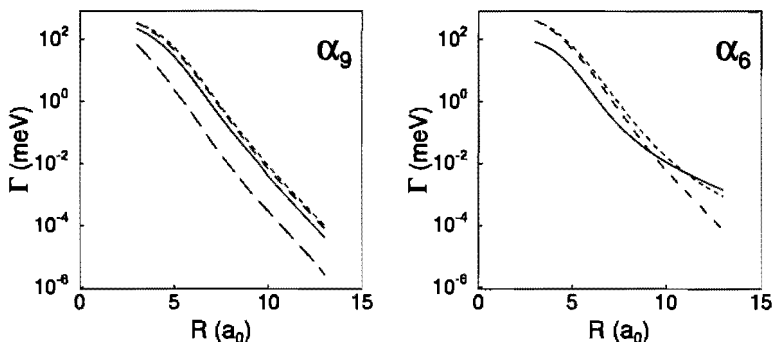


Figure 9: The autoionization width $\Gamma(R; \alpha_i^p \Omega)$ for two typical Ne(3p)-states. For the α_9 state only the exchange mechanism contributes to the ionization width. For the α_6 state both mechanisms contribute: for large values of R the radiative mechanism predominates.

For all states in the Ne(3p)-multiplet the ionization matrix elements are calculated as a function of the Ω -quantum number. The diagonal elements are the total autoionization widths and are presented in Fig. 9 for two typical states. The ionization widths are represented by the model function of Eq. (12) in a least squares fit and the parameters p_1, \dots, p_5 are listed in Table 3 for the Ne(3p) states.

The ionization widths for Ne(3p)-multiplet states have an average exponential decay with $p_2 \approx -1.65$ regardless of the Ω -quantum number. Only for the ionization curves with a large oscillatory structure, ($p_3 > 0.5$), the exponential decay is smaller. A pronounced tail can be observed for the singlet states (see α_6 state in Fig. 9). Note that for all Ne($3l, \alpha J \Omega$) states the largest autoionization width is found for the $\Omega = 1$ state in the range $R < 10 a_0$. The values of $\Gamma(R; l \alpha J \Omega)$ at $R = 5 a_0$ in Table 3 show that the ratio of the ionization width for different Ω quantum numbers varies considerably in magnitude for the different states. For the $\alpha_{8,10}$ states this polarization effect is close to one, whereas the polarization effect $\Gamma(\Omega = 0)/\Gamma(\Omega = 1)$ for the $\alpha_{6,7}$ states is quite large.

4 Coupled channels calculation with optical potentials

4.1 Semiclassical approach

Before discussing the coupled channels model we briefly review the semiclassical approach for calculating ionization cross sections. The total ionization widths serve as input for a simple semiclassical calculation, which is based on the opacity function. The total ionization probability $f_{\text{ion}}(b)$ is obtained as a function of the impact parameter b

$$f_{\text{ion}}(b) = 1 - \exp\left(-2 \int_{R_t}^{\infty} \frac{\Gamma(R)}{\hbar v_{\text{rad}}(R; b)} dR\right), \quad (13)$$

Table 3: Parameters of the model function of Eq. (12) determined in a least squares analysis of the calculated autoionization width for all atomic states α_i in the Ne(3p) multiplet.

i	Ω	$\Gamma(5 a_0)$ (meV)	p_1 (meV)	p_2 (a_0^{-1})	p_3	p_4 (a_0^{-1})	p_5
1	0	6.151	3.638	1.116	2.018	0.453	0.613
2	0	31.150	22.547	1.671	0.413	0.841	2.975
	1	54.791	41.342	1.672	0.402	0.898	2.569
3	0	31.440	18.858	1.604	0.545	0.723	-2.402
4	0	40.840	17.279	1.316	0.873	0.663	-1.573
	1	67.935	33.523	1.418	0.712	0.675	-1.933
	2	17.977	12.580	1.685	0.393	0.844	-3.082
5	0	36.172	28.191	1.670	0.398	0.898	2.470
	1	42.355	30.214	1.645	0.414	0.798	-3.036
6	0	11.087	5.523	1.151	0.831	0.691	-1.306
	1	57.127	27.426	1.350	0.734	0.670	-1.797
	2	41.725	28.981	1.630	0.435	0.771	-2.860
7	0	8.784	6.883	1.620	0.287	0.714	-2.554
	1	51.394	38.606	1.636	0.412	0.843	2.838
8	0	34.716	14.900	1.306	0.855	0.644	-1.503
	1	30.677	14.798	1.354	0.729	0.647	-1.643
	2	24.319	7.643	1.344	1.180	0.442	-0.443
9	0	22.573	18.280	1.652	0.312	0.857	2.739
	1	42.351	33.451	1.632	0.396	0.889	2.479
	2	38.260	29.785	1.628	0.408	0.833	2.779
	3	2.482	1.872	1.728	0.325	0.735	-1.585
10	0	7.038	5.322	1.679	0.364	1.422	1.440
	1	7.471	5.672	1.679	0.342	1.441	1.282



where R_t denotes the classical turning point and $v_{\text{rad}}(R; b)$ the radial velocity. The total cross section for ionization is now determined by integrating over the impact parameter:

$$Q_{\text{ion}} = 2\pi \int_0^{\infty} f_{\text{ion}}(b) b db. \quad (14)$$

The rotation of the internuclear axis R during the collision scrambles the Ω -distribution. When a straight line trajectory is assumed, this scrambling can be incorporated through a superposition of ionization widths, with squared Wigner- d functions as a weighting factor

$$\Gamma(R; \alpha J M_J) = \sum_{M'_J} |d_{M_J, M'_J}^J(\beta)|^2 \Gamma(R; \alpha J |M'_J|), \quad (15)$$

and where $\beta = \arcsin(b/R)$ the angle between the asymptotic relative velocity and the internuclear axis.

In case of the Ne(3p)-multiplet couplings between the fine structure states have to be taken into account which are difficult to incorporate in this semiclassical model. A quantum mechanical description is more suitable for the Ne(3p)-Ar system. However, the semiclassical model can be used for test purposes.

4.2 Coupled channels calculation

In the coupled channels model¹⁶ the wave functions $\Psi(r, R)$ are expanded in an orthonormal basis of channel functions: $\Psi(r, R) = \sum_i \frac{F_i(R)}{R} \varphi_i(r, R)$. For the Ne(3p)-Ar system this basis is a set of 23 channel functions, the so-called N -diabatic channel functions given by

$$|\varphi_i\rangle^N = |\pi \alpha J N P M_P\rangle, \quad (16)$$

where N is the rotational angular momentum quantum number of the nuclear motion and $P = N + J$ is the total angular momentum with M_P its projection on the laboratory z -axis. The states have a well-defined parity π . Solving the Schrödinger equation in this basis results in the S -matrix. The squares of the matrix elements $|S_{\alpha_f N_f, \alpha_i N_i}|^2$ give the probability for a transition from state $|\alpha_i N_i\rangle$ to a $|\alpha_f N_f\rangle$ state which is expressed in the cross section $Q_{i \rightarrow f}$. The unitarity of the S -matrix reflects the conservation of flux.

To incorporate ionization in the coupled channels calculation, a flux-dissipative term should be added to the Hamiltonian of the Schrödinger equation. This is realized by adding an imaginary part to the real-valued potential, resulting in the optical potential of Eq. (1). Analogous to Eq. (8), a matrix representation of the autoionization width is constructed in the N -diabatic basis:

$$\begin{aligned} \Gamma_{ij}(R; l \alpha J |M_P|) = & \\ & \sum_{\lambda} \frac{2\pi}{\hbar} \left\{ \frac{m_e}{\hbar q(R)} \sum_{J_I \Omega_I \mu m_s} V(R; l \alpha_i |M_P| \rightarrow J_I \Omega_I \lambda \mu m_s) \right. \\ & \left. \times V(R; l \alpha_j |M_P| \rightarrow J_I \Omega_I \lambda \mu m_s) \right\}, \end{aligned} \quad (17)$$

with i and j referring to two states in the N -diabatic basis. The non-diagonal elements cause an additional coupling of different states within an Ω -class. Thus, ionization not

only results in a loss of flux, but also affects the transition probability for intramultiplet mixing.

4.3 Complex potential in coupled channels calculation

We implemented the complex potential in the existing code of the coupled channels program. A number of specific routines have been extended for complex numbers. The most trivial test is to run the new program for a real potential, *i.e.*, with the imaginary part set to zero. This results in the same S -matrix elements compared to the results of the unaltered code.

To investigate the influence of the imaginary part of the optical potential on the integration methods in the CC program we use simple perturbation theory. The molecular Ne^+ -Ar interaction is represented by model potentials for the σ and π orientation of the (3p) valence electron. The relative nuclear motion is governed by the isotropic part $V_0 = \frac{1}{3}(V_\sigma + 2V_\pi)$ that does not exert a torque on the individual nuclei and, therefore, does not induce transitions between the fine structure states. On the other hand, the anisotropic part $V_1 = V_\sigma - V_\pi$ causes a torque on the molecular system and is responsible for the mixing of the individual states in the (3p)-multiplet. Therefore, as a test we use the following optical potential

$$V_{\text{opt}} = V_0 + p e^{i\alpha} V_1. \quad (18)$$

Because the Schrödinger equation is a linear equation the same factor $p e^{i\alpha}$ should appear in the off-diagonal elements of the S matrix for small p -values. This allows for a more rigorous test of the new coupled channels code. When taking the value p small enough we find the off-diagonal S -matrix elements to scale linearly with $p e^{i\alpha}$. This suggest strongly that the integration routine and the accompanying subroutines are correctly modified for the optical potential.

4.4 Ionization cross sections in coupled channels calculation

Due to the introduction of a complex potential, the S -matrix is no longer a unitary matrix. The deviation from unity of the norm of each column can be interpreted as a loss of flux due to ionization. Thus the ionization probability $f_{\text{ion}}(P)$ is given by

$$f_{\text{ion}}(\alpha_i, P) = 1 - \sum_f |S_{\alpha_f N_f, \alpha_i N_i}(P)|^2, \quad (19)$$

with P being the total angular momentum quantum number. The summation over f implies the summation over all diabatic channels indicated with $|\alpha_f N_f\rangle$. In a quantum mechanical equivalent of Eq. (14) we find for the total ionization cross section of a state $|\alpha_i\rangle$

$$Q_{\text{ion}}(\alpha_i) = \frac{\pi}{k_i^2} \sum_P (2P+1) f_{\text{ion}}(\alpha_i, P), \quad (20)$$

For the polarized atom ionization cross section $Q_{\text{ion}}^{|M_J|}(\alpha_i)$ for an $\text{Ne}(3p, \alpha_i |M_J\rangle)$ initial state we find in analogy to the cross section for intramultiplet mixing¹⁶

$$Q_{\text{ion}}^{|M_J|}(\alpha_i) = \frac{\pi}{k_i^2} \sum_P (2P+1) f_{\text{ion}}^{|M_J|}(\alpha_i, P). \quad (21)$$



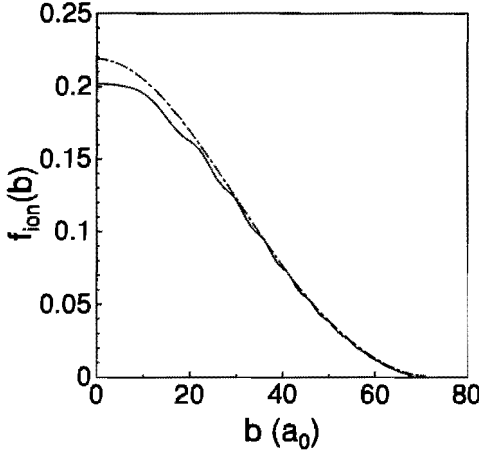


Figure 10: Ionization probability $f_{\text{ion}}(b)$ as a function of the impact parameter b calculated with the coupled channels model (solid curve) and the semiclassical model (dashed curve).

Here, the ionization probability is given by

$$f_{\text{ion}}^{|M_J|}(\alpha_i P) = 1 - \sum_f \sum_{N_f} \sum_{N_i} \sum_{N_{i'}} i^{N_i - N_{i'}} \times (J_i |M_J| P M_P |N_i 0)(J_i |M_J| P M_P |N_{i'} 0) S_{\alpha_f N_f, \alpha_i N_i} S_{\alpha_f N_f, \alpha_{i'} N_{i'}}^* \quad (22)$$

Of course, the total ionization cross section $Q_{\text{ion}}(\alpha_i)$ follows directly from the averaged polarized ionization cross sections

$$Q_{\text{ion}}(\alpha_i) = \frac{1}{2J+1} \sum_{M_J=-J}^J Q_{\text{ion}}^{|M_J|}(\alpha_i). \quad (23)$$

4.5 Performance coupled channels calculation versus semiclassical approach

A comparison of semiclassically calculated cross sections and those calculated with the coupled channels code forms a direct test for the validity of the expressions in the previous sections. We take the same optical potential as input for both approaches: the real part equal to the potential of Gregor *et al.* and an exponential function as the imaginary part, *i.e.*, the ionization width.

We expect the the discrepancy between the two approaches to be maximal for small kinetic energies. In this test we use a kinetic energy of $E = 20$ meV. The resulting ionization probabilities of the two methods are depicted in Fig. 10. For small impact parameters we see a discrepancy of approximately 10%. However, for larger impact parameter both methods result in exactly the same ionization probability. Semiclassically, the integrand in Eq. (13) has an integrable singularity at the classical turning point where the radial velocity is zero. In the quantum mechanical method the radial wave function near the turning point behaves like an Airy function and an exact treatment is possible. The effective potential shows for small impact parameters a step behavior (typically $1/R^{14}$) close to the turning point. For larger impact parameters the

Table 4: Partial ionization cross sections $\Delta Q_{\text{ion}}[R_1, R_2]$ for Ne(3s)+Ar at a kinetic energy of $E = 20$ meV calculated with a coupled channels model (CCC) and a semiclassical model (SC). Ionization is only taken into account in the region $R_1 \leq R \leq R_2$ as indicated, with the classical turning point located at $R_t = 7 a_0$. For comparison the total ionization cross section $Q_{\text{ion}} \equiv \Delta Q_{\text{ion}}[0, 15]$ is also indicated.

range $[R_1, R_2]$ (a_0)	$\Delta Q_{\text{ion}}^{\text{CCC}}$ (\AA^2)	$\Delta Q_{\text{ion}}^{\text{SC}}$ (\AA^2)
[7.1, 7.2]	0.603	0.433
[7.2, 7.3]	0.644	0.560
[7.3, 7.4]	0.636	0.639
[0, 15]	7.34	7.69

slope of the effective potential tends to a $1/R^2$ behavior of the centrifugal potential for which the discrepancy in the results of both methods becomes smaller. The behavior of the integral near the turning point is investigated by taking the imaginary part of the potential equal to zero except for a small range $\delta R = 0.1 a_0$ at different internuclear distances. In Table 4 we see a large discrepancy in the region close to the turning point $R_t = 7 a_0$. Clearly, the semiclassical approximation results in too large contributions to the ionization probability, which explains the difference between the two methods.

5 Cross sections for Ne(3p)-Ar

5.1 Ionization cross sections

The autoionization widths of Eq. (17) serve as input for the imaginary part of the optical potential in the coupled channels calculation. The real part of the optical potentials is given by the adiabatic molecular Ne(3p)-Ar potentials, which are obtained by diagonalizing the molecular interaction Hamiltonian as described by Hennecart.²¹ In our calculation the model potentials $V_\sigma(R)$ and $V_\pi(R)$ of Bussert⁸ are used as input, where σ and π refer to the orientation of the 3p-valence electron. The resulting adiabatic potential curves are shown in Fig. 11. Note that the curves for the upper five states $\alpha_1, \dots, \alpha_5$ clearly have a repulsive character, whereas the curves for $\alpha_6, \dots, \alpha_{10}$ show an attractive character. The avoided crossings in the adiabatic potential curves agree reasonably with those in the adiabatic potentials calculated by Kucal *et al.*,²² who use slightly different V_σ and V_π potentials as input.

The coupled channels calculation results in an S -matrix from which the ionization probability can be derived through Eq. (21). In Fig. 12 the ionization probabilities for the $|\alpha_9, J = 3 |M_J\rangle$ magnetic substates with a collision energy $E=130$ meV are depicted as a function of the impact parameter. The probability is constant with a sharp cut off at an impact parameter $b \approx 6 a_0$, corresponding with an angular momentum $P = 75$. Opacity functions calculated in a semiclassical analysis^{8,9} show the same behavior. In the semiclassical calculations the ionization probabilities are slightly larger than the results of the coupled channels calculation.



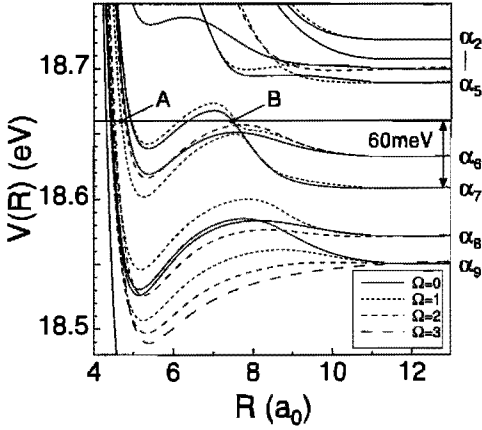


Figure 11: Adiabatic potentials for the $\text{Ne}(3p)+\text{Ar}$ system for the $\alpha_2, \dots, \alpha_9$ states. Asymptotically the atomic states are degenerate for the different Ω -quantum numbers. This degeneracy is cancelled for smaller internuclear distances. A shoulder in the $(\alpha_7, \Omega = 0)$ -potential prevents a 60 meV kinetic energy collision to probe the inner region of the potential. Position *A* and *B* indicate the different turning points for $\Omega = 0, 1$.

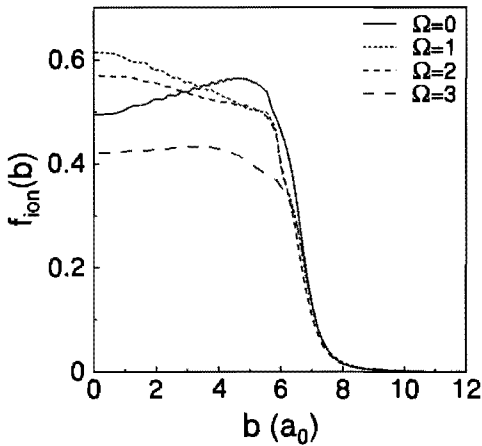


Figure 12: Ionization probability as a function of the impact parameter for the $|\alpha_9, J=3\rangle$ magnetic substates.

Table 5: Calculated ionization cross sections Q_{ion} for the Ne(3p)-multiplet compared with experimental results of Bussert at a collision energy $\langle E \rangle = 60$ meV. As a reference for the absolute value of Q_{ion} we give the average ionization width in the classical turning point R_t for the $\Omega = 0$ potential at $b = 0$.

state	optical potential		$Q_{\text{ion}}^{\text{CCC}}(\Omega)$ (\AA^2)				$\langle Q \rangle$ (\AA^2)	
	R_t (a_0)	$\Gamma(R_t)$ (meV)	$ M_J =0$	$ M_J =1$	$ M_J =2$	$ M_J =3$	CCC	expt. ^{a)}
α_1	7.6	0.39	1.20				1.20	
α_2	8.2	0.18	2.64	3.32			3.09	<0.9
α_3	8.4	0.13	11.95				11.95	
α_4	7.5	2.35	9.18	6.98	6.58		7.26	6.3
α_5	7.0	1.45	4.45	6.22			5.63	3.7
α_6	4.8	67.24	21.48	21.97	24.32		22.81	25.6
α_7	7.4	0.77	3.83	6.50			5.63	15.6
α_8	4.5	48.25	22.69	27.53	26.00		25.95	33.0
α_9	4.4	63.54	31.42	27.75	26.91	25.14	15.65	22.4
α_{10}	4.7	11.82						

a) Experimental values of Bussert *et al.*⁸

For all Ne(3p) states the ionization cross sections have been calculated with a collision energy of 60 meV. These results are shown in Table 5 together with experimental data of Bussert,⁸ obtained in a high resolution electron spectroscopy experiment. The relative scaling of the experimental cross sections is accurate within 10%, but the systematic error in the absolute value is rather large (50%).⁸ To compare the experimental data with our calculated results both sets are plotted in Fig. 13. The agreement of our calculated cross sections with the experimental values is good.

The ionization cross section is determined to a large extent by the magnitude of the autoionization width at the position of the turning point. This is demonstrated in Table 5 where we list both the turning point and the corresponding value of the autoionization width. If the turning point is located at large R -values, the corresponding ionization cross section is small. For a collision energy of 60 meV the rather large shoulder in the $(\alpha_7, |M_J| = 0)$ potential prevents the collision system to probe small internuclear distances as depicted in Fig. 11. Taking a slightly larger kinetic energy $E=80$ meV, the averaged ionization cross section increases drastically to a value of $Q_{\text{ion}}(\alpha_7, |M_J| = 0) = 8.53 \text{ \AA}^2$. This partly explains the discrepancy for the α_7 state.

Driessen *et al.* have measured the polarized ionization cross section for the Ne(3p)-Ar system in the thermal energy range (80-150 meV) and in the superthermal energy range (0.8-3 eV) as a function of the collision energy. In Table 6 these experimental data are compared with corresponding calculations. Again the calculated cross sections are in good agreement. However, the CCC results decrease more rapidly with increasing energy. This indicates a repulsive branch of the real part of the potential which is too



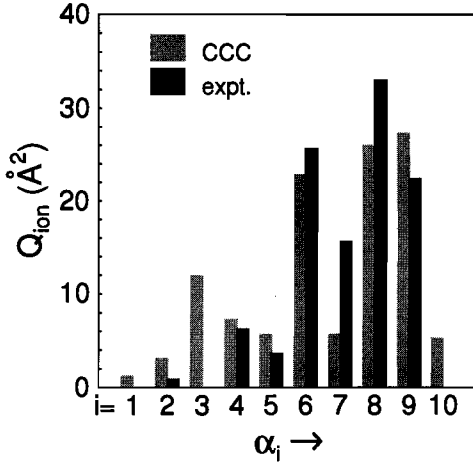


Figure 13: Ionization cross sections calculated with the coupled channels code using the proposed optical potential for the states of the Ne(3p) multiplet (CCC) compared with the experimental data of Bussert (expt.).

Table 6: Calculated energy-dependent ionization cross sections $Q_{\text{ion}}^{\text{CCC}}$ for the Ne(3p; α_9)-state, compared with experimental results of Driessen

$E(\text{eV})$	$Q (\text{Å}^2)^{\text{a)}$	$Q_{\text{ion}}^{\text{CCC}} (\text{Å}^2)$
0.08	25	23.8
0.09	24	22.6
0.10	24	21.5
0.13	23	20.0
0.20	22	15.7
1.70	19	12.9

^{a)} Driessen *et al.*⁹

hard.

5.2 Intramultiplet mixing

Accurate experimental cross sections for intramultiplet mixing have been obtained in our group²⁴ for the Ne(3p)-Ar system in a superthermal energy range with $\langle E \rangle \approx 1.7\text{eV}$. The experimental results are listed in Table 7. The systematic error in these measurements is less than 22%.²³ Therefore, these data form an ideal testcase for studying the influence of ionization on the intramultiplet mixing process.

The off-diagonal ionization matrix elements of Eq. (17) cause an additional coupling between the Ne(3p) states. Together with the loss of flux the intramultiplet mixing process will be affected by the autoionization width. In Table 7 we compare calculated cross sections with the experimental data. For most transitions the measured cross sections agree well with the calculated ones. Only for the $\alpha_7 \rightarrow \alpha_6$, $\alpha_9 \rightarrow \alpha_6$, and $\alpha_9 \rightarrow \alpha_7$ transitions we observe a discrepancy of a factor of three. Such a discrepancy was also

Table 7: Intramultiplet mixing cross sections for the Ne(3p)+Ar system calculated with a complex potential (CCC) and a real potential with $\Gamma = 0$, compared with experimental results at an average collision energy $E = 1.7\text{eV}$ for the $\alpha_i \rightarrow \alpha_f$ -transitions. The polarization effect $Q^{|0|}/Q^{|1|}$ is indicated.

i	f	$\langle Q \rangle (\text{\AA}^2)$			$Q^{ 0 }/Q^{ 1 }$		
		expt. ^{a)}	CCC	$\Gamma = 0$	expt	CCC	$\Gamma = 0$
5	3	0.4	0.1	(0.1)	0.2	0.0	(0.0)
	4	11.2	7.7	(15.3)	0.9	0.9	(0.7)
	6	4.7	3.5	(6.9)	0.7	0.5	(0.4)
	7	1.6	2.8	(3.9)	1.1	2.1	(1.8)
	8	1.4	1.2	(1.8)	1.2	1.6	(2.1)
	9	1.5	1.3	(2.0)	2.3	2.2	(2.1)
7	4	1.7	2.9	(4.3)	0.6	0.4	(0.6)
	5	1.4	2.6	(3.7)	2.3	3.6	(2.2)
	6	4.9	14.3	(16.2)	0.9	0.9	(0.9)
9	4	0.3	0.8	(0.9)			
	5	0.3	0.5	(0.8)			
	6	0.4	1.2	(1.6)			
	7	1.4	4.9	(6.7)			
	8	10.3	16.2	(19.0)			
	10	0.1	0.2	(0.4)			

^{a)} Systematic error in absolute value 22%, Boom *et al.*²³



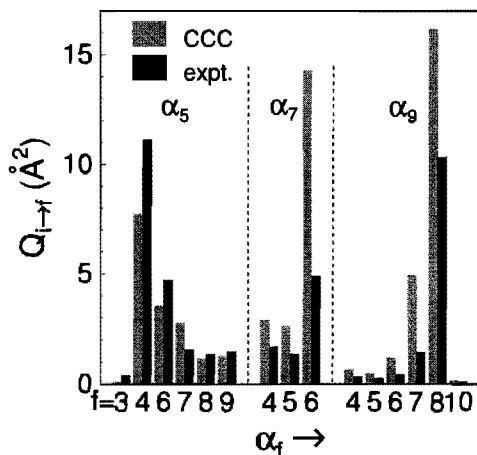


Figure 14: Magnetic substate averaged intramultiplet mixing cross sections calculated with the coupled channels code for transitions with α_5 , α_7 and α_9 initial states (CCC), in comparison to experimental data. The final states are indicated by their Paschen number under the bars.

observed for the Ne(3p)-He system, where no ionization takes place. This discrepancy in the superthermal energy regime was attributed to the incorrect long range description of the potentials.²⁵ Especially transitions with a small energy splitting, such as the $\alpha_7 \rightarrow \alpha_6$, are sensitive for the long range behavior of the potential. The comparison between calculated and experimental averaged cross sections is demonstrated in Fig. 14. The experimental and calculated polarization effects $Q_{i \rightarrow f}^{M=0} / Q_{i \rightarrow f}^{M=1}$ are in good agreement for all $J = 1$ states in Table 7, regardless of the (dis)agreement in absolute values. A good agreement of the polarization effect was also observed in high energy measurements on intramultiplet mixing in the Ne(3p)-He system.²³ This shows that the polarization effect is rather robust for errors in the absolute values.

The effect of ionization on the intramultiplet mixing cross sections is elucidated in Fig. 15. For impact parameters $b < 6 a_0$ the ionization probability is large. Therefore, the $dQ_{i \rightarrow f} / db$ contribution becomes negligible for these impact parameters. Especially for transitions where the intramultiplet mixing cross section mainly stems from small impact parameter collisions the influence of ionization is significant. For some transitions the ionization reduces the cross sections for intramultiplet mixing by more than a factor of two as shown in Table 7. For other transitions the effect of ionization is negligible. In the case of the $\alpha_9 \rightarrow \alpha_8$ -transition the contribution to the intramultiplet mixing cross sections originates from large impact parameter collisions and ionization has a negligible effect. Because the cross sections $Q_{i \rightarrow f}^{M_J}$ of the different magnetic substates have almost the same relative impact parameter dependency, the polarization effect is not very sensitive to ionization. This is reflected in the values of the polarization effect in Table 7.

6 Cross sections for Ne(3s)-Ar

In a multiproperty analysis both the real and the imaginary part of the potential are simultaneously determined. In the case of Verheyen *et al.* these potentials describe the experimental value cross sections for ionization in a broad energy range. In our

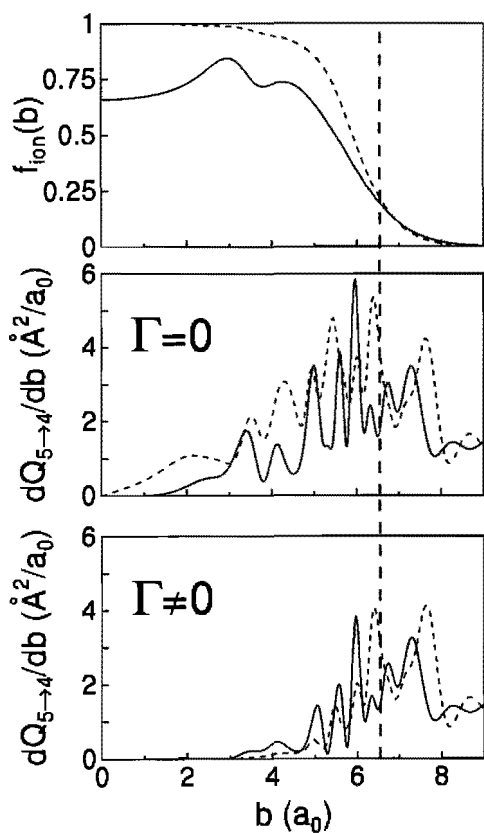


Figure 15: Effect of ionization on intramultiplet mixing cross section as a function of the impact parameter b . Upper panel: ionization probability, middle panel: cross section without ionization, lower panel: cross section with ionization. Here the solid curves represents the $|M_J| = 0$ state and the dashed curve the $|M_J| = 1$ state. The vertical dashed line indicates the region where ionization influences the intramultiplet mixing process.



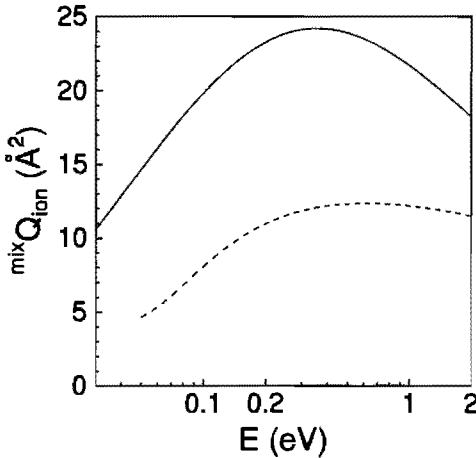


Figure 16: Ionization cross sections calculated with a semiclassical model for a mixed beam (dashed line) compared with experimental data of Verheyen *et al.*⁴ (solid line).

case, however, it is difficult to make a good estimate for the real part of the potential and combine it with our calculated ionization widths in order to calculate ionization cross sections. In this example we use the real-part of the potential as given by Gregor *et al.*³ The resulting semiclassical cross section for a mixed Ne-beam is depicted in Fig. 16 as a function of the collision energy in energy range $E=0.05\text{--}2$ eV together with the experimental data of Verheyen *et al.* The calculated cross sections are more than a factor two too small. A minor adjustment of the real potential by shifting the classical turning point to smaller R -values increases the ionization probability. Due to the exponential decay of the ionization width only a small shift of the repulsive part of the real-valued potential is sufficient for compensating the discrepancy. We can estimate that a shift $\delta R = -0.5 a_0$ is sufficient to increase the ionization cross sections in our calculation by a factor two.

6.1 Initial state fine structure

As shown in Fig. 16 the experimental cross section for the 3P_0 state is 20% larger than the 3P_2 cross section for thermal energies. This increases up to 50% in the superthermal collision energy range. The ratio $Q_{\text{ion}}(^3P_0)/Q_{\text{ion}}(^3P_2)$ is discussed separately from the overall discrepancy mentioned above. The experimental ratio is shown in Fig. 17. Obviously, the calculated ratio is much too small compared to the experimental data. In the remainder of this section we discuss a possible mechanism to explain the discrepancy between the calculated and experimental ratios of the 3P_0 and 3P_2 ionization cross sections.

Because the radiative mechanism is more effective, the singlet states ionize a factor 20 more efficiently than the triplet states. This also reflects in the lifetimes of the singlet 1P_1 and the triplet 3P_2 state which are 1.5 ns and 20 ns, respectively.²⁶ Therefore, a small admixture of singlet states will increase the ionization widths of the triplet states significantly. To investigate this effect we propose the following admixture:

$$|1s_3\rangle' = \left\{ |^3P_0\rangle + \gamma|^1P_1\rangle \right\} / \sqrt{1 + \gamma^2}. \quad (24)$$

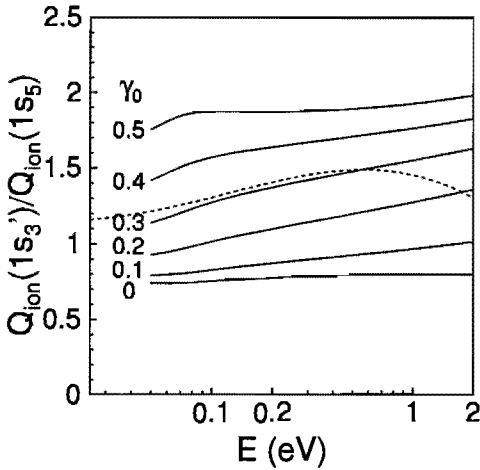


Figure 17: The ratio $Q_{\text{ion}}(1s_3')/Q_{\text{ion}}(1s_5)$ for a mixed $|1s_3'\rangle = (|{}^3P_0\rangle + \gamma|{}^1P_1\rangle)/\sqrt{1+\gamma^2}$ state. The R -dependent mixing parameter $\gamma(R)$ is given by Eq. (25). Results for different values of γ_0 are shown. The dashed line depicts the experimentally observed ratio by Verheijen *et al.*

We assume that the interaction that causes the mixing behaves like the induced-dipole force, which has a R^{-4} behavior resulting in

$$\gamma(R) = \gamma_0(R/R_{\text{ref}})^{-4}, \quad (25)$$

with γ_0 the value at the reference distance $R_{\text{ref}} = 5 a_0$. Using the semiclassical model of Section 4.1 we calculate the ionization cross section for several values of γ_0 . The ratio of the ionization cross sections of the mixed $|1s_3'\rangle$ state and the $|1s_5\rangle$ state is shown in Fig. 17 as a function of the parameter γ_0 . Compared with the experimental ratio of Verheijen *et al.* a reasonable agreement can be obtained for $0.3 < \gamma_0 < 0.4$. Whether such large admixing coefficients are realistic, needs to be studied in the future.

Alternatively, one may introduce state dependent real potentials. This allows the $|1s_3\rangle$ state to probe smaller internuclear distances compared to the $|1s_5\rangle$ state and hence the ionization for the $|1s_3\rangle$ state increases. Verheijen *et al.* used in their analysis a state-dependent repulsive branch to get better agreement for higher collision energies.

6.2 Final state fine structure analysis

To obtain information on the ratio of the $\text{Ar}^+({}^2P_{1/2})$ and $\text{Ar}^+({}^2P_{3/2})$ final states we rewrite the autoionization width of Eq. (8) as $\Gamma(R; l\alpha J\Omega) = \sum_{J_I} \Gamma(R; l\alpha J\Omega \rightarrow J_I)$. The probability for ending up in an $\text{Ar}^+({}^2P_{J_I})$ state is given by the following ratio:

$$W(R; l\alpha J\Omega) = \Gamma(R; l\alpha J\Omega \rightarrow J_I = 3/2) / \Gamma(R; l\alpha J\Omega \rightarrow J_I = 1/2). \quad (26)$$

This ratio has been calculated and is shown in Fig. 18 for the 3P_0 state and for the Ω -averaged 3P_2 state. The ratio $W(R; {}^3P_0)$ has a pronounced R -dependence in contrast with the 3P_2 state, which is almost R -independent. Considering the R -range where ionization occurs, only the ratios for $R < 7 a_0$ are of importance. Experimentally, we cannot obtain R -dependent data. Instead, the ratio of the ionization cross sections has

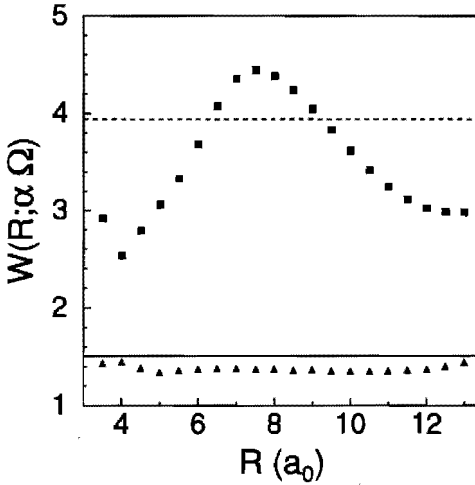


Figure 18: The ratio of the fine structure depending autoionization width $W(R; \alpha \Omega)$ for the 3P_0 -state (square markers) and for the Ω -averaged 3P_2 -state (triangle markers). The ratios are compared with experimentally determined ratios for the 3P_0 -state (dashed line) and for the Ω -averaged 3P_2 -state (solid line).

been determined for a collision energy $E=60 \text{ meV}^{27}$ by analyzing the electron energy spectrum results in

$$\begin{aligned} Q_{{}^3P_{0;3/2}} / Q_{{}^3P_{0;1/2}} &= 3.94(14), \\ Q_{{}^3P_{2;3/2}} / Q_{{}^3P_{2;1/2}} &= 1.51(7). \end{aligned} \quad (27)$$

These values are plotted in Fig. 18 and show a remarkable agreement in the R -range ($R < 7 a_0$) important for ionization. This ratio mainly depends on the ionization widths. The good agreement strongly suggest that the real part of the potentials for the Ne(3s)-Ar system needs to be adjusted in cases of disagreement, as discussed in the previous section.

7 Concluding remarks

We have performed ab initio calculations for the autoionization width of the Ne(3s)-Ar and Ne(3p)-Ar systems. In case of the Ne(3p)-Ar system we have used these autoionization widths together with ab initio data for the real part of the potential as input for a coupled channels calculation. The good agreement between experiment and theory for both the ionization cross sections and the intramultiplet mixing cross sections demonstrates that our calculated ionization widths have been determined with correct absolute scaling. Moreover, the good agreement in the cross sections for intramultiplet mixing shows that the coupled channels model describes the features of ionizing collisions in a very satisfactory way.

For the Ne(3s)-Ar system the agreement with experimental ionization cross sections is less striking. Two effects may be accountable for this. First, the semiclassical model is not as accurate as a complete coupled channels approach. Second, and more important, the real part of the potentials has been determined from experimental data in a multiproperty analysis and is therefore interdependent with the imaginary part.

This interdependency is cancelled when we study the ratio $Q({}^2P_{1/2})/Q({}^2P_{3/2})$ which

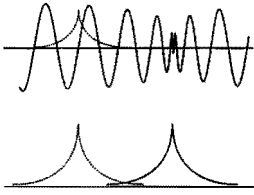
mainly depends on the ionization widths related to these final fine structure states. The ratio is in good agreement with calculated ratios based upon our ab initio ionization widths. In our opinion, this implies that the real part of the potential is not correctly determined and need to be adjusted.

References

- [1] P. Siska, *Rev. Rev. Mod. Phys.* **65**, 337 (1993), and references cited herein.
- [2] J. Baudon, P. Feron, C. Miniatura, F. Peales, J. Reinhardt, J. Robert, H. Haberland, B. Brunetti, and F. Vecchiocattivi, *J. Chem. Phys.* **95**, 1801 (1991).
- [3] R. Gregor and P. Siska, *J. Chem. Phys.* **74**, 1078 (1981).
- [4] M. Verheijen and H. Beijerinck, *Chem. Phys.* **102**, 255 (1986).
- [5] J. Driessen, S. Op de Beek, L. Somers, H. Beijerinck, and B. Verhaar, *Phys. Rev. A* **44**, 167 (1991).
- [6] S. Op de Beek, J. Driessen, H. Beijerinck, and B. Verhaar, *J. Chem. Phys.* (1996), chapter 5 of this thesis, submitted for publication.
- [7] W. Bussert, T. Bregel, R. Allan, M.-W. Ruf, and H. Hotop, *Z. Phys. A* **320**, 105 (1985).
- [8] W. Bussert, Ph.D. thesis, Universität Kaiserslautern, Germany, 1985, unpublished.
- [9] J. Driessen, F. van de Weijer, M. Zonneveld, L. Somers, M. Janssens, H. Beijerinck, and B. Verhaar, *Phys. Rev. A* **42**, 4058 (1990).
- [10] J. Gardner, R. Cline, J. Miller, D. Heinzen, H. Boesten, and B. Verhaar, *Phys. Rev. Lett.* **74**, 3764 (1995).
- [11] T. O'Malley, *Phys. Rep.* **150**, 14 (1966).
- [12] R. Bieniek, *Phys. Rev. A* **18**, 392 (1978).
- [13] E. Clementi, supplement to *IBM J. of Res. and Dev.* **9**, 1 (1965).
- [14] H. Haberland, private communication, Albert-Ludwigs-Universität Freiburg, West Germany.
- [15] M. Aymar, S. Feneuille, and M. Klapisch, *Nucl. Instr. and Meth.* **90**, 137 (1970).
- [16] M. Manders, W. van Hoek, E. Vredenburg, G. Sandker, H. Beijerinck, and B. Verhaar, *Phys. Rev. A* **39**, 4467 (1989).
- [17] D. Hennecart, Ph.D. thesis, Université de Caen, Caen, France, 1982, unpublished.
- [18] P. Brussaard and P. Claudemans, in *Shell-model applications in Nuclear Spectroscopy* (North-Holland, Amsterdam, 1977), Chap. 13.
- [19] A. Messiah, *Quantum Mechanics* (North-Holland, Amsterdam, 1961), Vol. II.
- [20] A. Niehaus, in *The excited state in Chemical Physics*, edited by J. Gowan (John Wiley and Sons, New York, 1981), Chap. 5.
- [21] D. Hennecart and F. Masnou-Seeuws, *J. Phys. B* **18**, 657 (1985).
- [22] H. Kucal, D. Hennecart, and F. Masnou-Seeuws, *Chem. Phys.* **145**, 163 (1990).
- [23] W. Boom, R. van Galen, B. Klaver, S. Op de Beek, J. Heier, H. Beijerinck, and B. Verhaar, *Phys. Rev. A* **51**, 3837 (1995).
- [24] R. van Galen, Master's thesis, Eindhoven University of Technology, The Netherlands, 1992, report NO 92-17, unpublished.
- [25] W. Boom, H. Beijerinck, and B. Verhaar, *Phys. Rev. A* (1996), to be published.
- [26] W. Wiese, M. Smith, and B. Glennon, *Atomic Transition Probabilities* (Nat. Bureau of Standards, U.S., 1966), Vol. 1.
- [27] H. Hotop, J. Lorenzen, and A. Zastrow, *J. Electron Spectrosc. Relat. Phenom.* **23**, 347 (1981).







5

Calculation of Two-center Integrals involving a rapidly oscillating free Electron Wave Function

S.S. Op de Beek, J.P.J. Driessen, H.C.W. Beijerinck, and B.J. Verhaar

Optical potentials are used in a quantum mechanical treatment of loss processes *e.g.* ionization, where the loss of flux is described by the imaginary part. We present a numerical method for calculating two-center two-electron integrals necessary to construct the imaginary part of the optical potential. By introducing Slater-type Orbitals with complex-valued exponents (CSTO's), we are able to represent the free electron wave function with a limited number of CSTO's. For the representation of free electron wave functions with many oscillations, *i.e.*, in a large r -range or for a high kinetic energy, these new CSTO's form a more natural set of basis functions. The introduction of CSTO's is inevitable for the calculation of integrals concerning collisions in the mK energy range, where the interaction acts over large internuclear distances. Extensive numerical checks show that the final imaginary part of the optical potentials can be calculated with an accuracy better than 2%.

PACS numbers: 31.15.-p, 32.10.Hq, 31.15.Ar. 34.20.-b

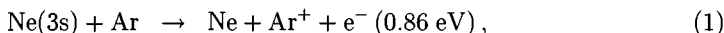


1 Introduction

In collisions of electronically excited atoms with ground state atoms and molecules various channels may be open.¹⁻⁴ If the excitation energy exceeds the ionization energy of the collision partner, ionization is a possible exit channel.^{5,6} This process is referred to as Penning or associative ionization, depending on whether the final state is an atomic or molecular ion. In principle, it can be regarded as an irreversible process: the wave function describing the colliding partners loses flux to the ionized channel. The calculation of this loss rate (or ionization rate) has been the subject of various theoretical studies.⁷

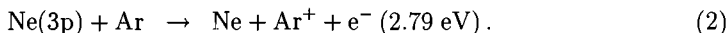
Ionization is an important loss mechanism in magneto-optical traps.^{8,9} Ionization may occur if an excited atom in the optical molasses collides with an atom or molecule of the background gas. Alternatively, the trapped atoms may collide with each other. If both atoms are excited, ionization may occur as well. In the last couple of years the investigation of trapped atoms has made tremendous progress. This has triggered theoretical interest to calculate ionization rates for these systems. A recent example is spin-polarized triplet helium, in which the prospects for the realization of Bose-Einstein condensation is determined by relaxation-induced Penning ionization.¹⁰

Penning ionization has been investigated in detail for the metastable rare gas - ground state rare gas and N₂ systems,⁶ *e.g.*, by measuring the yield of ions and/or electrons,¹¹ by analyzing the energy distribution of the electrons,¹² and by observing the influence of ionization on large angle elastic differential cross sections.¹³ In general, these measurements have been performed with an initial state in a well-defined fine structure and polarization configuration. A typical system is



where a low energy electron is emitted. These measurements have been carried out in a wide range of collision energies, starting at a few meV up to 10 eV and higher.¹¹ Using laser excitation the different behavior of the two fine structure states ³P₀ and ³P₂ has been well established experimentally. For a theoretical description we can suffice with an optical potential with an exponential type auto-ionization width that saturates at small internuclear distances. A remaining problem is the larger ionization cross section for the ³P₀ state, for which a theoretical basis is lacking.

In the last decade these measurements have been extended to rare gas atoms in short-lived, laser-excited states, such as^{14,15}



Additional information about the ionization process may be inferred from experimental results for the competing inelastic channels besides ionization, *e.g.*, the polarized-atom cross sections for intramultiplet mixing. For the non-ionizing Ne(3p) + He system, a coupled channels calculation gives results for intramultiplet mixing¹⁶ which are in good agreement with experimental cross sections. In case of ionizing systems optical potentials have to be used as input for a coupled channels calculation. The imaginary part will cause a loss of flux due to ionization, but will also affect the calculated cross

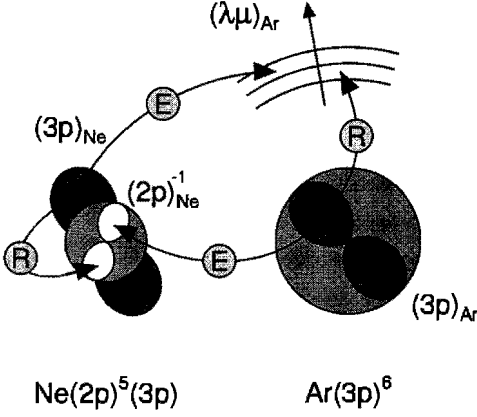
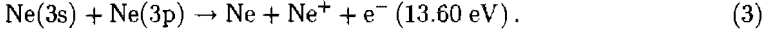


Figure 1: Schematic view of the two ionization mechanisms: R) radiative mechanism, where the two electrons remain centered on the same atoms; E) exchange mechanism, where the electrons are exchanged between the atoms.

sections for intramultiplet mixing. For the Ne(3p) + Ar system experimental results are available for 1.7 eV collision energy which will be used in a future analysis.¹⁷

Recently, there is a strong interest in so-called optical collisions of systems with a resonant dipole interaction.^{18,19} These collisions occur for a homonuclear system in two states that are connected by an electric-dipole transition, *e.g.*,



Because two excited states are involved, a high energy electron is emitted. The long range resonant dipole interaction $V \sim R^{-3}$ may lead to very large ionization cross sections, resulting in an important loss mechanism for cold atoms in a magneto-optical trap.

A rigorous description of the ionization process would involve all electron wave functions of the two colliding atoms. However, since essentially only two electrons are actively involved in the transition to the ionization channel, we restrict ourselves to a two-electron description. Depending on the role which they play in this process, we can distinguish two different mechanisms. They are depicted in Fig. 1 for the process of Eq. (2). First, the *radiative mechanism* in which the Ne(3p) valence electron decays into the Ne(2p)⁻¹ core hole while an Ar(3p) core electron is ejected as a free electron. Second, the *exchange mechanism* where the two electrons are exchanged during the ionization, resulting in the occupation of the Ne(2p)⁻¹ core hole with the Ar(3p) valence electron and the ejection of the Ne(3p) electron as a free electron.

The ionization rate can be constructed from the two following two-center two-electron integrals¹⁴

$$\begin{aligned}
 & V^{\text{rad}}(R; m_{\text{Ar}} m_c m_v \lambda \mu) \\
 &= \iint d\mathbf{r}_1 d\mathbf{r}_2 \Psi_{3p, m_{\text{Ar}}}^{\text{Ar}}(\mathbf{r}_1) \Psi_{\lambda \mu}^{\text{Ar}^*}(\mathbf{r}_1) \frac{e^2}{4\pi\epsilon_0 |\mathbf{r}_1 - \mathbf{r}_2|} \Psi_{3p, m_v}^{\text{Ne}}(\mathbf{r}_2) \Psi_{2p, m_c}^{\text{Ne}^*}(\mathbf{r}_2) \\
 &= \frac{e^2}{4\pi\epsilon_0} \langle 1m_{\text{Ar}}; \lambda, \mu | r_{12}^{-1} | 1m_v; 1m_c \rangle_{\lambda}^{\text{rad}}, \quad (4)
 \end{aligned}$$

$$V^{\text{exch}}(R; m_{\text{Ar}} m_c m_v \lambda \mu)$$



$$\begin{aligned}
&= \iint d\mathbf{r}_1 d\mathbf{r}_2 \Psi_{3p, m_v}^{\text{Ne}}(\mathbf{r}_1) \Psi_{\lambda\mu}^{\text{Ar}^*}(\mathbf{r}_1) \frac{e^2}{4\pi\epsilon_0 |\mathbf{r}_1 - \mathbf{r}_2|} \Psi_{3p, m_{Ar}}^{\text{Ar}}(\mathbf{r}_2) \Psi_{2p, m_c}^{\text{Ne}^*}(\mathbf{r}_2) \\
&= \frac{e^2}{4\pi\epsilon_0} \langle 1m_v; \lambda, \mu | r_{12}^{-1} | 1m_{Ar}; 1m_c \rangle_{\lambda}^{\text{exch}}, \tag{5}
\end{aligned}$$

where Ψ denotes the electron wave functions of the electrons involved. The subscripts c and v relate to the core and the valence electron of the neon atom. The emitted electron is characterized by the orbital angular momentum quantum numbers (λ, μ) , with μ representing the projection onto the internuclear axis. The corresponding wave function is a rapidly oscillating function extending to infinity. The other three electrons are bound p -states with magnetic quantum numbers m_{Ar} , m_c , and m_v for the $\text{Ar}(3p)$ -, $\text{Ne}(2p^{-1})$ - and $\text{Ne}(3p)$ -states, respectively. The integration variables \mathbf{r}_1 and \mathbf{r}_2 are the position vectors of electron 1 and 2. They are represented in spherical coordinates (r_a, θ_a, ϕ_a) with respect to the origin of nucleus $a = \text{Ne}$ or Ar . Finally, R denotes the internuclear distance.

A numerical procedure to calculate this type of two-center integrals has been discussed extensively by Wahl *et al.*²⁰ Recently, an analytical approach based on a complicated set of recurrence relations has been proposed by Rico *et al.*²¹ Both procedures use Slater-type Orbitals (STO) as basis sets. As is well recognized, STO's are a superior basis set for representing bound electronic wave functions. This representation provides a high accuracy in calculations of these integrals. Numerical tests suggest that an accuracy of 12 decimal places can be obtained.^{21, 22}

To calculate the ionization rates, the Coulomb wave function of the free electron needs to be represented in an STO basis set. Using CSTO's with a complex-valued exponent, it is possible to represent the rapid oscillating free electron accurately in a large r -range ($r < 75 a_0$) with a limited number of basis functions. In this paper we propose a modification of the methods of Wahl *et al.*²⁰ and Rico *et al.*²¹ The numerical recipes have been modified to allow for complex-valued exponents. Our code has been tested for a number of values of the set of parameters, which are typical for the ionization processes of Eqs. (1)-(3).

2 Preliminaries

To explain our approach we start from a number of methods, described in Refs. [20–22]. In these references notations slightly different from ours are used. Therefore, in this section we will briefly summarize common notations and definitions needed in the following sections. Computational methods for two-center two-electron integrals discussed in this paper are based on STO's with which the electron wave functions are represented. In our approach all electronic wave functions are expanded in normalized STO's defined as

$$\chi_{lm}(\mathbf{r}; n, \zeta) = \chi(r; n, \zeta) Y_{lm}(\theta, \phi) = C r^{n-1} e^{-\zeta r} Y_{lm}(\theta, \phi), \tag{6}$$

with (l, m) the angular momentum quantum numbers and C the normalization constant given by

$$C = (2\zeta)^{n+1/2} [(2n)!]^{-1/2}. \tag{7}$$

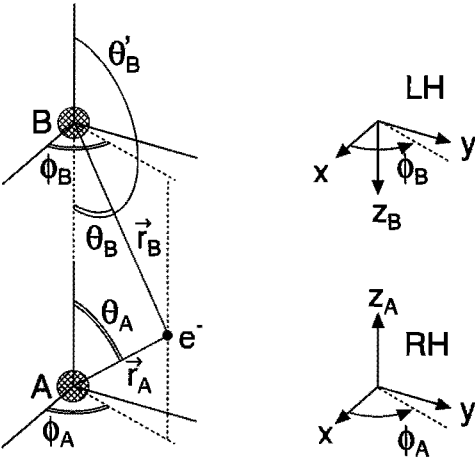


Figure 2: The spherical coordinates of one of the electrons are given in a right-handed frame (RH) for nucleus A and in a left-handed frame (LH) for nucleus B . Note that the azimuthal direction is the same in both frames.

The radial part of an STO is characterized by the parameters n and ζ which determine the shape of the STO. The angular part $Y_{lm}(\theta, \phi)$ is expressed as

$$Y_{lm}(\theta, \phi) = \left[\frac{(2l+1)(l-m)!}{2(l+m)!} \right]^{1/2} P_l^m(\cos \theta) \Phi_m(\phi). \quad (8)$$

Usually the function $\Phi_m(\phi)$ is chosen as a complex-valued function

$$\Phi_m(\phi) = \frac{e^{im\phi}}{\sqrt{2\pi}}. \quad (9)$$

However, sometimes this function is defined to be a real-valued even or odd function with the intention to avoid calculations with complex numbers:

$$\tilde{\Phi}_m(\phi) = \frac{1}{\sqrt{\pi}} \begin{cases} \cos m\phi, & (m \geq 0), \\ \sin |m|\phi, & (m < 0). \end{cases} \quad (10)$$

The two definitions of STO's in Eqs. (9) and (10) can be transformed into each other by

$$\begin{aligned} \chi_{lm} &= \frac{1}{\sqrt{2}} (\tilde{\chi}_{l|m|} + i \tilde{\chi}_{l-|m|}), & (m > 0), \\ \chi_{lm} &= \frac{(-1)^m}{\sqrt{2}} (\tilde{\chi}_{l|m|} - i \tilde{\chi}_{l-|m|}), & (m < 0), \\ \chi_{l0} &= \frac{1}{\sqrt{2}} \tilde{\chi}_{l0}, & (m = 0). \end{aligned} \quad (11)$$

Usually STO's are defined in terms of spherical coordinates centered on nuclei A and B , as depicted in Fig. 2. In various methods the angles θ_A and θ_B are defined with respect to two opposing quantization axes z_A and z_B . Since the azimuthal angles ϕ_A



and ϕ_B are defined with the same sense of rotation, a right-handed coordinate system is centered on nucleus A and a left-handed one on nucleus B. In a scattering analysis the wave functions centered on the two nuclei are always expressed with respect to the same quantization axis, which we will define in Fig. 2 as $\hat{z} \equiv \hat{z}_A$. Consequently, a transformation has to be performed on the wave functions centered on nucleus B. Because the azimuthal angles ϕ_A and ϕ_B are identical, only the Legendre polynomial in Eq. (6) is affected. The following transformation has to be applied to the STO's centered on nucleus B with $\theta'_B = \pi - \theta_B$, resulting in

$$\chi_{lm}(r, \theta_B, \phi_B; n, \zeta) = (-1)^{l-m} \chi_{lm}(r, \theta'_B, \phi_B; n, \zeta). \quad (12)$$

The two-center two-electron integrals have the following general form

$$\langle \chi_a \chi_{b'} | r_{12}^{-1} | \chi_c \chi_{d'} \rangle = \iint d\mathbf{r}_1 d\mathbf{r}_2 \Omega_{ab'}(\mathbf{r}_1) \frac{1}{r_{12}} \Omega_{cd'}(\mathbf{r}_2), \quad (13)$$

where the charge distribution functions Ω are defined by

$$\Omega_{ab'}(\mathbf{r}_1) = \chi_a(\mathbf{r}_1) \chi_{b'}^*(\mathbf{r}_1), \quad \Omega_{cd'}(\mathbf{r}_2) = \chi_c(\mathbf{r}_2) \chi_{d'}^*(\mathbf{r}_2). \quad (14)$$

The subscripts a, b, c , and d denote either center A or B and the prime indicates the final state. In the general notation of Eq. (13) the two types of integrals are written as $V_{\text{exch}} = \langle \chi_A \chi_{B'} | r_{12}^{-1} | \chi_B \chi_{A'} \rangle^{\text{exch}}$ and $V_{\text{rad}} = \langle \chi_A \chi_{A'} | r_{12}^{-1} | \chi_B \chi_{B'} \rangle^{\text{rad}}$.

In general, the integral of Eq. (13) is represented in prolate spheroidal coordinates (ellipsoidal coordinates) which are defined in terms of the previously introduced spherical coordinates as

$$\xi = (r_A + r_B)/R, \quad \eta = (r_A - r_B)/R, \quad \phi = \phi_A = \phi_B, \quad (15)$$

with r_A and r_B the distance of the electron from the respective nuclei and R the inter-nuclear distance. Using the following definitions²²

$$(-1)^a \equiv \begin{cases} 1, & \text{for } a = \text{nucleus A,} \\ -1, & \text{for } a = \text{nucleus B.} \end{cases} \quad (16)$$

the reciprocal relations can be written as

$$\begin{aligned} r_a &= \frac{1}{2} R (\xi + (-1)^a \eta), \\ \cos \theta_a &= \frac{1 + (-1)^a \xi \eta}{\xi + (-1)^a \eta}. \end{aligned} \quad (17)$$

The volume element in ellipsoidal coordinates is given by $d\mathbf{r} = (\frac{1}{2}R)^3 (\xi^2 - \eta^2) d\xi d\eta d\phi$, and the integration limits are $-1 < \eta < 1$, $1 < \xi < \infty$, and $0 < \phi < 2\pi$.

To evaluate the integrals in Eq. (13) the individual charge distributions are represented in ellipsoidal coordinates. Next, the electron-repulsion operator r_{12}^{-1} is expanded in Legendre polynomials using the Neumann expansion.²³ From this point we can distinguish different techniques for the further evaluation of the integrals. As pointed out

above, for the calculation two methods are important: *i*) analytical methods and *ii*) numerical integration methods. Before discussing these methods we will make a few general remarks by comparing them.

Wahl *et al.*²⁰ have proposed a partly numerical procedure for calculating radiative and exchange type integrals. It has an extremely low computational cost and allows one to attain high accuracy in the integrals for low quantum numbers (nlm) and large exponents ζR of the STO's. This method gives reasonable results for the radiative type of integrals. Unfortunately, it fails to give good accuracy for higher quantum numbers and small exponents in calculating the exchange integrals, due to numerical instabilities.

Analytical methods developed as an alternative in recent years have a higher accuracy at the cost of a greater computational effort and are mainly used for test purposes. An analytical approach to calculate the exchange integrals based on recurrence relations has been proposed by Rico *et al.*²¹ The computational cost is reduced drastically using recurrence relations which express the integrals in simple analytical functions. Compared to the method of Wahl *et al.* this approach gives accurate results for all quantum numbers, exponents, and internuclear distances with comparable computational cost. In the next two sections we will discuss the methods in more detail.

3 Numerical Methods

3.1 Recurrence algorithm

In this section we briefly summarize the recurrence algorithm of Rico *et al.*²¹ We refer to appendix B and Ref. [21] for definitions and derivations. We conveniently start with a simplified form of the intricate final expression for the two-center integral:

$$I \propto (\dots) \sum_m \sum_{l=0}^{\infty} (\dots) \sum_{k_1, k_2} (\dots) W_l^{|m|}(k_1, k_2; \beta_1, \beta_2) J_{lk_1 m_1}(\gamma_1) J_{lk_2 m_2}(\gamma_2), \quad (18)$$

where the dots (\dots) stand for additional variables which have been omitted since they are not relevant for the following discussion. In essence, the integrals are written as an infinite summation over l , and a double summation over k_1 and k_2 of two different auxiliary functions W and J (Eqs. (6) and (7) in Ref. [21]) depending on the parameters

$$\begin{aligned} \beta_1 &= (\zeta_a + \zeta_b) \frac{R}{2}; & \beta_2 &= (\zeta_c + \zeta_d) \frac{R}{2}; \\ \gamma_1 &= ((-1)^a \zeta_a + (-1)^b \zeta_b) \frac{R}{2}; & \gamma_2 &= ((-1)^c \zeta_c + (-1)^d \zeta_d) \frac{R}{2}. \end{aligned} \quad (19)$$

The generalized notation of Yasui *et al.* [Eq. (16)] allows us to use Eq. (18) for both exchange and radiative integrals, in contrast to Rico *et al.* who limit their treatment to exchange integrals. Rico *et al.* show that the summation over l converges rapidly, so that only a restricted range of l values is needed. The two J -functions arise from the individual charge distributions of the two electrons involved and the accompanying η -integration. The W -functions depend on parameters connecting the two charge distributions and contain the ξ -integration. Using recurrence relations the integral can be



Table 1: The function $\mu_l(\beta, s)$ with $l = 10$ and different values for β and s has been calculated with multiple precision arithmetic (MPA) resulting in the same values as obtained by MATHEMATICA. The double-precision results are presented up to the first digit which deviates from the MPA results (indicated with |). For $\beta \ll s$ the number of corresponding digits decreases dramatically.

β	s	$\mu_l(\beta, s)$	
		MPA/MATHEMATICA	Double
100	200	$5.532\ 793\ 701\ 816 \times 10^{-94}$	$5.532\ 793\ 701 4 \times 10^{-94}$
1.00	2.00	$1.480\ 475\ 898\ 035 \times 10^{-6}$	$1.480\ 475\ 89 7 \times 10^{-6}$
0.50	1.00	$4.686\ 655\ 862\ 190 \times 10^{-6}$	$4.686\ 655\ 8 \times 10^{-6}$
0.05	0.10	$1.359\ 123\ 467\ 413 \times 10^{-5}$	$1.357\ 0 \times 10^{-5}$
0.05	5.00	$3.014\ 460\ 753\ 935 \times 10^{-25}$	$-4. \times 10^{-18}$

evaluated efficiently. In order to fill the J_{lkm} functions we need some explicit starting relations. As described in Ref. [21] this can be done in a very stable way for a large range of parameters.

In contrast, the calculation of the auxiliary functions $W_l^m(k_1, k_2; \beta_2, \beta_2)$ is a more complicated problem and the recipe tends to become numerically unstable. Using recurrence relations the W -functions are expressed in W -functions with lower m , k and k' values. Ultimately, all W -functions can be constructed from the $W_l^0(0, 0; \beta_1, \beta_2)$ functions. In turn, these starting functions W_l^0 are derived from auxiliary functions $w_{l,\nu}$ with $W_l^0 = w_{l,l}$. Again, recurrence relations are used to calculate all $w_{l,\nu}$ -functions for $0 \leq l, \nu \leq l_{\max}$. As a result, the corner elements $w_{0,0}$, $w_{0,l_{\max}}$, $w_{l_{\max},0}$, and $w_{l_{\max},l_{\max}}$ need to be calculated to begin with. In the calculation of the corner elements $w_{0,l_{\max}}$ and $w_{l_{\max},0}$ Rico *et al.* introduce a function μ_l defined as

$$\mu_l(\beta_i, s) = e^s \sum_{k=l}^{\infty} \frac{(2\beta_i)^k}{k+1} \Gamma(-k, 2s), \quad (i = 1, 2), \quad (20)$$

with

$$s = \beta_1 + \beta_2. \quad (21)$$

Rico *et al.* do not report any numerical problems concerning loss of accuracy or bad convergence. However, the individual terms in the summation can be 20 orders of magnitude larger than the final summation μ_l . Hence, the accuracy in a standard double precision representation (15 digits) is too small to give accurate results. This is demonstrated in Table 1 where the values of μ_l calculated in double precision are compared with values calculated with MATHEMATICA for typical parameter values of l , β and s . In a double precision implementation the calculated μ_l -functions differ significantly, especially if one of the exponents is small and the other is large.

We implemented multiple precision routines (50 digits) based on an available multiple precision arithmetic library (MPA).²⁴ The MPA-results are identical to the values calculated with Mathematica. Only in a multiple precision implementation we are able

Table 2: Exchange and radiative integrals for the test systems of Yasui *et al.* The results of the present paper using the recurrence algorithm (RC) and the Gaussian-quadrature method (GQ) are compared to results obtained by Yasui *et al.*(RC/Y). The vertical bar indicates the attainable accuracy in comparison with the other methods.

molecule	algorithm	exchange	radiative
LiH	RC/Y ^{a)}	0.110 855 240 322	0.272 179 676 425
	RC ^{b)}	0.110 855 240 322	0.272 179 676 276
	GQ ^{b)}		0.272 179 676 424
BeF	RC/Y	0.147 697 441 413 $\times 10^{-7}$	0.393 441 678 274
	RC	0.147 697 441 413 $\times 10^{-7}$	0.393 441 678 273
	GQ		0.393 441 678 27 0
NaH	RC/Y	0.156 438 155 873 $\times 10^{-3}$	0.276 348 883 880
	RC	0.156 438 155 8 36 $\times 10^{-3}$	0.276 348 883 780
	GQ		0.276 348 883 820
ScF	RC/Y	0.575 837 963 697 $\times 10^{-22}$	0.285 714 285 714
	RC	0.575 83 6 626 908 $\times 10^{-22}$	0.285 714 285 714
	GQ		0.285 714 641 777

a) Yasui *et al.*²²

b) This work

to fully reproduce the results reported by Rico *et al.*²¹ Moreover, a few recurrence relations in Ref. [21] contain errors, as confirmed by Rico *et al.*²⁵ For completeness, the correct recurrence relations are given in Appendix B.

Subsequently, the multiple precision results for μ_l are converted to double precision and are used to calculate the two corner elements $w_{l_{\max},0}$ and $w_{0,l_{\max}}$. The remainder of the calculation is performed in double precision and leads to accurate computation of the integrals. The recurrence algorithm has the advantage that once the auxiliary functions W_l^m are calculated, one can easily calculate integrals with different magnetic quantum numbers by determining a new set of J_{lkm} -functions. The J -functions are derived from a smaller set of recurrence relations. Therefore, the evaluation is faster than for the W -functions. Using the general representation of the integrals, Eq. (13), we are able to apply this recurrence algorithm to radiative integrals as well.

The results obtained for exchange and radiative type integrals based on our implementation of the recurrence algorithm have been compared to values given by Yasui *et al.*²² As shown in Table 2 there is agreement in almost all digits given. The exchange integrals for the diatomic ScF system only agree in five digits, possibly due to the large values of ζ and the small absolute value of the integral. In Section 5 we will discuss the applicability of the recurrence algorithm for our calculations.



3.2 Numerical integration

The numerical approach described by Wahl *et al.*²⁰ for calculating exchange integrals leads to expressions which have a very slow numerical convergence. Therefore, we focus on the more simple and more stable method for calculating radiative integrals, which will be very useful to check the results obtained by the recurrence algorithm. We briefly outline Wahl's integration method for the radiative integrals. The integration over the first electron coordinate \mathbf{r}_1 can be done analytically and yields a potential $U_A(\mathbf{r}_2)$ depending on the coordinates of electron 2. Thus, the radiative integral can be written as

$$\iint d\mathbf{r}_1 d\mathbf{r}_2 \Omega_{AA'}(1) \frac{1}{r_{12}} \Omega_{BB'}(\mathbf{r}_2) = \int d\mathbf{r}_2 U_A(\mathbf{r}_2) \Omega_{BB'}(\mathbf{r}_2), \quad (22)$$

in which the potential $U_A(\mathbf{r}_2)$ is defined by

$$U_A(\mathbf{r}_2) = \int_0^{2\pi} d\phi_1 \int_0^\pi d\theta_{A,1} \sin \theta_{A,1} \int_0^\infty dr_{A,1} \frac{r_{A,1}^2 \Omega_{AA'}(\mathbf{r}_1)}{r_{12}}. \quad (23)$$

The remaining integral over coordinates of electron 2 is evaluated numerically using a two-dimensional Gauss-Legendre quadrature integration method²⁶ which is implemented with a variable grid size. In order to use this method, the integration variable ξ , as defined in Eq. (15), has to be transformed into a new variable t , with integration limits $-1 < t < 1$, which is defined by

$$t = \frac{\xi - \delta - 1}{\delta \xi}, \quad (24)$$

where the parameter δ is determined by the maximum value of ξ in the integration. Since ξ is the distance of the electron, scaled to the internuclear distance R , an upper limit of $\xi = 10$ is a good choice for our practical case. This corresponds to $\delta=9/11$.

Obviously, the accuracy depends on the grid size employed in the integration over both ξ and η , as can be seen in Table 3. The method converges very rapidly. However, the computational time increases drastically with decreasing grid size because of the two-dimensional grid. A practical value of $n_g=30$ is used in our calculations. The corresponding numerical results have been compared with the recurrence algorithm, as implemented in our code and by Yasui *et al.*²² As can be seen in Table 2 the agreement is excellent, even for the problematic ScF molecule where the number of agreeing digits is 6. Since the numerical integration will be used for test purposes, this performance will suffice.

4 STO expansion of free electron wave function

4.1 STO's with real-valued exponents ζ

In terms of STO's, the radial part of the wave functions is expanded as follows

$$\psi(r) = \sum_{i=1}^N c_i \chi(r; n_i, \zeta_i), \quad (25)$$

Table 3: Convergence of the Gaussian-quadrature technique (GQ) for a radiative integral $\langle \chi_{00} \chi_{00} | r_{12}^{-1} | \chi_{00} \chi_{00} \rangle^{\text{rad}}$, calculated at $R = 5 a_0$ with $\chi_{00} = \chi_{00}(r; n=1, \zeta=1)$. The grid size in each direction is characterized by the number of steps n_g . For values of $n_g \geq 30$ the accuracy is comparable with the adopted recurrence method of Rico *et al.* (RC)

GQ	n_g	integral
	10	0.33 4 $\times 10^{-2}$
	15	0.335 2 1 $\times 10^{-2}$
	20	0.335 204 9 70 $\times 10^{-2}$
	25	0.335 204 965 2 7 $\times 10^{-2}$
	30	0.335 204 965 264 $\times 10^{-2}$
	90	0.335 204 965 264 $\times 10^{-2}$
RC ^{a)}		0.335 204 965 264 $\times 10^{-2}$

^{a)} Result of our calculation using the recurrence algorithm of Rico *et al.*

with expansion coefficients c_i . The bound states occurring in the processes of Eqs. (1)-(3) are represented in a set of STO's in a rather straightforward way. Because the STO's do not form an orthogonal set of basis functions, the parameters c_i and ζ_i cannot be determined adequately in a least-squares analysis. Therefore, we have constructed an orthonormal set of basis functions in the interval $0 < r < r_{\text{max}}$ from a set of STO's with fixed n_i and ζ_i . The coefficients c_i are obtained by projecting the wave function on this orthonormal set. Next, the values of ζ_i can be refined using a least-squares analysis. In each iteration cycle a new orthogonal basis is constructed, yielding new values of c_i . Unfortunately, no optimization is obtained for the number of STO's nor for the values of n_i .

The representation of the bound state wave functions is given in Table 4. Following Clementi²⁷ we use a representation by eight STO's for the Ar(3p) wave function. For the Ne(3p), Ne(3s) and Ne(2p) wave functions we use data supplied by Haberland²⁸ to fit a superposition of three or four STO's. The relatively small number of STO's required for a good representation reflects the statement that STO's are an ideal basis set for bound state wave functions.

The free-electron wave functions are oscillating functions with an amplitude decreasing as $1/r$ due to flux conservation. In Appendix A the numerical method is described to obtain the free-electron wave function in the screened Coulomb potential. The screened Ar⁺ Coulomb potential is given by Aymar.²⁹ Asymptotically, the wave function $\psi_{\lambda,\mu}(r)$ corresponds to a free electron at the kinetic energy ϵ moving in a $1/r$ Coulomb potential. The behavior near the origin of any regular solution, and in particular the Coulomb wave, is given by r^λ , with λ the angular momentum quantum number. As a consequence, the exponents n_i in Eq. (25) play a role analogous to the principal quantum number in the hydrogen spectrum. Therefore, the exponents n_i have to be larger than λ .

The oscillatory behavior of the Coulomb wave function complicates the representa-



Table 4: Expansion coefficients of the bound state wave functions for Ar(3p), Ne(2p), Ne(3s) and Ne(3p) orbitals.

Ar(3p) ^{a)}	n_i	$\zeta_i(a_0^{-1})$	c_i
	4	8.7924	-0.12559
	2	9.0000	-0.18072
	4	15.0000	-0.01234
	4	11.9644	0.02183
	4	6.3011	0.10518
	4	3.4327	0.58041
	4	1.9409	0.46149
	4	1.0309	0.02249
Ne(2p) ^{b)}	n_i	$\zeta_i(a_0^{-1})$	c_i
	2	12.1578	0.00514
	2	5.4492	0.17733
	2	3.2708	0.43033
	2	2.0510	0.46019
Ne(3s) ^{b)}	n_i	$\zeta_i(a_0^{-1})$	c_i
	1	7.09325	0.09194
	1	1.51940	-0.30573
	2	0.60208	1.07499
Ne(3p) ^{b)}	n_i	$\zeta_i(a_0^{-1})$	c_i
	2	2.2154	0.08530
	2	4.8862	0.03626
	2	0.4476	-0.11808
	2	0.8087	0.22614

a) Clementi *et al.*

b) Haberland

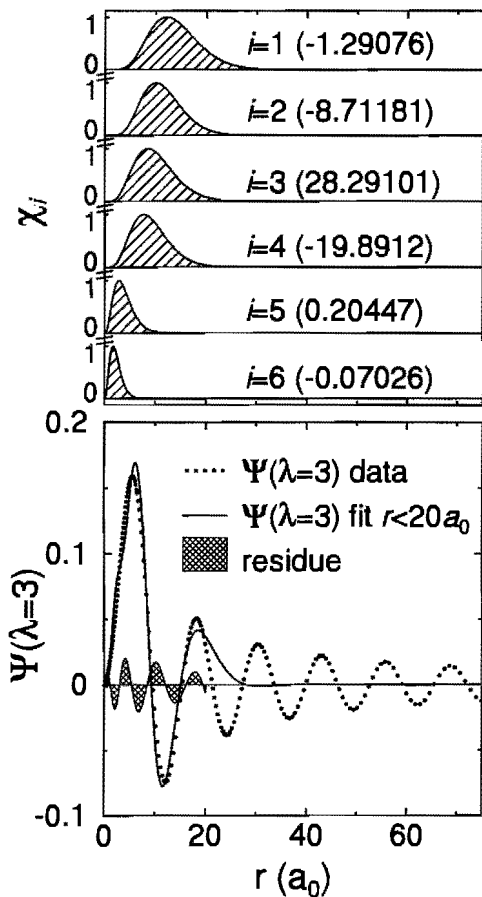


Figure 3: Representation of a free-electron wave function with energy $\epsilon = 2.79$ eV and angular momentum quantum number $\lambda = 3$ in a set of six STO's over the range $0 < r < 20 a_0$. The dots give the exact wave function, the solid line is the fitted representation in STO's and the cross-hatched area indicates the residue. In the upper panel the individual STO's χ_i are shown, with their expansion coefficients c_i given in parentheses. Note the magnitude of the expansion coefficients in comparison with the actual size of the wave function.

tion in STO's considerably. In the literature several methods for expanding coulomb wave functions in STO's are available, see Ref. [30]. Typically, the exponential parameters ζ_i are chosen according to the geometrical sequence $\zeta_i = \zeta_0 c^{1/i}$, with an empirically determined value of parameter ζ_0 and constant c . These recipes are based on solving the eigenvalues of a secular equation in an STO basis set. Since we are using a numerically integrated Coulomb wave function instead of a pure $1/r$ potential, this treatment is not applicable in our case. Therefore, we use an empirically determined set of STO parameters, inspired by the positions r_i of the extrema of the oscillations in the free electron wave function. At the position $r = (n - 1)/\zeta$ an STO has a maximum value. We aim to represent every extremum of the wave function by two STO's to allow for more flexibility. Starting from the outmost extremum in a certain range $(0, r_{\max})$, we take different values of n_i and ζ_i to represent every following extremum, with $n = \lambda + 1$ as a lower limit. Then we use a least-squares analysis to fine-tune the parameters ζ_i and we use the projection method for calculating the expansion coefficients c_i .

Figure 3 shows the result of such an STO-representation for $\lambda = 3$ for an electron

with kinetic energy $\epsilon=2.79$ eV in the region $0 < r < 20 a_0$. The number of STO's and the corresponding residue are comparable to results reported in the literature.³⁰ The obtained STO-representation contains expansion coefficients which are orders of magnitude larger than the actual Coulomb wave: the resulting curve is the remainder after cancellation of pairs of STO's with extremely large coefficients c_i with opposite signs. Because the two-center two-electron integrals are calculated with high precision, these kinds of cancellations are permitted without loss of accuracy. However, the integrals are very sensitive to the size and shape of the residue. Especially, for $r > r_{\max}$ the residue can be very large. The empirical value $r_{\max} = 20 a_0$ is found to be too small for accurate results. Therefore, the representation range of the free electron wave function has to be extended to a larger r -range. Due to the increasing width of STO's with increasing position of the maximum, $(n-1)/\zeta$, this extension is rather complicated. Not only the number of STO's increases drastically, also the magnitude of the expansion coefficients becomes order of magnitude larger than the actual value of the wave function. This emphasizes the necessity of using another basis set to represent the free electron wave function.

4.2 CSTO's with complex-valued exponent ζ

Using a complex-valued exponent $\zeta = \text{Re}\zeta + i\text{Im}\zeta$ in the definition of the STO's in Eq. (6) we can incorporate an oscillatory character in the basis functions, which are then more suitable for representing the oscillating free electron wave function. We thus define an STO with a complex-valued exponent, abbreviated as CSTO, as follows

$$\begin{aligned}\chi^\zeta(r; n, \zeta) &= \chi(r; n, \text{Re}\zeta) \cos(\text{Im}\zeta r + \phi) \\ &= \frac{1}{2} \left\{ e^{i\phi} \chi(r; n, \zeta) + e^{-i\phi} \chi(r; n, \zeta^*) \right\} = \text{Re} \left\{ e^{i\phi} \chi(r; n, \zeta) \right\}, \quad (26)\end{aligned}$$

with ϕ a phase factor, and χ as defined in Eq. (6). In Fig. 4 the same free electron wave function for $\lambda = 3$ is now represented with four basis functions. The wave function is represented in the much larger range $0 < r < 75 a_0$ with residues which are apparently a factor five smaller than in the pure STO case. The CSTO's form a better set of basis functions than in the STO case. Therefore, a least-squares analysis can be used to determine the parameters. The envelope of the wave function is described by the combination of parameters n_i and $\text{Re}\zeta_i$. The value of $\text{Im}\zeta_i$ can be estimated by means of the reciprocal de Broglie wavelength $\lambda_{\text{dB}} = \hbar/\sqrt{2m_e\epsilon} \approx 2.2 a_0$. The parameters used in this representation are listed in Table 5. The CSTO's form a good basis to represent free electron wave functions as is indicated by the magnitude and the convergence of the expansion coefficients, suggesting a negligible cancellation in the final superposition.

The representation in CSTO's is especially important if the number of oscillations to be represented is large, *e.g.*, when the wave function has to be represented in a large r -range, or in case of a high kinetic energy ϵ of the free electron, corresponding to a small period of oscillation. High energy electrons are emitted in the optical collision of Eq. (3). Using CSTO's allows us to represent the wave function of the free electron wave function with a high energy of $\epsilon = 13.6$ eV in a range of $0 < r < 75 a_0$, which is required for accurate calculation of ionization widths for this system. The result of this representation is shown in Fig. 5 for parameters listed in Table 6.

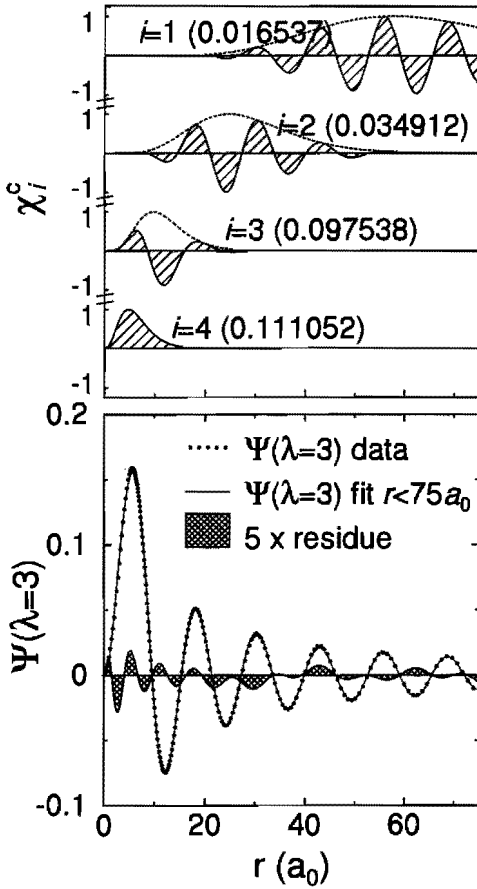


Figure 4: Representation of a free-electron wave function with energy $\epsilon = 2.79$ eV and angular momentum quantum number $\lambda = 3$ in a set of four CSTO's in the range $0 < r < 75 a_0$. The dots give the exact wave function, the solid line is the fitted representation in CSTO's and the cross-hatched area indicates the residue, after multiplication by a factor of 5. In the upper panel the individual CSTO's are shown, the dashed lines indicate the envelope, which is described by a real-valued STO with $\zeta_i = \text{Re } \zeta_i^c$.

Table 5: Parameters for the expansion of the free-electron wave function $\Psi_{\lambda\mu}$ with $\lambda = 3$ and electron energy $\epsilon = 2.79$ eV in CSTO's in the range $0 < r < 75 a_0$. The local wave number ($\text{Im } \zeta_i$) is comparable with the asymptotic reciprocal of the de Broglie wavelength $\lambda_{\text{dB}} \approx 2.2 a_0$.

n_i	$\text{Re } \zeta_i (a_0^{-1})$	$\text{Im } \zeta_i (a_0^{-1})$	c_i	ϕ_i
10	0.15615	0.48329	6.03783	1.29031
8	0.28410	0.48960	3.87872	0.77001
6	0.51689	0.42370	3.01415	1.11257
4	0.63193		1.45938	

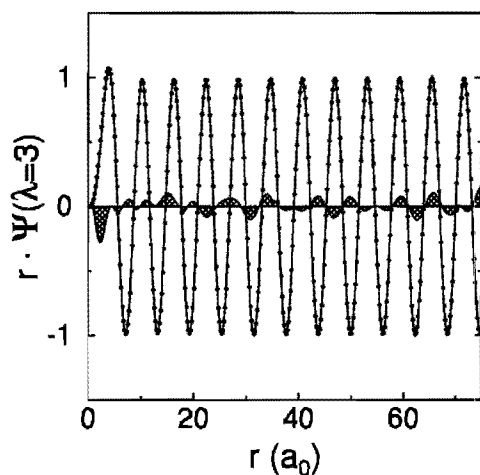


Figure 5: Representation of a free-electron wave function, multiplied by r , corresponding with an electron energy $\epsilon = 13.6$ eV and angular momentum quantum number $\lambda = 3$ in a set of five CSTO's on the range $0 < r < 75 a_0$. The dots give the exact wave functions, the solid line is the fitted representation in CSTO's and the cross-hatched area indicates the residue after multiplication by a factor of 5.

Table 6: Parameters for the expansion of the free-electron wave function $\Psi_{\lambda\mu}$ with $\lambda = 3$ and electron energy $\epsilon = 13.6$ eV in CSTO's in the range $0 < r < 75 a_0$. The local wave number ($\text{Im } \zeta_i$) is comparable with the asymptotic reciprocal of the de Broglie wavelength $\lambda_{dB} \approx 1 a_0$.

n_i	$\text{Re } \zeta_i(a_0^{-1})$	$\text{Im } \zeta_i(a_0^{-1})$	c_i	ϕ_i
7	0.10069	1.01177	6.57504	-0.11826
6	0.20313	1.01418	3.75567	-0.49336
5	0.39404	0.99272	2.54225	-0.47687
4	0.73958	0.82338	1.76560	0.28033
4	1.21036		0.68568	

Since we restrict the use of CSTO's to the representation of the free electron wave function only, no cross terms occur in the evaluation of the integrals. Consequently, the integral $\langle \chi_a \chi_{b'} | r_{12}^{-1} | \chi_c \chi_{d'} \rangle$ can be evaluated as

$$\langle \chi_a \chi_{b'} | r_{12}^{-1} | \chi_c \chi_{d'} \rangle = \text{Re} \left\{ e^{i\phi_i} \langle \chi_a \chi_{b'} | r_{12}^{-1} | \chi_c \chi_{d'}(\zeta_d) \rangle \right\}, \quad (27)$$

where the last step is justified by the fact that the integral is a real-valued quantity. In case that more wave functions are represented by CSTO's cross terms appear that cannot be neglected.

The introduction of a complex-valued exponent ζ means that the recipes for calculating the integrals have to be adapted for complex numbers. Since all the functions which are integrated over the elliptical coordinates η and ξ have at most one pole in the origin (η or ξ equals zero), the integration paths have to be taken in such way that they do not cross the negative real axis. The extension to complex numbers causes no serious problems in any of these algorithms. In Section 5 this extension to complex-valued exponents is extensively tested.

5 Test of numerical code

5.1 Transformation of complex χ_i to real-valued $\tilde{\chi}_i$ STO's

In the integrals of Eqs. (4) and (5), the spatial parts of the wave functions contain complex-valued spherical harmonics and the magnetic quantum numbers are given with respect to one quantization axis. Hence, at least one of the transformations given in Eqs. (11) and (12) has to be applied to the results obtained by the methods described in the previous two sections.

The recurrence algorithm uses real-valued STO's ($\tilde{\chi}$). As a consequence we have to expand each complex STO into a sum of even ($\cos m\phi$) and odd ($\sin m\phi$) functions using Eq. (11). We get a linear superposition of products of four STO's resulting in either an even or odd function of ϕ . Due to the integration over the angle ϕ only the resulting even functions contribute, reducing the number of relevant combinations to only 8. The final integral is subject to the conservation of the total magnetic quantum number

$$\underbrace{m_a + m_c}_{\text{initial}} = \underbrace{m_{b'} + m_{d'}}_{\text{final}}, \quad (28)$$

which reduces the number of non-zero integrals drastically. For the processes of Eqs. (1) and (3) we have five integrals, for the process in Eq. (2) up to 14 basic integrals can be defined in the same manner as in Ref. [14]. This notation is shown in Table 7.

The book-keeping of integrals, as described above, is susceptible to sign errors in the final summation. As an overall test we compared radiative integrals calculated with both the recurrence algorithm (for which the transformation of Eq. (11) has to be carried out) and the numerical approach, that uses complex-valued STO's defined with Eq. (9). The transformations are depicted in Fig. 6.

For this test case we took integrals containing three $l = 1$ STO's and one $l = 3$ STO, with parameters given in Table 7. This combination results in the 14 basic integrals



Table 7: Results of radiative integrals $\langle \chi_{1m_a} \chi_{1m_b} | r_{12}^{-1} | \chi_{1m_c} \chi_{3m_d} \rangle^{\text{rad}}$ calculated with the recurrence algorithm using real-valued STO's $\tilde{\chi}_{lm}$, have been transformed with Eq. (11) and are compared with the numerical approach using complex-valued STO's χ_{lm} . The single STO's are given by $\chi(r; n = 1, \zeta = 1)$. The integrals are listed for all possible combinations of magnetic quantum numbers. The third column is the result of both the recurrence after transformation and the numerical recipe by GQ($n_g = 30$), which agree in all digits given.

$m_a m_b m_c m_d$	recurrence	after transformation
	$\langle \tilde{\chi}_a \tilde{\chi}_b r_{12}^{-1} \tilde{\chi}_c \tilde{\chi}_d \rangle$	$\langle \chi_a \chi_b r_{12}^{-1} \chi_c \chi_d \rangle$
1 0 -1 0	$-0.265\ 216\ 29 \times 10^{-2}$	$-0.265\ 216\ 29 \times 10^{-2}$
0 0 0 0	$0.202\ 963\ 88 \times 10^{-1}$	$0.202\ 963\ 82 \times 10^{-1}$
1 1 0 0	$0.175\ 087\ 40 \times 10^{-1}$	$0.265\ 216\ 29 \times 10^{-2}$
0 1 1 0	$-0.265\ 216\ 29 \times 10^{-2}$	$0.175\ 087\ 35 \times 10^{-1}$
1 -1 -1 1	$0.148\ 195\ 58 \times 10^{-2}$	$0.135\ 133\ 23 \times 10^{-1}$
0 -1 0 1	$0.145\ 619\ 83 \times 10^{-2}$	$0.145\ 619\ 84 \times 10^{-2}$
1 0 0 1	$0.145\ 619\ 83 \times 10^{-2}$	$0.105\ 770\ 61 \times 10^{-1}$
1 -1 1 1	$0.120\ 313\ 71 \times 10^{-1}$	$0.296\ 391\ 15 \times 10^{-2}$
0 0 1 1	$0.105\ 770\ 65 \times 10^{-1}$	$-0.145\ 619\ 84 \times 10^{-2}$
1 1 1 1	$0.149\ 952\ 83 \times 10^{-1}$	$0.135\ 133\ 23 \times 10^{-1}$
1 -1 0 2	$0.825\ 132\ 28 \times 10^{-2}$	$0.355\ 653\ 06 \times 10^{-2}$
0 -1 1 2	$0.251\ 484\ 69 \times 10^{-2}$	$-0.116\ 691\ 33 \times 10^{-1}$
1 0 1 2	$0.251\ 484\ 69 \times 10^{-2}$	$-0.355\ 653\ 06 \times 10^{-2}$
1 -1 1 3	$0.482\ 398\ 02 \times 10^{-2}$	$-0.964\ 796\ 03 \times 10^{-2}$

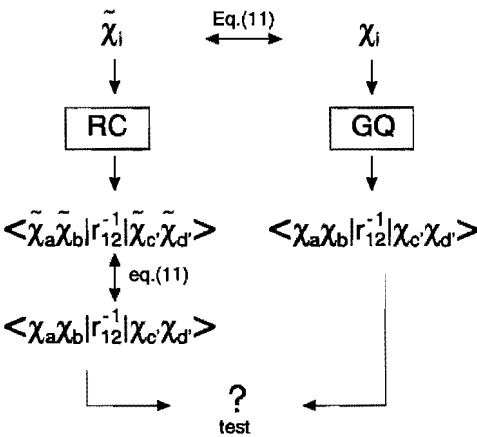


Figure 6: Schematic of the transformation between complex-valued STO's $\chi_i \sim e^{im\phi_i}$ and real-valued STO's $\tilde{\chi}_i \sim \cos m\phi_i / \sin m\phi_i$. The integrals obtained with the recurrence algorithm (RC) use $\tilde{\chi}_i$ whereas the numerical integration (GQ) uses χ_i . A transformation is required to compare their results.

Table 8: Expansion coefficients of two representations of the free-electron wave function Ψ_{00} with *i)* four STO's; and, *ii)* two CSTO's.

Ψ_0 (4 STO's)			Ψ_0 (2 CSTO's)				
n_i	$\zeta_i(a_0^{-1})$	c_i	n_i	$\text{Re } \zeta_i(a_0^{-1})$	$\text{Im } \zeta_i(a_0^{-1})$	c_i	ϕ_i
3	0.739	0.135×10^3	3	0.900	0.446	4.037	2.344
3	0.466	0.524×10^1	7	0.779	0.024	24.515	1.261
3	1.441	-0.108×10^1					
3	0.710	-0.139×10^3					

listed in the table. The transformed integrals and the numerically integrated results are identical to the accuracy shown. From this we conclude two things: *i)* no errors are introduced by transformations of Eqs. (11) and (9); and *ii)* the two methods are completely equivalent.

5.2 Comparison STO's versus CSTO's

To check the validity of the extension into CSTO's a simple test is performing a calculation for STO's with the CSTO-code. A more conclusive test consists of a comparison of a calculation done with wave functions represented by STO's only and a calculation performed for the same radial wave functions, with one of them represented in CSTO's. We evaluated the exchange and radiative integrals for a set of three identical $l = 1$ STO's, $\chi_{1m}(\mathbf{r}; n = 1, \zeta = 1)$, and one wave function ψ_0 with $l = 0$ which is shown in the middle panel of Fig. 7. It is given as the sum of four STO's, as depicted in the upper panel. In the lower panel of Fig. 7 we show the fitted representation in CSTO's of ψ_0 which has a negligible residue. Again, we see that the representation in CSTO's is superior for describing oscillatory structures. The parameters for both representations are listed in Table 8. Using the selection rules, as described in Section 5.1, only four basic integrals have to be calculated. The results for the exchange integrals denoted by $\langle m_a m_b | r_{12}^{-1} | m_c m_d \rangle^{\text{exch}}$ are shown in Fig. 8. For $R = 10 a_0$ the four basic exchange integrals resulting from the STO and CSTO representations are compared in Table 9. We see perfect agreement between the two different methods.

6 Performance

6.1 Two-electron two-center integrals

As an illustrative example we study the calculation of two-center integrals concerning the process of Eq. (2). The wave functions of the bound states involved are expanded in STO's as listed in Table 4. The free electron wave function for each value of angular quantum number λ in the range $0 \leq \lambda \leq 9$ is expanded in CSTO's in a constant range $0 \leq r < r_{\text{max}}$. The residue is approximately equal for the different wave functions. The number of oscillations in the range $0 < r < r_{\text{max}}$ decreases for larger λ -values and as a



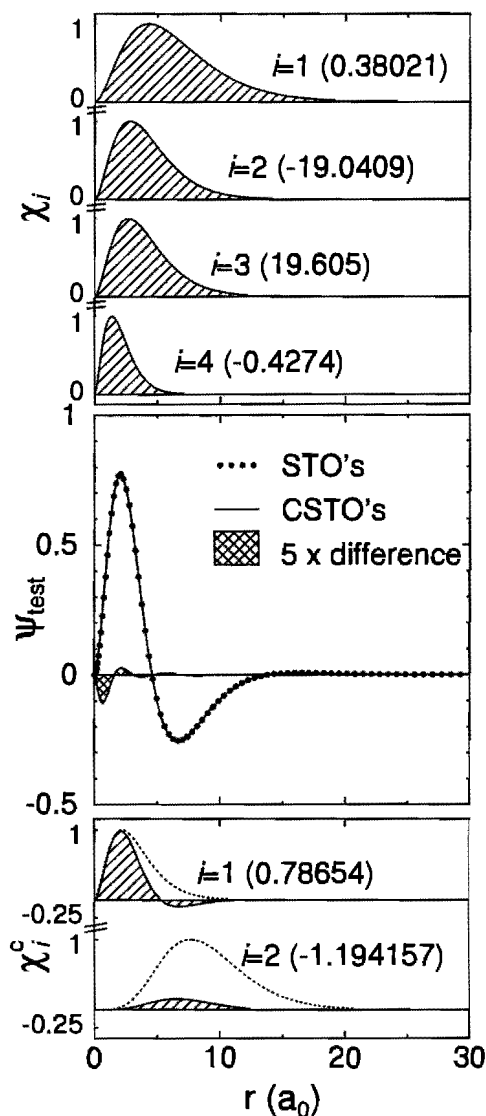


Figure 7: The middle panel shows the superposition (dotted line) of four STO's which are depicted in the upper panel. The resulting superposition is fitted (solid line) with two CSTO's as shown in the lower panel, where the dashed lines indicate the envelope of the CSTO's. The expansion coefficients c_i are given in parentheses for each STO and CSTO. The difference in representations is shown by the cross-hatched area. The parameters of the basis functions (C)STO's are given in Table 8.

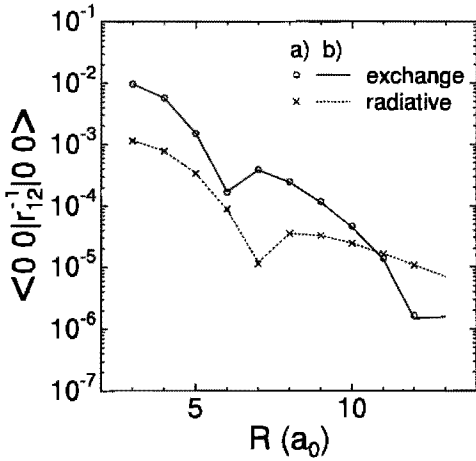


Figure 8: Results of the exchange integral $\langle \chi_{1m_a} \chi_{1m_b} | r_{12}^{-1} | \chi_{1m_c} \psi_{0m_d} \rangle^{\text{exch}}$ with single STO's $\chi(r; n = 1, \zeta = 1)$ and the fourth wave function ψ_0 represented by either STO's (a, markers) or CSTO's (b, lines).

Table 9: Exchange integrals $\langle \chi_{1m_a} \chi_{1m_b} | r_{12}^{-1} | \chi_{1m_c} \psi_{0m_d} \rangle^{\text{exch}}$ at an internuclear distance $R = 10 a_0$ calculated for two different representations of ψ_0 . The first three wave functions are given by a single STO $\chi_{1m}(r; n = 2, \zeta = 1)$. The fourth wave function ψ_0 is represented in a set of STO's and in a set of CSTO's with coefficients as listed in Table 8.

$m_a m_b' m_c m_d'$	Ψ_0 (4 STO's)	Ψ_0 (2 CSTO's)
1 0 -1 0	-0.3813×10^{-3}	-0.3843×10^{-3}
0 0 0 0	-0.4464×10^{-2}	-0.4465×10^{-2}
1 1 0 0	0.5617×10^{-3}	0.5694×10^{-3}
0 1 1 0	-0.7770×10^{-3}	-0.7794×10^{-3}

Table 10: Number of integrals as a function of quantum number λ for the Ne(3p)+ Ar Penning ionization process. The condition $|s| < 120$, for which the algorithm is stable, reduces the number of integrals. For $R = 3 a_0$ this number is not yet reduced, whereas for $R = 13 a_0$ the total number of integrals is reduced to 75%. The net reduction is listed in the column \bar{R} . The average calculation time is 8.5 s per set of STO's for exchange and radiative integral together.

λ	N_λ	N_{int}	criterion $ s < 120$			\bar{R}
			$R = 3 a_0$	$R = 8 a_0$	$R = 13 a_0$	
0	6	768	768	708	431	635
1	6	768	768	723	472	654
2	5	768	768	754	498	673
3	4	512	512	507	353	457
4	4	512	512	507	354	457
5	4	512	512	507	353	457
6	3	384	384	381	267	344
7	3	384	384	381	267	344
8	3	384	384	381	267	344
9	3	384	384	381	267	344
Total:		5248	5248	5230	3528	4668
time: ^{a)}		12h23m	12h23m	12h20m	8h20m	11h01m

^{a)} timing on Pentium 90 Mhz

result a smaller number N_λ of CSTO's is necessary to describe the free electron wave function. In Table 10 the total number of integrals $N_{int} = N_{Ar} N_c N_v N_\lambda$ is listed as a function of λ .

In Section 3.1 we already introduced the parameter s in Eq. (21), which can be expressed in the exponents of the STO's with Eq. (19) as

$$s = (\zeta_a + \zeta'_b + \zeta_c + \zeta'_d) R/2. \quad (29)$$

For certain combinations of STO's contributing to the total integral the s -parameters can take up values $\geq 20 (a_0^{-1}) R$. For $R > 7 a_0$ these combinations lead to $s > 140$, for which the numerical code becomes unstable. Apparently, for these s -values the summation $\sum WJJ'$ of Eq. (18) needs to be calculated in multiple precision using MPA because the individual terms are orders of magnitude larger than the final value of the summation. The extension of the complete calculation to multiple precision increases the computation time drastically. However, we have found empirically that the relative contribution of STO combinations with these large s -values to the net integral is less than 1%. Therefore, these contributions are omitted for $|s| > 120$. Furthermore, due to this s -parameter restriction the total computation time is reduced for increasing values of R , as is shown in Table 10.

Table 11: Parameters for the expansion of the free-electron wave function $\Psi_{\lambda\mu}$ with $\lambda = 3$ and electron energy $\epsilon = 2.79$ eV in CSTO's in the range $0 < r < 75 a_0$, now with odd values of n_i for the CSTO's (see also Table 5).

n_i	$\text{Re } \zeta_i(a_0^{-1})$	$\text{Im } \zeta_i(a_0^{-1})$	c_i	ϕ_i
9	0.13699	0.48280	6.12105	1.32344
7	0.24732	0.48975	3.87082	0.76751
5	0.44137	0.43899	2.89940	0.86897
4	0.65905		1.23792	

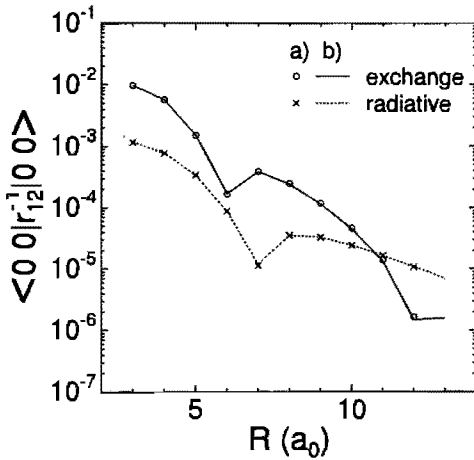


Figure 9: Results of the $\lambda = 3$ exchange and radiative integrals for the Ne(3p)-Ar system where the free-electron wave function is represented by the set in Table 5 (a, line) and by the set in Table 11 (b, markers). Only the integrals with all magnetic quantum numbers $m = 0$ are depicted.

The performance of our numerical code has been analyzed. About half of the computational time is spent in the MPA routines. Since the MPA routines use integer arithmetic, no gain in performance can be achieved by applying floating point calculation optimization techniques. For calculating radiative integrals we can choose between the recurrence algorithm and the numerical model. The two methods have approximately the same computation time.

Now that the integrals can be calculated in a stable way, we want to investigate the sensitivity of the integrals for changes of the CSTO-expansion of the free electron wave function. For this we calculated radiative and exchange integrals for two different sets of CSTO's describing the same Coulomb wave function. The first set is given in Table 5, the second set in Table 11. Both sets represent the $\lambda = 3$ free electron wave function with $\epsilon = 2.79$ eV. The first set has even n_i -values, whereas the second set has odd n_i -values. Consequently, the values for c_i , k_i and ζ_i are different for the two sets. The residues are of the same magnitude for the two sets. In Fig. 9 we compare the results of the exchange and radiative integrals with magnetic quantum numbers $m = 0$ for R -values ranging from $3 a_0$ to $13 a_0$. Although the basis sets differ considerably, the resulting integrals agree within 1%. The residue for $r > 75 a_0$ is not equal for

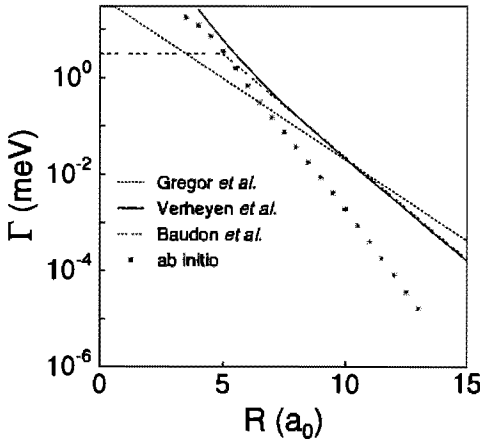


Figure 10: Results of ionization widths $\Gamma(R)$ for the mixture of 3P_0 and 3P_2 states of the Ne(3s)-Ar system. The calculated results are compared with experimentally determined ionization widths proposed by Gregor *et al.* and Verheyen *et al.*

both expansions, but does not affect the final results. From this we conclude that the description of the free electron wave function with $\lambda = 3$ in the range $0 < r < 75 a_0$ is sufficient for calculating two-center two-electron integrals.

6.2 Total ionization rates

The accuracy with which the total ionization rates can be calculated is limited to about 2%. This accuracy is determined by *i*) the criterion for omitting the contributions with parameter $|s| > 120$; and by *ii*) the residue in describing the free electron wave function. However, the accuracy for calculating the constituting STO-integrals has to be much higher than this 2% in order to guarantee accurate summations, where terms cancel to less than 10^{-6} of their individual values.

For the Ne($3s; {}^3P_0, {}^3P_2$) - Ar system we calculated auto-ionization widths.¹⁷ Due to spin-selection rules, only the exchange integrals contribute to the ionization width of the triplet states. From Fermi's "golden rule"³¹ the relation between the ionization width and the two-center two-electron integrals can be written as

$$\begin{aligned} \Gamma(R) &= \frac{2\pi}{\hbar} \left\{ \frac{m_e}{\hbar q} \sum \frac{e^2}{4\pi\epsilon_0} \sum_{\lambda} \left| \langle 1m_{Ar}; 1m_c | r_{12}^{-1} | 1m_v; \lambda, \mu \rangle_{\lambda}^{\text{exch}} \right|^2 \right\} \\ &= 1.994 \cdot 10^7 \frac{1}{\sqrt{\epsilon(\text{meV})}} \left| \langle 1m_{Ar}; 1m_c | r_{12}^{-1} | 1m_v; \lambda, \mu \rangle_{\lambda}^{\text{exch}} \right|^2, \end{aligned} \quad (30)$$

with q the asymptotic wave number of the emitted electron with kinetic energy ϵ and the first summation running over the angular quantum numbers $J = 1/2$ and $3/2$ of the $\text{Ar}^+(3p^5, {}^2P_J)$ -ion and over the quantum numbers of the initial and final Ne-states. A scaling factor, which depends on the kinetic energy ϵ , is required to obtain absolute values for the ionization width. In this example the contributions of integrals for $\lambda > 6$ are negligible. The resulting ionization widths for the different initial electronic states are shown in Fig. 10. The total ionization width can be characterized by an exponentially decaying function proportional to $\exp(-0.65 (a_0^{-1}) R)$. The structure present in the individual λ -contributions disappears when summing over λ .

In general, empirical ionization widths are described by an exponential function. The slope of the potential proposed by Gregor *et al.*³² differs from our results, as shown in Fig. 10. Gregor *et al.* derived the potential by simultaneous fitting experimental data for the ionization cross sections, quenching rates and elastic scattering angular distributions at thermal energies. Verheyen *et al.*¹¹ have proposed potentials derived from experimental results for the total ionization cross section in a wide energy range (0.1 eV–2 eV). The potential for the mixture of 3P_0 and 3P_2 as determined by Verheyen *et al.* is in fair agreement with our results for $R < 7 a_0$, as shown in Fig. 10. In a semi-classical analysis we found that the dominant contribution to the ionization process occurs for impact parameters $b < 7 a_0$, close to the turning point. Therefore, our calculated potential gives strong support for the potential of Verheyen.

7 Conclusion

Ab initio potentials have been used to calculate cross sections of fine-structure state changing collisions for the Ne(3p)-He system. Good agreement of the calculated results and experimental data is obtained.¹⁶ To describe collisions of Ne with Ar, ionization has to be incorporated in the quantum mechanical code. Therefore, absolute values of ionization rates have to be available. Driessen *et al.*¹⁴ used a quantum chemistry package ATMOL running on a Cyber 205 supercomputer to calculate the two-center two-electron integrals. An arbitrary scaling factor was introduced to obtain the correct order-of-magnitude for the ionization rates. In our recipe, however, no scaling is required. The computer power necessary for running our code is not demanding: we performed our calculations on a Pentium 90 processor. Furthermore, a limited claim on available workspace (< 2 Mbyte) is sufficient to perform the calculations.

Recently, much attention has been paid to “optical collisions” of cold atoms,³³ where ionization is the main loss channel. An accurate calculation of ionization rates is essential for a good description of these processes. We have shown that the corresponding two-center two-electron integrals can be computed with high accuracy using the recipes described in this paper. A marked improvement is obtained by representing the free electron wave function in complex-valued exponent CSTO’s. It enables us to describe the free electron wave function in a large r -range and for high kinetic energies in the 10 eV-range. The additional computational cost of using complex-valued exponents is compensated for by the smaller number of CSTO’s required in the description of the free electron wave function.

The ab initio calculation of optical potentials for the Ne(3s) + Ar system¹⁷ are in good agreement with potentials proposed by Verheyen *et al.*¹¹ in the range $R < 7 a_0$. This implies that the relevant physics can be approximated by the electrostatic interaction of only two electrons. Since no scaling is introduced in our calculations, the agreement in absolute value with the experimental potentials indicates that normalization is carried out correctly in the calculation of the free electron wave function and in the application of Fermi’s “golden rule”.

Appendices

A Free electron wave function in Ar^+ -potential

The wave function $\Psi_{\lambda\mu}^{\text{Ar}}$ of the free electron with kinetic energy ϵ is calculated by solving the radial Schrödinger equation with a spherical symmetric potential representing the Ar^+ - e^- interaction. The screened Coulomb interaction we use is given by Aymar *et al.*²⁹ The Schrödinger equation is solved using a Numerov integration method and yields an unnormalized radial wave function $R_\lambda(r)$ which relates to the normalized wave function $\psi_\lambda(r)$ as

$$\psi_\lambda(r) = C R_\lambda(r) = \frac{u_\lambda(r)}{r}, \quad (\text{A1})$$

with C a flux-normalization constant. For large r -values, the interaction is pure Coulombic, and the function $u_\lambda(r)$ can be written as a superposition of regular $F_\lambda(r)$ and irregular $G_\lambda(r)$ Coulomb functions. This directly results in the correct normalization constant C . Using a recursion relation for the Coulomb functions,³¹ all F_λ and G_λ can be calculated starting with an explicit relation for G_0 .

B Corrected recurrence relations

In this appendix we give correct versions of the equations in the paper of Rico *et al.* which contains errors in essential parts. Eqs. (16) and (17) in Ref. [21] should be

$$w_{i,0}^{r,r'} = w_{i,1}^{r,r'-1} + \frac{1}{\beta'} \left[K_{l,r+r'-1}(s) + (r'-1) \{w_{i,0}^{r,r'-1} - w_{i,1}^{r,r'-2}\} \right], \quad (\text{B2})$$

$$w_{0,i}^{r,r'} = w_{1,i}^{r-1,r'} + \frac{1}{\beta} \left[K_{l,r+r'-1}(s) + (r-1) \{w_{0,i}^{r-1,r'} - w_{1,i}^{r-2,r'}\} \right], \quad (\text{B3})$$

Starting conditions of the $u_{l,l'}$ -matrix, Eqs. (28) and (29) should read

$$u_{l,l+1} = \frac{1}{(l+1)(l+2)} \frac{\Gamma(2, s)}{s^2}, \quad (\text{B4})$$

$$u_{i+1,i} = \frac{1}{l(l+1)} \frac{\Gamma(2, s)}{s^2}. \quad (\text{B5})$$

With the given restrictions on l and l' the definition $\nu_{-1} \equiv 0$ should be included. A sign error occurs in the last term of Eq. (33)

$$u_{i,1} = \frac{1}{2(2l+1)} [\dots] + \frac{l^2 + l - 1}{(2l-1)(2l+3)} \nu_{l-1}. \quad (\text{B6})$$

Another sign error appears in the last term of Eq. (36)

$$\beta^l w_{10}(\beta, \beta') = \dots - \theta_l(\beta) \mu_l(\beta, s). \quad (\text{B7})$$

And finally, Eq. (38) should look like

$$\beta^l w_{00} = e^{-\beta^l} L_0(\beta) - e^{+\beta^l} L_0(\beta, 1 + 2\beta^l/\beta). \quad (\text{B8})$$

References

- [1] H. Ferkel, A. Koch, and R. Feltgen, *J. Chem. Phys.* **100**, 2690 (1994).
- [2] M. Kitajima, K. Hidaka, H. Kusumori, M. Ukai, N. Kouchi, and Y. Hatano, *J. Chem. Phys.* **100**, 8072 (1994).
- [3] C. Richter, N. Andersen, D. Doweck, J. Houver, J. Salgado, and J. Thomsen, *Z. Phys. D* **30**, 211 (1994).
- [4] E. Spain, M. Dalberth, P. Kleiber, S. Leone, S. Op de Beek, and J. Driessen, *J. Chem. Phys.* **102**, 9522, 9532 (1995).
- [5] H. Yoshida, M. Kitajima, H. Kawamura, K. Hidaka, M. Ukai, N. Kouchi, and Y. Hatano, *J. Chem. Phys.* **98**, 6190 (1993).
- [6] P. Siska, *Rev. Rev. Mod. Phys.* **65**, 337 (1993), and references cited herein.
- [7] P. Julienne, K.-A. Suominen, and Y. Band, *Phys. Rev. A* **49**, 3890 (1994).
- [8] H. Boesten, B. Verhaar, and E. Tiesinga, *Phys. Rev. A* **48**, 1428 (1993).
- [9] R. Solts, A. Ben-Reuven, and P. Julienne, *Phys. Rev. A* **52**, 4029 (1995).
- [10] G. Shlyapnikov, J. Walraven, U. Rahmonov, and M. Reynolds, *Phys. Rev. Lett.* **73**, 3247 (1994).
- [11] M. Verheijen and H. Beijerinck, *Chem. Phys.* **102**, 255 (1986).
- [12] H. Hotop, J. Lorenzen, and A. Zastrow, *J. Electron Spectrosc. Relat. Phenom.* **23**, 347 (1981).
- [13] J. Kroon, A. C. Haverkorn, and H. Beijerinck, *Chem. Phys.* **103**, 119 (1986).
- [14] J. Driessen, S. Op de Beek, L. Somers, H. Beijerinck, and B. Verhaar, *Phys. Rev. A* **44**, 167 (1991).
- [15] W. Bussert, T. Bregel, R. Allan, M.-W. Ruf, and H. Hotop, *Z. Phys. A* **320**, 105 (1985).
- [16] M. Manders, W. van Hoek, E. Vredendregt, G. Sandker, H. Beijerinck, and B. Verhaar, *Phys. Rev. A* **39**, 4467 (1989).
- [17] S. Op de Beek, J. Driessen, S. Kokkelmans, H. Beijerinck, and B. Verhaar, chapter 4 of this thesis, to be published.
- [18] H. Dengel, M.-W. Ruf, and H. Hotop, *Europhys. Lett.* **23**, 567 (1993).
- [19] J. Grosser, D. Gudelfinger, A. Maetzing, and W. Behmenburg, *J. Phys. B* **27**, L367 (1994).
- [20] A. Wahl, P. Cade, and C. Roothaan, *J. Chem. Phys.* **41**, 2578 (1964).
- [21] J. Rico, R. López, G. Ramírez, and C. Tablero, *J. Chem. Phys.* **101**, 9807 (1995).
- [22] J. Yasui and A. Saika, *J. Chem. Phys.* **76**, 468 (1982).
- [23] F. Neumann, *Vorlesungen über die Theorie des Potentials und der Kugelfunctionen* (B.G. Teubner, Germany, 1878).
- [24] R. Brent, *ACM Trans. on Math. Soft.* **4**, 57 (1978).
- [25] R. López, private communication, Departamento de Química Física, Universidad Autónoma de Madrid, Spain.
- [26] W. Press, B. Flannery, S. Teukolsky, and W. Vetterling, *Numerical Recipes in Fortran* (Cambridge University Press, New York, 1989).
- [27] E. Clementi, supplement to *IBM J. of Res. and Dev.* **9**, 1 (1965).
- [28] H. Haberland, private communication, Albert-Ludwigs-Universität Freiburg, West Germany.
- [29] M. Aymar, S. Feneuille, and M. Klapisch, *Nucl. Instr. and Meth.* **90**, 137 (1970).
- [30] A. Macías, F. Matín, A. Riera, and M. Yáñez, *Phys. Rev. A* **36**, 4178, 4186, 4203 (1987).
- [31] A. Messiah, *Quantum Mechanics* (North-Holland, Amsterdam, 1961), Vol. II.
- [32] R. Gregor and P. Siska, *J. Chem. Phys.* **74**, 1078 (1981).
- [33] P. Julienne and F. Mies, *J. Opt. Soc. Am. B* **6**, 2257 (1989).

Concluding remarks

In this thesis two phenomena are studied in depth: *i*) intramultiplet mixing for Ne(3p)-He collisions and *ii*) ionizing collisions of Ne(3s) and Ne(3p) with Ar. Both phenomena have been subject of study for the last two decades by many experimental and theoretical groups. In a collaboration between the experimental Atomic Collisions and Quantum Electronics group and the theoretical Atomic Physics and Quantum Electronics group, both of the Eindhoven University of Technology, two branches of experimental research dealing with these phenomena have been set up ten years ago. The collaboration exists since then. We briefly discuss the development of these two research lines and we indicate in what direction both lines can have a 'bright' future.

Intramultiplet mixing

In 1984 a new apparatus was especially designed for measurements on the intramultiplet mixing process of short-lived Ne(3p) atoms. The short lifetimes of the Ne(3p) atoms and the small cross sections for the intramultiplet mixing process made it necessary to construct a very compact crossed-beam apparatus (mini-beam). This apparatus formed the basis of two previous Ph.D. projects in which two-vector correlation experiment were performed for thermal¹ and superthermal² collisions.

In the present project the same apparatus is still used, now to perform four-vector correlation experiments on the Ne(3p)-He system by detecting laser-induced fluorescence (LIF). Due to the very small LIF-signals measurements could only be performed for the Ne(3p, $\alpha_9 \rightarrow \alpha_8$) transition. In that sense, this four-vector correlation experiment forms a conclusive experiment with the mini-beam apparatus; more detail cannot be abstracted from this experiment. At the same time this experiment opens up a new era of four-vector correlation experiments on excited neon collisions that can be performed in apparatuses using bright beams.^{3,4} With a gain in signal of a factor 10^4 , 'mono'-energetic atoms and a non-divergent atomic beam, the quality of the data will improve and all transitions within the Ne(3p) multiplet can be studied.

In our experiment we used counter-propagating laser beams. From these measurements we are able to determine the diagonal elements and a few off-diagonal elements of the scattering matrix. However, in order to establish the complete scattering matrix, the preparation and probe laser beams should be oriented in non-parallel configurations as well. In a future four-vector correlation experiment this extra degree of freedom for the laser beams should be included in the design. These experimental considerations can be simulated and investigated using a quantum mechanical description of the four-vector correlation experiment that is based on the coupled channels code developed in an earlier stage.

The LIF/Doppler probe technique we use for probing the final Ne(3p) states implies an integration over the Doppler cone. The analysis of the experimental results are simplified to a great extent when the probe laser direction coincides with the initial relative velocity. For more flexibility in aligning the probe laser with respect to the

pump laser the parabolic mirror for efficient photon collection has to be partially offered. However, a large efficiency can also be achieved with a lense system.⁵

Ionizing collisions

In the last ten years extensive measurements have been performed on ionizing collisions of Ne(3s) and Ne(3p) with ground-state rare gas atoms in the Eindhoven group⁶⁻⁸ and other groups (see for example Refs. [9,10]). In our group the last conclusive measurements on this system were performed in 1992. Semiclassical and quantum mechanical descriptions of this ionization process have been formulated.^{7,9,11} A theoretical description of the ionization process in terms of projection operators¹¹ was the basis for the work described in the second part of this thesis. We developed a recipe for calculating two-electron two-center integrals involved in this description. A coupled channel code was extended to incorporate complex (optical) potentials. The calculated results are in good agreement with experimental results for both the intramultiplet mixing and ionization cross sections.

In 1994 the "Gemini" project⁴ started as a collaboration between the Eindhoven group and the Atomic Physics group of the Debye Institute of the University of Utrecht. The aim of this project is to study ultra-cold collisions of identical and asymmetrical systems. The first experiments in Eindhoven will concern the Ne(3s)-Ne(3p) system which is an ideal candidate to investigate ionization for low-energy "optical" collisions in the mK-range. These collisions can be studied as intra-beam collisions in a bright beam. Ab initio calculations of the ionization width are essential for a correct interpretation of collisions. For the symmetric Ne(3s)-Ne(3p) system, symmetry effects for the interchangeability of the nuclei have to be incorporated in the existing ionization width calculation. A careful investigation of these symmetry aspects has already been performed.¹² Therefore, it will be rather straightforward to adapt the code for calculating ionization widths for the symmetric Ne(3s)-Ne(3s) and Ne(3s)-Ne(3p) systems.

References

- [1] M. Manders, W. Ruyten, F. v.d. Benken, J. Driessen, W. Veugelers, P. Kramer, E. Vredendregt, W. van Hoek, G. Sandker, H. Beijerinck, and B. Verhaar, *J. Chem. Phys* **89**, 4777 (1988).
- [2] W. Boom, R. van Galen, B. Klaver, S. Op de Beek, J. Heier, H. Beijerinck, and B. Verhaar, *Phys. Rev. A* **51**, 3837 (1995).
- [3] M. Hoogerland, J. Driessen, E. Vredendregt, H. Megens, M. Schuwer, H. Beijerinck, and K. van Leeuwen, *Appl. Phys. B* **62**, 323 (1996).
- [4] H. Beijerinck, K. van Leeuwen, B. Verhaar, A. Niehaus, H. Heideman, P. van der Straten, and H. Rudolph, project proposal GEMINI, unpublished.
- [5] E. van Vliembergen, E. Vredendregt, G. Kaashoek, J. Jaspas, M. van Lanen, M. Janssens, M. Verheijen, and H. Beijerinck, *Chem. Phys* **114**, 117 (1987).
- [6] J. Driessen, F. van de Weijer, M. Zonneveld, L. Somers, M. Janssens, H. Beijerinck, and B. Verhaar, *Phys. Rev. Lett.* **62**, 2369 (1989).
- [7] J. Driessen, F. van de Weijer, M. Zonneveld, L. Somers, M. Janssens, H. Beijerinck, and B. Verhaar, *Phys. Rev. A* **42**, 4058 (1990).
- [8] J. Driessen, M. Manders, F. van de Weijer, G. Sandker, W. Boom, H. Beijerinck, and B. Verhaar, *Chem. Phys* **155**, 447 (1991).

- [9] W. Bussert, Ph.D. thesis, Universität Kaiserslautern, Germany, 1985, unpublished.
- [10] W. Bussert, T. Bregel, R. Allan, M.-W. Ruf, and H. Hotop, *Z. Phys. A* **320**, 105 (1985).
- [11] J. Driessen, S. Op de Beek, L. Somers, H. Beijerinck, and B. Verhaar, *Phys. Rev. A* **44**, 167 (1991).
- [12] J. Driessen and S. Op de Beek, unpublished results.

Summary

In this thesis the collision dynamics of excited neon atoms with ground-state rare gas atoms plays a central role. Two inelastic processes are studied: *i*) fine-structure changing transitions within the Ne(3p) multiplet due to collisions with ground-state He atoms and *ii*) ionizing collisions of Ne(3s) and Ne(3p) states with ground-state Ar atoms. On the basis of these processes fundamental insight can be gained in the dynamics and interactions involved in these collisions. Both from a theoretical as an experimental point of view, the work presented in this thesis can be regarded as a significant extension of work reported earlier. This project is a collaboration of the experimental Atomic Collisions and Quantum Electronics group and the theoretical Atomic Physics and Quantum Electronics group of the Physics Department of Eindhoven University of Technology.

The first part of this thesis deals with the process of fine-structure changing transitions, often referred to as collision-induced intramultiplet mixing. We study the transitions between short-lived Ne(3p) states ($\tau \approx 20$ ns) which are produced by laser excitation from one of the metastable Ne(3s) states, 3P_0 or 3P_2 , produced in a thermal metastable source. In the collision with He atoms, the alignment or orientation of the initial Ne(3p) state is determined by the polarization of the pump laser beam. Together with the well-defined initial relative velocity in our crossed beam experiment the alignment or orientation of the initial state can be controlled and manipulated (two-vector correlation experiment). In previous experiments the fluorescence from the initial and final state is monitored. From the ratio of the fluorescence signals absolute values for the polarized-atom cross sections $Q_{i \rightarrow f}^{|M_f|}$ are determined.

In the experiments described in this thesis we take one step further by analyzing the final Ne(3p) states as well. Using an extra laser (probe laser) to excite the Ne(3p) \rightarrow Ne(4d) transition the orientation or alignment of the final state can be determined by detecting the laser-induced fluorescence (LIF). This LIF scheme is combined with a Doppler probing scheme: the detuning of the probe laser selects a class of final states having a certain velocity component along the probe laser beam. In that sense, we are able to correlate four vectors: two velocity vectors and two alignment or orientation vectors of the initial and the final state. In the present experimental setup we performed the first four-vector correlation measurements on the elastic Ne(3p, $\alpha_7 \rightarrow \alpha_7$) and the inelastic Ne(3p, $\alpha_9 \rightarrow \alpha_8$) transitions for an average collision energy $\langle E \rangle = 70$ meV. In the case of Ne(3p) elastic scattering the LIF signal has extra contributions from two competing processes: elastic scattering of the metastable Ne(3s) state and 'Lorentz-tail' excitation of unscattered Ne atoms. The four-vector correlation experiment of the elastic scattering process is disturbed significantly by these extra signals. In case of inelastic scattering these competing processes do not contribute to the LIF-signal, though the expected signals are extremely small. The two level character of the Ne(3s, $^3P_2 \rightarrow$ Ne(3p, α_9) pump transition causes a 25 fold larger LIF-signal compared to collision-induced transitions from other Ne(3p) states. This gain in signal enables us to perform a four-vector correlation experiment for the inelastic scattering Ne(3p, $\alpha_9 \rightarrow \alpha_8$).

The theoretical description of this four-vector correlation experiment is given in terms of density matrices for the initial and final state. The separation of the differential cross section expression into a part comprehending the collisional quantum numbers and a part only depending on the scattering direction (θ, ϕ) reduces the computational effort with a factor of typically 10^5 . The first comparison of the calculated differential cross sections with the measured data is very promising.

The second part of this thesis concerns a theoretical study of Penning ionization occurring in Ne($3l$)-Ar collisions ($l=s,p$). Quantum mechanically, the process of ionization is described by the imaginary part of an optical potential $V_{\text{opt}} = V - \frac{1}{2}i\Gamma$. The autoionization width Γ takes into account the loss of flux due to ionization with a rate Γ/\hbar . In a two-electron approximation of the ionization process two different mechanisms can be distinguished. First, the *radiative mechanism* in which the Ne($3l$) valence electron decays into the Ne($2p$) $^{-1}$ core hole while an Ar($3p$) core electron is ejected as a free electron. Second, the *exchange mechanism* where the two electrons are exchanged during the ionization, resulting in the occupation of the Ne($2p$) $^{-1}$ core hole with a Ar($3p$) valence electron and the ejection of the Ne($3l$) electron as a free electron.

The ionization width Γ is constructed from two-center two-electron integrals formulated for each of the two mechanisms. For calculating these two-center two-electron integrals we use an integration method where the electron wave functions are expanded in so-called Slater-type Orbitals (STO's) which are generally used for describing bound electron states. By introducing STO's with complex-valued exponents (CSTO's) we can represent the free electron wave function over a large range of electron coordinates with a limited number of CSTO's with sufficient accuracy; the CSTO's form a more natural basis set for describing free electron wave functions. With this extension of the numerical recipe the two-center two-electron integrals can be accurately calculated.

Ab initio autoionization widths are calculated for the Ne($3l$)-Ar system ($l=s,p$). The results for the Ne($3s$)-Ar system are in good agreement with empirical ionization widths derived from a multiproperty analysis. For the Ne($3p$)-Ar system a quantum mechanical coupled channels code has been modified to incorporate the (complex) optical potential. We use ab initio potentials of Bussert *et al.* and our calculated ionization widths for the real and imaginary parts of the potential, respectively. For the very first time the influence of ionization on the intramultiplet mixing process can be studied theoretically. For the Ne($3p$)-Ar system experimental intramultiplet mixing cross sections measured by Boom *et al.* and experimental ionization cross sections obtained by Bussert *et al.* are compared with the results of the coupled channels calculation and give good agreement.

Samenvatting

In dit proefschrift speelt de dynamica van botsingen tussen geëxciteerde neonatomen en edelgasatomen in de grondtoestand een centrale rol. Twee inelastische processen worden bestudeerd: *i*) overgangen tussen de fijnstruktuurniveaus binnen het Ne(3p)-multiplet ten gevolge van botsingen met He-atomen en *ii*) ioniserende botsingen van Ne(3s)- en Ne(3p)-toestanden met Ar-atomen. Op basis van deze twee processen kan fundamenteel inzicht verkregen worden in de dynamica en de interacties die een rol spelen bij de botsing. Zowel vanuit theoretisch als experimenteel oogpunt kan het in dit proefschrift gepresenteerde werk beschouwd worden als een belangrijke uitbreiding van eerder onderzoek. Het betreft hier een gezamenlijk project van de experimentele groep Atomaire Botsingen en Quantum Elektronica en de groep Theoretische Atoomfysica en Quantum Elektronica, beide van de Faculteit Technische Natuurkunde van de Technische Universiteit Eindhoven.

Het eerste deel van dit proefschrift behandelt het proces van fijnstructuur-veranderende overgangen ook wel botsingsgeïnduceerde intramultipletmixing genoemd. We bestuderen overgangen tussen kortlevende Ne(3p)-toestanden ($\tau \approx 20$ ns) die worden aangemaakt door laserexcitatie van een van de metastabiele Ne(3s)-toestanden, 3P_0 of 3P_2 , geproduceerd in een thermische bron. De richting en/of draaizin van de Ne(3p)-begintoestand bij de botsing wordt bepaald door de polarisatie van de excitatie laser. We kunnen zowel de goed gedefinieerde relatieve snelheid in ons gekruiste-bundel experiment als de richting en/of draaizin van de begintoestand manipuleren (twee-vector correlatie experiment). De fluorescentie van begin- en eindtoestand wordt gemeten en uit de verhouding van deze fluorescentie signalen kunnen absolute gepolariseerde werkzame doorsneden $Q_{i \rightarrow f}^{M, J}$ bepaald worden.

In de experimenten die in dit proefschrift beschreven worden gaan we een stap verder door ook de Ne(3p)-eindtoestand te analyseren. Met behulp van een extra laser (de analyselaser) wordt de Ne(3p)-toestand geëxciteerd naar een Ne(4d) toestand. De richting en/of draaizin van de eindtoestand kan bepaald worden door de laser-geïnduceerde fluorescentie te detecteren. Deze detectiemethode kan worden gecombineerd met een Doppler-detectieschema: de verstemming van de analyselaser selecteert een klasse van eindtoestanden die een bepaalde snelheidscomponent in de richting van de analyselaserbundel hebben. Op deze wijze zijn we in staat om de correlatie tussen vier vectorgrootheden te bestuderen: twee snelheidsvectoren van begin- en eindtoestand en twee richtings- en/of draaizinvectoren van de begin- en eindtoestand. In het huidige experiment doen we vier-vector correlatiemetingen aan de elastische Ne(3p, $\alpha_7 \rightarrow \alpha_7$) en de inelastische Ne(3p, $\alpha_9 \rightarrow \alpha_8$) overgangen bij een gemiddelde botsingsenergie van $\langle E \rangle = 70$ meV. Bij de elastische metingen dragen er twee processen bij aan het uiteindelijke signaal: elastische verstrooiing van Ne(3s)-atomen en 'Lorentzstaart'-excitatie van onverstrooide Ne atomen. De vier-vector correlatiemeting wordt significant verstoord door deze extra signalen. Voor de inelastische metingen treden deze stoorprocessen niet op, echter de verwachte meetsignalen zijn hierbij erg klein. Het twee-niveau-karakter van de Ne(3s, $^3P_2 \rightarrow$ Ne(3p, α_9) overgang levert een 25-voudig meetsignaal op zodat we in staat zijn om vier-vector correlatiemetingen te doen aan de inelastische Ne(3p, $\alpha_9 \rightarrow \alpha_8$)

overgang.

Theoretisch wordt dit vier-vector correlatie-experiment beschreven in termen van dichtheidsmatrices van de begin- en eindtoestand. De rekeninspanning wordt met een factor 10^5 teruggebracht door de uitdrukking voor de differentiële werkzame doorsnede te splitsen in een deel dat afhankelijk is van de botsingsquantumgetallen en een deel dat afhankelijk is van de strooirichting (θ, ϕ). De eerste vergelijking van deze berekende differentiële werkzame doorsneden met experimentele data is veelbelovend.

Het tweede gedeelte van dit proefschrift betreft een theoretische studie van Penning-ionisatie bij Ne($3l$)-Ar botsingen ($l=s,p$). Het ionisatieproces wordt quantummechanisch beschreven door het imaginaire deel van een optische potentiaal, namelijk $V_{opt} = V - \frac{1}{2}i\Gamma$. De autoionisatiebreedte Γ beschrijft het fluxverlies tengevolge van een ionisatiesnelheid Γ/\hbar . In een twee-elektron benadering van het ionisatieproces onderscheiden we twee mechanismen. Ten eerste, het *stralingsmechanisme* waarbij het Ne($3l$) valentie-elektron terugvalt in het rompgat, terwijl een Ar($3p$)-elektron wordt uitgezonden als vrij elektron. Ten tweede, het *uitwisselingsmechanisme* waarbij de twee elektronen worden uitgewisseld tijdens de ionisatie, hetgeen resulteert in het opvullen van het Ne($2p$)⁻¹ rompgat met een Ar($3p$) valentie-elektron en de uitzending van het Ne($3l$)-elektron als vrij elektron.

De ionisatiebreedte Γ wordt geconstrueerd uit twee-centrum twee-elektron integralen, opgesteld voor ieder van de twee mechanismen. Deze twee-centrum twee-elektron integralen worden berekend met behulp van een integratiemethode waarbij de elektrongolf functie wordt gerepresenteerd in zogenaamde Slater-type orbitalen (STO's) die algemeen gebruikt worden voor de beschrijving van gebonden elektrontoestanden. Door toevoeging van een imaginair deel aan de exponent van de STO's kunnen we voldoende nauwkeurig met een beperkt aantal CSTO's de vrije-elektrongolf functie beschrijven over een groot bereik van de elektroncoördinaten; CSTO's vormen daarom een geschiktere basis voor de beschrijving van vrije-elektrongolf functies.

Voor het Ne($3l$)-Ar systeem ($l=s,p$) zijn ab initio auto-ionisatiebreedten berekend. De resultaten voor het Ne($3s$)-Ar systeem zijn in goede overeenstemming met empirische ionisatiebreedten zoals bepaald uit een verscheidenheid van verstrooiingsexperimenten. Een quantummechanisch gekoppelde-kanalen programma voor het Ne($3p$)-Ar systeem werd zodanig aangepast dat een complexe/optische potentiaal gebruikt kan worden. We gebruiken de ab initio potentialen van Bussert *et al.* en onze berekende ionisatiebreedten als reëel respectievelijk imaginair deel van de optische potentiaal. Voor het eerst kan nu theoretisch de invloed van ionisatie op het proces van intramultipletmixing worden bestudeerd. Voor het Ne($3p$)-Ar systeem zijn experimentele werkzame doorsneden voor intramultipletmixing en ionisatie gemeten door Boom *et al.* respectievelijk Bussert *et al.* in goede overeenstemming met de gekoppelde kanalen berekeningen.

Dankwoord

Het werk zoals dat nu voor u ligt is het resultaat van vier jaar ervaringen die op de plezierschaal ergens tussen droefenis en euforie liggen. Gelukkig zorgden een groot aantal mensen ervoor dat het zwaartepunt behoorlijk aan de vreugdevolle kant van dit bereik lag. Met name wil ik de volgende mensen noemen.

Herman Beijerinck, jouw enorme enthousiasme, je ongekeerde optimisme, maar ook zeker je snelle en kordate beslissingen hebben voor een groot deel bijgedragen aan het slagen van dit project. Ook je raad in persoonlijke kwesties was altijd zeer nuttig.

Jan Driessen, wij hebben elkaar in dit gezamenlijke onderzoek prima aangevuld en de samenwerking met jouw is voortreffelijk geweest. Ik denk dat Wolfram en konsorte nog een lange weg te gaan hebben voor ze een algebra pakket ontwikkelen dat jouw cijferwerk kan evenaren.

Boudewijn Verhaar, jouw vermogen om door iemand anders' denkraam te kijken naar een probleem en je kennis uit de kernfysica toegepast op atomaire botsingen zijn het theoretische stuk van dit proefschrift ten goede gekomen. Niet alleen de fysica was van hoog niveau, zo ook onze klimpartij naar de top van de Psiloritus.

Edgar Vredendregt, zonder twee van jouw perfect werkende lasers en je hulp bij het 'trekken' van de glasfibers zou er geen Hoofdstuk 3 zijn geweest.

Louis van Moll en Rien de Koning, als technisch brein van de groep hebben jullie me vaak bijgestaan met de reanimatie van de 'iets oudere apparatuur'.

Arjeh Tal, dankzij je enorme vertrouwen dat je in me gesteld hebt, ben ik in staat geweest veel te leren over computers en dergelijke.

Ton van Leeuwen, qua sterke verhalen vertellen zijn wij geloof ik aan elkaar gewaagd, maar het WC-rol experiment ga ik echt nog eens onder gecontroleerde omstandigheden uitvoeren.

Sander Peters, Noel Knoors en Koen Robben, Nico Buzing, Servaas Kokkelmans en Michel Roelofs, als afstudeerders en stagiaires hebben jullie een belangrijke bijdrage geleverd aan dit onderzoek.

Maarten Manders en Wim Boom, als mijn 'voorgangers' op dit onderzoek hebben jullie beide met ongekende degelijkheid de basis gelegd waarop ik prettig verder heb kunnen bouwen.

Mijn mede AIO's en andere mensen binnen de groep, zonder jullie zou het een stuk minder gezellig zijn geweest.

Peter, als 'grote broer' ben jij ooit met die natuurkunde begonnen...

Renske, de weekendjes in Delft en onze ellenlange telefoongesprekken hebben me op de been gehouden. Nu dit boekje af is wordt ik langzaam weer normaal en wellicht nóg vrolijker.



Curriculum Vitae

8 oktober 1968 geboren te Roermond
1986 eindexamen Atheneum,
Albert Schweitzer Scholengemeenschap te Geleen
1986 aanvang studie Technische Natuurkunde,
Technische Universiteit Eindhoven
1990 – 1991 studentassistent Natuurkundepracticum
voor Werktuigbouwkunde
1991 – 1992 studentassistent Computer Algebra
1992 doctoraal examen Technische Natuurkunde, cum laude,
Technische Universiteit Eindhoven
1992 – 1996 promotie-onderzoek (AIO),
groep Atomaire en Optische Wisselwerking,
Faculteit Technische Natuurkunde,
Technische Universiteit Eindhoven.

Stellingen behorende bij het proefschrift van S.S. Op de Beek "Orbital Dynamics in Excited Neon Collisions"

I

In de berekening van ionisatiebreedten verwaarlozen Driessen *et al.* ten onrechte de bijdrage afkomstig van impulsmoment-quantumgetallen $\lambda > 2$ voor het wegvliegend elektron.

Dit proefschrift, hoofdstuk 5

II

De afhankelijkheid tussen het reële en imaginare deel van de optische potentiaal zoals die uit experimentele grootheden wordt bepaald, is alleen op te heffen door een ab initio berekening te doen van tenminste één van beide bijdragen.

Dit proefschrift, hoofdstuk 5

III

De numerieke methode voor de berekening van 2-centrum 2-elektron integralen zoals voorgesteld door Rico *et al.* maakt rekenen in een precisie van 50 cijfers noodzakelijk.

Dit proefschrift, hoofdstuk 4

IV

De door Boom ingevoerde alternatieve representatie van gepolariseerde werkzame doorsneden is uiterst handig in het gebruik, maar heeft niets te maken met een representatie in componenten van een irreducibele sferische tensoroperator.

W. Boom, Proefschrift (1992), TU Eindhoven

V

Voor het berekenen van stroomdichtheden in dunne geleidende plaatjes in een diëlektrische laag met behulp van een eindige-elementenmethode blijken Thomas-Raviart elementen uiterst handig te zijn.

R. Ligtmans, Afstudeerverslag (1995), TU Eindhoven

VI

De empirische formule die de dimensies van een orgelpijp relateert aan de eigenfrequentie, opgesteld door de 19^{de}-eeuwse orgelbouwer M. Cavallé-Coll, is een frappant voorbeeld van bruikbare empirie.

H. Helmholtz, "On the Sensations of Tones" (Longmans & Co, 1885)

VII

Dat programmeurs zelfs in wijdverbreide besturingssystemen nog steeds verborgen routines weten in te bouwen wijst op een tekortschietende invloed van de opdrachtgever.

VIII

De cryptische UNIX-tools `sed` en `awk` vormen een onoverwinnelijk duo als het op geautomatiseerd editen aankomt.

IX

De mislukte lancering van de raket Ariane 5 is het zoveelste bewijs dat complexe software nooit geheel foutvrij is.

X

Het organiseren van conferenties met als onderwerp "luchtvervuiling", waarbij de participanten genoodzaakt worden tot het maken van een verre vliegreis, past niet bij de doelstelling van de conferentie.

Symposium on Air-polution 1993, Monterry, Mexico

XI

Het van kracht worden van de nieuwe spelling anno 1996 zal een ongewilde verarming van de spellingskennis tot gevolg hebben.

XII

Bach's muziek zou anders geklonken hebben wanneer deze componist een andere naam zou hebben gehad of in een ander talstelsel zou hebben gerekend.

K. van Houten en M. Kasbergen, "Bach en het getal" (de Walburg Pers Zutphen, 1985)

XIII

De moeilijke behandeling van de ziekte van Lyme is onder andere het gevolg van de onduidelijke diagnose, de grote spreiding in incubatietijd en de mogelijke mechanismen waarmee de spirocheten *Borrelia burgdorferi* aan immuniteitsreacties kunnen ontsnappen.

F.S. Kantor (Scientific American, september 1994, page 20)

XIV

Het beoefenen van de zwerfsport is slechts weggelegd voor de welgestelde burgerij.

Bever 'Zwerfsport' catalogus (Den Haag, 1996)

XV

Enige jaren intensieve omgang met een broer levert een bron van sterke verhalen voor een veelvoud van deze tijdsspanne.